Advances in Respiratory Impedance Predictions using Pulmonary Functional Imaging Models of Asthma

by

Cody Mathew Church

Submitted in partial fulfillment of the requirements
for the degree of Master of Science

at

Dalhousie University
Halifax, Nova Scotia
August 2018

© Copyright by Cody Mathew Church, 2018

Table of Contents

List of Tables

List of Figures

List of Abbreviations Used

Pulmonary Function Test	**PFT**
Forced Expiratory Volume in 1 Second	**FEV1**
Forced Vital Capacity	**FVC**
Total Lung Capacity	**TLC**
Provocation Concentration with 20% decrease	**PC20**
Airway Hyperresponsiveness	**AHR**
Forced Expiratory Flow 25-75%	**FEF25-75%**
Computed Tomography	**CT**
Chronic Obstructive Pulmonary Disease	**COPD**
High-Resolution Computed Tomography	**HRCT**
Positron Emission Tomography	**PET**
Nuclear Scintigraphy	**NS**
Single Photon Emission Computed Tomography	**SPECT**
Magnetic Resonance Imaging	**MRI**
Ventilation Defect Volume	**VDV**
Ventilation Volume	**VV**
Ventilation Defect Percentage	**VDP**
Forced Oscillation Technique	**FOT**
Respiratory Impedance	$\mathbf{Z_{rs}}$
Respiratory Resistance	$\mathbf{R_{rs}}$
Respiratory Inertance	$\mathbf{I_{r}}$
Respiratory Reactance	$\mathbf{X_{rs}}$
Respiratory Elastance	$\mathbf{E_{rs}}$
Respiratory Compliance	$\mathbf{C_{rs}}$
Tissue Damping	**G**
Tissue Stiffness	**H**
American Thoracic Society	**ATS**
Image Functional Modelling	**IFM**
European Respiratory Society	**ERS**
Functional Residual Capacity	**FRC**
Modality Independent Neighbourhood Descriptor	**MIND**
Fractional Volume Overlap	**FVO**
Dice Similarity Coefficient	**DSC**
Cumulative Distribution Function	**CDF**
Performance Index	**PI**
Sum of Squared Differences	**SSF**
Objective Function	**OF**
Multi-breath Washout	**MBW**

Abstract

Previous asthma pulmonary functional modelling used the locations of ventilation defects observed in inhaled gas imaging to implement binary airway closures and required additional random narrowing in ventilated regions to describe measured impedance, compromising predicted ventilation. Here we used gradations in intensity discretized using k-means clustering, and simulated annealing to choose degrees of narrowing within these regions to minimize the difference between measured and predicted ventilation. We found that the resistance ($p < 0.005$), reactance ($p < 0.05$), and ventilation ($p < 0.005$) predicted by the graded narrowing model was closer to subjects' measurements compared to the binary model. The graded approach did not fully account for the frequency dependence of resistance known to be indicative of heterogeneity. Thus, while the modelled airway narrowing predicted ventilation and impedance closer to subjects' measurements than binary closures, other factors or unobserved heterogeneity are needed to account for additional frequency dependence of resistance.

Acknowledgements

First and foremost, I would like to express my sincere appreciation for my supervisor, Dr. Geoffrey Maksym, who has been an endless source of knowledge and wisdom in the field of respiratory mechanics keeping many of my investigatory tangents grounded. Your email, your phone, and your door were always open to me for discussion, reassurance, and motivation; and for that I am very grateful.

I would also like to thank Dr. Grace Parraga for the data she provided for my thesis work. Beyond involvement with my thesis, her standards for professional conduct, and scientific communication are characteristics that I aspire to adopt in my professional career. Within her Laboratory at Western University, she has had several students that have been integral in my understanding of the data provided. I would like to thank these students: Rachel Eddy, Heather Young, and Dante Capaldi for all the help they have provided.

In my course work, I am indebted to Dr. James Robar and Dr. Mike Sattarivand for their instruction with MATLAB, which has been crucial for the completion of my thesis. Also, I owe thanks to Dr. Steven Beyea for providing my favourite (and most useful for this thesis) course on the physics of MRI.

To my classmates, and friends, John Lincoln, and Michael Reno; your camaraderie was essential throughout our academic struggles. It was a pleasure working with you, and I wish you two the best. To Lee MacDonald, your mentorship was truly invaluable, and I was very lucky to have your guidance.

I would like to thank all my family for their love and support. Finally, I would like to thank my partner, Jacqueline, your patience was paramount for my success.

Chapter 1. Introduction

1.1 List of Conference Abstracts and Awards

The following is a list of public contributions arising from the work presented in this thesis.

Conference Abstracts

1. Young H, Guo F, Eddy R, Church C* et al. (2017). Forced oscillation technique and MRI predictions of airway reactance in moderate-severe asthma.
   European Respiratory Society International Congress 2017
   Code that I developed was used to apply closures to a multi-branching airway tree model, and to calculate impedance.
2. Church C*, Young H, Parraga G, et al. (2018). Improvements in Functional Image Impedance Modelling of Asthmatic Lungs Using K-means Clustering.
   American Thoracic Society Conference
   Abstract with Presentation (Selected from submitted abstract for a mini Symposium: 15-minute talk including questions)

Awards

1. School of Biomedical Engineering – Dalhousie University
   Research Day 2018
   1st Prize – Pre-masters Category (Student Presentation Competition)

1.2 Preface

Asthma is usually described as an inflammatory disease that results in airway obstruction from physical narrowing of the airways, or airway plugging due to mucous. Symptomatically, it presents as episodes of breathlessness, chest-tightness and wheezing. The exact cause of bronchoconstriction and obstruction is believed to be the result of a variety of factors; namely: physical airway remodelling including increased airway smooth muscle and changes to the epithelial layer associated with mucous hypersecretion, as well as extravasated plasma.[1,2] Whether causing immediate narrowing, or linked to narrowing through longer term changes such as remodelling; the triggers of, and susceptibility to these responses, are believed to be a combination of environmental factors (airborne irritants, exercise) and likely genetic factors, but the causes are not often clear.[3] In 2015, the National Health Interview Survey found a 7.8% prevalence of asthma in Americans, with a larger prevalence in non-Caucasian races (> 9.0%), and an increasingly larger prevalence in low-income households.[4] In 2013, the cost of asthma per year in the United States totalled approximately $81.9 billion; with $3 billion being owed to missed work alone.[5]

1.3 Lung Structure and Function

Breathing is a manoeuvre that is achieved by the synchronous participation of the lungs, where gas exchange with the blood occurs, and the inspiratory muscles that coordinate to bring air into the lung, and the elasticity of the lung that follows passive exhalation, sometimes assisted by ribcage expiratory muscles during active exhalation. During inspiration, the diaphragm contracts and moves downward, while the external intercostal muscles contract which moves the ribcage in the cranial and outward direction. This sequence of events creates a more negative pressure outside of the lungs (relative to the atmosphere) leading to their expansion and inspiration. First, air flows through the conducting zone which includes: the oropharynx/nasopharynx, larynx, trachea, and mainstem-bronchi which are the first branches of airway tree. Next, the air passes into the respiratory region of the lung which includes the bronchioles, alveolar ducts, and alveoli which make up the majority of the lung parenchyma. The alveoli are thought of as elastic balloon-like structures, which have largely walls comprised of collagen and elastin fibres, and various other proteins. The stiffness, or elastance of the lung, arises largely from the elastic properties of the collagen and elastin fibres stretching during inspiration and surface tensions generated by the fluid-lining within alveoli. During passive exhalation, air is expelled from the lungs driven by this elastic recoil. In healthy lungs, the act of breathing is generally understood to result in a homogeneous filling of the lungs. But, with obstructive airway disease, ventilation of the lung has been seen to be spatially, and temporally heterogeneous.[6-8]

1.4 Diagnosis and Classification

Although objective measures are recommended, asthma is more often diagnosed using a combination of the subject's medical history, reported symptoms, and sometimes seasonal, and environmental exposures are considered.[9] Recommendations are that symptomatic subjects should receive pulmonary function testing (PFT), specifically spirometry (described in more detail below) to aid in diagnosis. However, a population-based study found that less than one-half of all candidates for spirometry actually receive the suggested testing.[10] subjects that do spirometry, will usually do this as part of reversibility testing where the response to a short-acting beta agonist bronchodilator is assessed by a second PFT.

From spirometry, the two most-common characteristics used to assess lung function are the forced expiratory volume in one second (FEV1) and the forced vital capacity (FVC). FEV1 is the volume of air expelled as rapidly as possible after a deep inspiration to total lung capacity (TLC), measured over the course of one second, and FVC is *total* volume of air that the subject can expel. Sometimes the FEV1 is used alone or often expressed as a ratio relative to FVC. FEV1 is used to assess reversibility and is also used to assess the sensitivity of the airways to a bronchoconstricting agent. This is done via a provocation test where increasing levels of the bronchoconstrictor, typically methacholine, are introduced in the subject, and the FEV1 is measured at each increment of added bronchoconstrictor until FEV1 is decreased by at least 20%, and the provocation concentration (PC20) is computed. PC20 values < 8 mg/mL indicate the presence of airway hyperresponsiveness (AHR) associated with asthma.[11]

1.5 Lung Function Testing

1.5.1 Spirometry

Unfortunately, FEV1 is not very sensitive to obstruction of the small airways (< 2 mm), where most respiratory diseases including asthma are thought to originate. Earlier studies indicated that a component of the forced exhalation maneuver known as FEF25-75% could be used to indicate small airway obstruction,[12-14] in which FEF25-75% is the forced expiratory flow from 25% to 75% FVC. However, more recently this was shown to be not well associated with small airways and was only weakly-moderately correlated with many characteristics of asthma,[15] and it lacked specificity.[16-18] An important limitation of spirometry to mention is that it is challenging to perform and can suffer from poor reproducibility due to the fact that it is a learned maneuver that requires expert training to meet the quality criteria current guideline standards.[19,20] Spirometry is thus challenging for preschool children where asthma is most often diagnosed, the elderly or geriatric, and impossible for subjects on mechanical ventilators. Approximately 10% of subjects are still unable to perform spirometry successfully even with training from an experienced respiratory technician.[21]

1.6 Imaging and Asthma

1.6.1 Computed (CT) and Positron Emission Tomography (PET)

Many imaging techniques have been employed that are able to show structural and functional information about the respiratory system. Computed tomography (CT) is commonly employed to assess lung structure in chronic obstructive pulmonary disease (COPD). However, CT is not used clinically for asthma, but structural changes can be observed using high resolution CT (HRCT). In one study, HRCT was able to show increased structural heterogeneity in persons with asthma post-methacholine in larger airways compared to healthy subjects.[22] However, an important innovation to understanding changes in lung function in disease including asthma was the development of imaging methods that rely on an inhaled gas. Positron emission tomography (PET), nuclear scintigraphy (NS), and single photon emission computed tomography (SPECT) can be utilized to assess ventilation heterogeneity by inhaling particular radioactive gases, which these different modalities can regionally quantify.[23] These techniques do have a disadvantage in that they confer a quantifiable radiation-dose, with the dose depending on the modality. For example, the average HRCT of the chest delivers an effective dose of 0.98 mSv,[24] which is the annual dose limit based upon recommendations from the International Commission of Radiological Protection.[25] The other radiation dependent techniques (PET/NS/SPECT) deliver less radiation but as typically employed, the dose limit prevents visualization of small airways.

1.6.2 Inhaled Gas Magnetic Resonance Imaging (MRI)

Inhaled gas MRI is an imaging technique that does not deliver radiation and uses inhaled non-radioactive inert gas. It was developed by Albert et al., in 1994 to image regions of the body that have low inherent proton densities such as lung tissue.[26] MRI signal intensity in regions with low proton density can be increased by introducing a spin ½ noble gas that has been hyperpolarized. This polarization of a noble gas is achieved through collisions with an optically pumped metal vapour (typically Rb), which increases the nuclear magnetic resonance signal from the gas nuclei by ~10^5. The hyperpolarized gas is put into a sealed bag, and carried to the subject waiting in the MRI, who inhales the gas prior to image acquisition. Modern imaging with hyperpolarized gases typically uses a breath-hold technique over a period of 16 seconds while images are acquired.[27] The distribution of intensities of the hyperpolarized nuclei are then indicative of where the gas was inhaled and to where it diffused, and regions of higher intensity are sometimes termed hyperventilated, while low intensity is hypoventilated, or if sufficiently low, termed a ventilation defect. The images then are often called ventilation images, even though this is not usually acquired during breathing, but as breath-hold. In healthy lungs the ventilation image is largely homogenous, but in asthma, images depict a large degree of ventilation heterogeneity, which has been correlated with disease severity.[28,29] As mentioned, where the image intensity is very low, below a chosen threshold, these pockets of non-ventilated regions are referred to as ventilation defects.[30] These ventilation defects in asthma are normally thought to be the result of gas trapping due to airway obstructions.[31] While conducting MRI with hyperpolarized gases uses a breath-hold technique, several factors have been found to affect the distribution of the gas signal with principal factors including (1) pendelluft flow, which describes the redistribution and exchange of gas between different regions due to inhomogeneous inflation of the lung[32] (2) regional partial pressure differences of oxygen, which causes regional differences in rapid relaxation of the spins in the hyperpolarized gas through dipolar coupling [29,33] and (3) diffusive redistribution, which similar to pendelluft, is redistribution of gas, but via collateral ventilation pathways (through pores in alveolar walls) in the lung thought to facilitate gas exchange.[34]

When first developed, ventilation defect volume (VDV), defined as the volume of lung devoid of signal, was manually segmented from the *central slices* of inhaled gas MRI.[7,35] However, this approach is inherently limited by inter- and intraobserver variability, and it does not quantify the ventilation defect volume for the entire lung. In recent years, automated approached have been developed which can segment MR images into meaningful distinct levels of ventilation.[36]

1.6.2.1 K-means Clustering

The approach used to analyze inhaled gas MR images into distinct intensity levels in this thesis is known as k-means clustering and is described here.[37] The objective of k-means clustering as developed for inhaled gas MRI is to delineate physiologically meaningful different levels of ventilation from the acquired intensity information, usually compared to an expert who discerns clusters often from histograms of the image intensities. The mathematical concept of k-means clustering is to partition a set of measurements, image or other type of data into k-clusters, where the data in the set of measurements is 'clustered' with the closest k-mean. To initialize this algorithm, a set of k means is defined that fit within the set of observations:

$$x = (x_1, x_2, \dots, x_k), \;\; x_i \epsilon E_N, \;\; i = 1,2, \dots, k \tag{1}$$

where E_N is the set of all points. As described in Kirby et al.,[38] the means initialized for this algorithm applied to an image can be derived from the centers of sorted ventilation intensities. The centers of each cluster are taken to be the means, and the ventilation intensities are assigned to the k-cluster by taking the set of points in E_N and evaluating the distance to all k means:

$$T_i^t(x) = \{\xi: \;\; \xi \epsilon E_N, \;\; |\xi - x_i| \leq |\xi - x_j|, \quad j = 1,2, \dots, k\} \tag{2}$$

where T_i^t is a set of points in E_N with a mean x_i, where the mean is iteratively updated until all data in the set of observations is sorted*:*

$$x_i^{(t+1)} = \frac{1}{|T_i^t|} \sum_{x_j \epsilon T_i^t} x_j \qquad (3)$$

where $|T_i^t|$ is the size of subset of points within E_N. In a clinical application, this process can be applied in 2D, or 3D. In Kirby et al., this process was applied in 3D with four k-clusters, with four being chosen to be in agreement with an expert chest radiologist's opinion of clinically significant signal intensity differences. To identify ventilation defects, they also applied a second level of k-means clustering (with four levels) to the lowest derived cluster from the first application of k-means to differentiate signal intensities that included background and the hypointense intense signal regions or ventilation defects.[38]

Delineation of the ventilation defect volume (VDV) from the ventilation defects as described above, and the ventilation volume (VV) which is the volume of lung with larger signal than the defect region, has been shown to be a useful method to assess the functional decrement in ventilating the lung the lung, and differences in correlated to disease severity.[39,40] Commonly the VDV is normalized as the ventilation defect percentage (VDP), defined from:

$$VDP = \frac{VDV}{TCV} * 100\% \qquad (4)$$

where TCV is the thoracic cavity volume, identified usually from proton MRI. VDP has been suggested as a useful biomarker for obstruction in small-airway diseases due to its association with disease and disease severity, but also in part because of its reproducibility using k-means clustering.[38]

VDP has been used in both ^{3}He and ^{129}Xe imaging, and tends to be larger in ^{129}Xe images compared to ^{3}He for the same individual.[41] The differences in this value are likely due to differences in the apparent diffusion coefficient or differences in density; however this is still under speculation.[42] But, given the scarcity of ^{3}He, recent ventilation imaging has moved towards more use of hyperpolarized ^{129}Xe, and more recently, free-breathing or inspiratory/expiratory methods can be used that do not need hyperpolarized gas, utilizing inhaled oxygen and the changes in density that occurs with changes in lung volume during breathing to identify regions of poor ventilation thought to correspond to ventilation defects.[43,44]

While VDP provides an objective quantity where lung function is clearly dysfunctional, it only characterizes the site, and size of obstruction observed in the lung. The airways responsible for the defects, cannot be visualized directly with MRI, but the defects do localize the volumes distal to the sites of airway obstruction. They do not tell us the changes in airway obstruction or diameters that leads to the development of observed ventilation heterogeneity. To better understand what changes are likely present to give rise to the ventilation heterogeneity we can use multi-branching airway trees to explore changes in airway and tissue properties that can lead to observed heterogeneity in inhaled gas distribution. When combined with measurements of respiratory system impedance by oscillometry (described below), which is also sensitive to small airway obstruction we can add another lens to understand the extent and possible variability underlying pathophysiology in asthma.

1.7 Forced Oscillation Technique (FOT)

Oscillometry is a technique developed by Dubois and colleagues in 1956 to non-invasively measure mechanics of the respiratory system.[45] An oscillating surface (often a loudspeaker) oscillates low-amplitude multifrequency flow directed into the mouth which results in pressure waves sinusoidally measured at the mouth during normal breathing. While flow is normally considered the input, and flow the output, we can examine either. Here we consider the pressure wave is formed discrete frequencies as depicted in Figure 1.1.

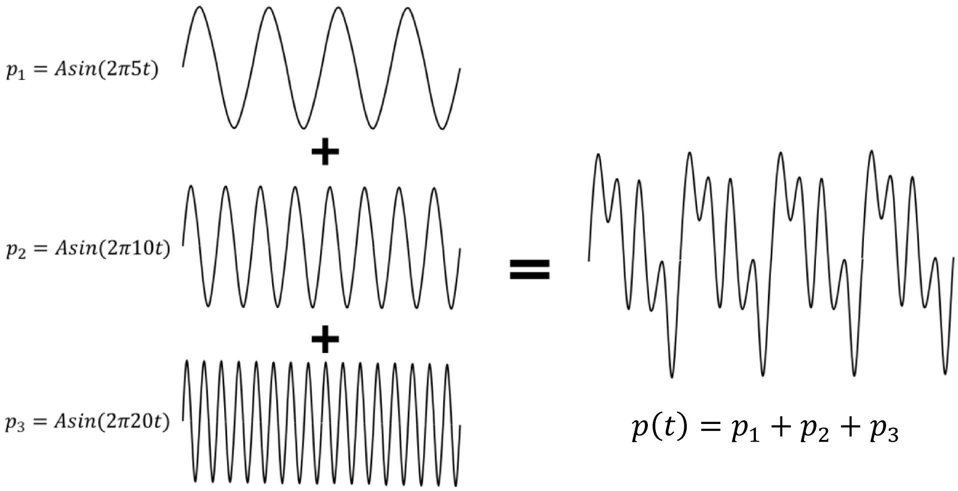

Figure 1.1: A set of sinusoidal pressure waves at discrete frequencies are superimposed to create a multifrequency pressure wave.

The airflow (V'_{ao}) and pressure at the airway opening (P_{ao}) is measured with the subject sitting upright, wearing nose-clips, and supporting their cheeks firmly with their hands as depicted in Figure 1.2. Measurements are repeated usually a minimum of 3 times, of duration of about 16 seconds or more and impedance averaged. Measurements are considered acceptable if the coefficient of variation is less than a threshold, usually 10% or 15%.

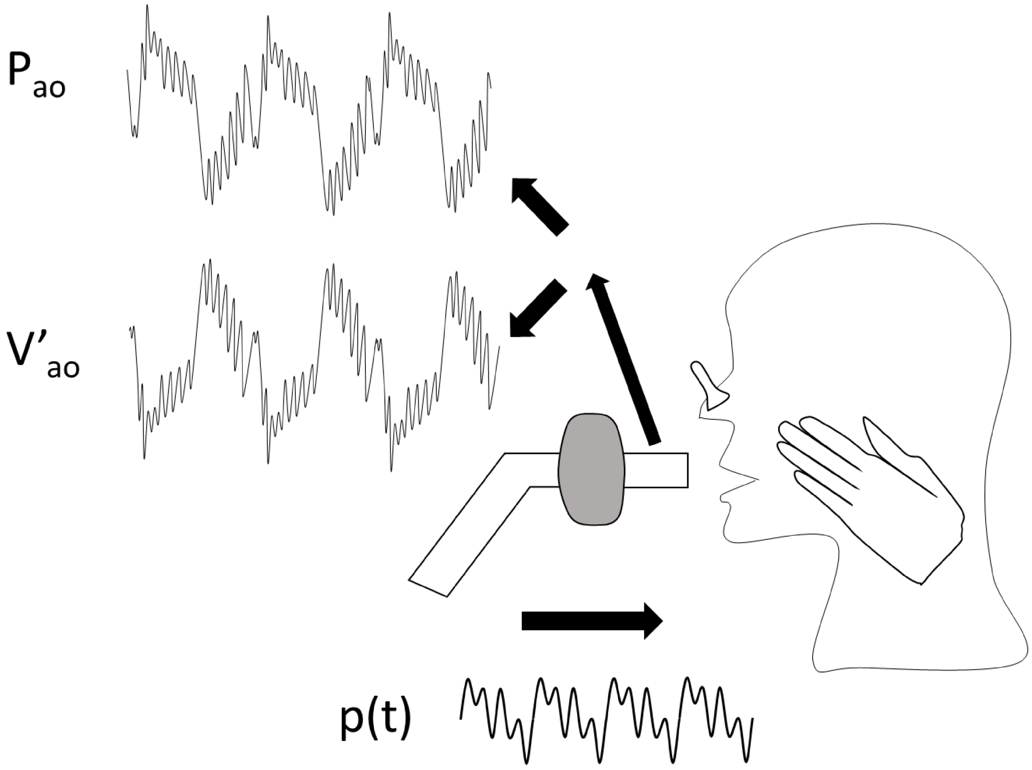

Figure 1.2. A depiction of an oscillometry measurement, where a multifrequency oscillatory signal is generated and the result pressure at the mouthpiece (P_{ao}), and also airflow at the mouthpiece (V_{ao}') are inferred from measurements correcting for the impedance of device between the subject and the sensors including the anti-viral and anti-bacterial filter and the subject respiratory impedance computed.

The impedance of the respiratory system (Z_{rs}), typically represented as function of frequency, is calculated by taking Fourier transform of the temporal pressure, and flow at the mouthpiece; and taking the ratio of these quantities:

$$Z_{rs}(f) = \frac{FT\{P_{ao}(t)\}}{FT\{\dot{V}_{ao}(t)\}} \tag{5}$$

The impedance is a complex mathematical quantity with a real component that is the ratio of pressure to flow in-phase with pressure, and the imaginary component is the ratio of pressure to flow that is 90 degrees out-of-phase. The impedance describes the difficulty in delivering flow and volume into the lung for a given pressure. However often it is interpreted using mathematical models with parameters designed to correspond to physical phenomena such as airflow resistance, or mechanical compliance that link structure to function. Various models have been developed to attribute airway and tissue mechanics to respiratory function, described further below. To interpret the impedance most generally, it is understood that the real component of the impedance, referred to as resistance (R_{rs}), is mostly related to the structure of the airways (largely the airway diameter). The imaginary component, which is in phase with volume changes of the lung, is referred to as reactance (X_{rs}), and is attributed to the elastic and inertive properties of the tissues. Depending on the model, contributions from the lung parenchyma, chest wall, or airway stiffness can be considered and each contribute to either the real or imaginary part of impedance to differing degrees. Further comments about mechanical impedance models can be found in the following sections.

FOT has an advantage over conventional PFTs' like spirometry, in that it does not require complex breathing manoeuvres, such as a deep inspiration with forced exhalation to complete; and it only takes about one minute to complete the typical 3 measurements. This technique has been shown to be feasible with infants,[46] children,[47] elderly,[48] geriatric subjects,[49] anaesthetized subjects,[50] and subjects on mechanical ventilation.[51] This technique has revealed that subjects with an obstructive airway disease such as asthma, usually demonstrates an increased R_{rs}, often with an inversely frequency dependent R_{rs} that is largely attributed to airway structural heterogeneity. Also, asthmatic subjects tend to exhibit a more negative X_{rs}, which implies an increased mechanical stiffness.[52, 53] R_{rs} has likely received the most attention in asthma as it is related to airway structure (diameter), and asthma is believed to be an obstructive disease of the airways (not changes in tissue properties). Like spirometry, several studies have established reference values to aid clinicians to determine abnormal values for R_{rs} and X_{rs}.[54-63] There have been clinical guidelines and recommendations from the American Thoracic Society (ATS) and European Respiratory Society (ERS) for FOT as a clinical tool.[64, 65] Additionally, there have been significant advancements by manufacturers to create user-friendly devices, including hand-held portable devices as shown in Figure 1.3.

Figure 1.3 The tremoflo^{TM} C-100 AOS^{TM}, a handheld oscillometer developed by Thorasys Thoracic Medical System Inc., Montreal, Canada.

1.7.1 Multi-branching Airway Tree Models for FOT

The emergence of imaging techniques that visualize ventilation have led to the development of computational multi-branching airway tree models that make use of the ventilation data to investigate the role of structural heterogeneity in asthma physiology. The complexity of the lung poses a significant challenge when designing an accurate model. The first useful airway tree that used branch airway dimensions was based upon data acquired from a resin cast of the lung down to the 10th airway generation, and microscopic measurements down to diameters of 2 mm using histological techniques.[66] This model was further developed by Horsfield and Cummings, where asymmetric branching conditions were added, where variations in daughter airways length and diameter were introduced.[67] Despite a few complex asymmetric bronchial tree models being available, the first demonstration of ventilation heterogeneity to reproduce a ventilation distribution similar to that observed in inhaled gas imaging was a simple symmetric bifurcating model.[68,69] This model incorporated airway instability whereby each airway was distended by inflation of the acinus it subtended as developed by Anafi and Wilson for a single airway. This model notably predicted the development of ventilation heterogeneity through this mechanism.[70] This model was not used to predict impedance, but other models, including models that extended the airway trees to smaller airways beyond those obtainable by casts have been used in an approach known as image functional modelling.

High resolution computed tomography (HRCT) with imaging parameters typically used in clinics can visualize the bronchial tree down to the 5-8th generation. While this allows the construction of subject-specific airway trees non-invasively, it does not include small airways. However, using large airways modelled from the HRCT, the remaining airways can be grown with a volume-filling algorithm guided by the fractal branching pattern of the lung. For this thesis, a multi-branching airway tree model generated by Tawhai and Hunter was utilized, and the process for the generation of the tree is as follows.[71,72] A random set of peripheral airway endpoints are generated and the center of mass from these points is calculated. A vector is created from final airway of the undeveloped tree to the center of mass of the randomly generated points, and the length of the resulting airway is taken as 40% of the length of this vector. New seed points are generated, and this process is repeated continuously until the airways reach a boundary, and the airway is terminated. *For the purposes of this thesis, the airways at the end of branch will be referred to as terminal; albeit convention has called for the first airway where gas exchange is occurring to signify the start of the terminal branch.* From the above process, the diameter of the daughter airway is calculated with:

$$\log\big(D(x)\big) = (x - N)\log\big(R_b S^{1/3}\big) + (D_N) \tag{6}$$

where D is the computed diameter, x is the branch order, N is the higher order (trachea being highest), $R_b\, S^{1/3}$ is the Strahler-based ratio, and D_N is the diameter of the highest order branch. While not contained within this thesis, continual advancements have been made with this modelling technique to include curvilinear mesh-models, along with physiologically appropriate lobar boundaries.[73]

1.7.2 Single Compartment Lung Mechanics Modelling

As mentioned previously, FOT measures the ratio of pressure to flow referenced at the airway opening, which is defined as the respiratory system impedance (Z_{rs}), a complex mathematical quantity. The real component (R_{rs}) largely reflects the resistive properties respiratory system and the imaginary component (X_{rs}) largely reflects the elastic and inertive properties of the respiratory system:

$$Z_{rs} = R_{rs} + jX_{rs} \tag{7}$$

If we model the respiratory system as a single compartment model as shown in Figure 1.4, we can derive an equation of motion pertaining to airflow throughout the system. With this model, we assume that the elastic recoil pressure (P_{el}) increases linearly with the volume of gas within the elastic sac described by E, and the pressure difference (ΔP) across the airway tube varies linearly with airflow ($\dot{V}$), described by R:

$$P(t) = P_{el} + \Delta \mathrm{P} = EV(t) + R\dot{V}(t) \tag{8}$$

For frequencies greater than that of normal breathing, we must consider the pressure required to accelerate the mass of air throughout the tube constituent ($\ddot{V}$). To account for this, we add an inertive term, I_r, to the differential equation above:

$$P(t) = EV(t) + R\dot{V}(t) + I_r\ddot{V}(t) \tag{9}$$

This equation can be reconstructed in the frequency domain by taking the Fourier transform of the above function where we use the notation $\omega = 2\pi f$ for convenience:

$$P(\omega) = \left(R(\omega) + i\left[\omega I_r - \frac{E}{\omega}\right]\right)\dot{V}(\omega) = Z(\omega)\dot{V}(\omega) \tag{10}$$

From the above equation we can separate out the real, and imaginary components, and use equation 11 to get:

$$X_{rs} = \omega I_r - \frac{E_{rs}}{\omega} \tag{11}$$

such that:

$$C_{rs} = \frac{1}{E_{rs}} \tag{12}$$

where C is the compliance. The single-compartment linear model (to model the entire lung) can model healthy-lung impedance very well,[64,74] but it lacks the ability to fit well with changes that occur with obstructive disease, which alters the Z_{rs} behavior with frequency, particularly increasing R_{rs} at low frequencies (<10 Hz).

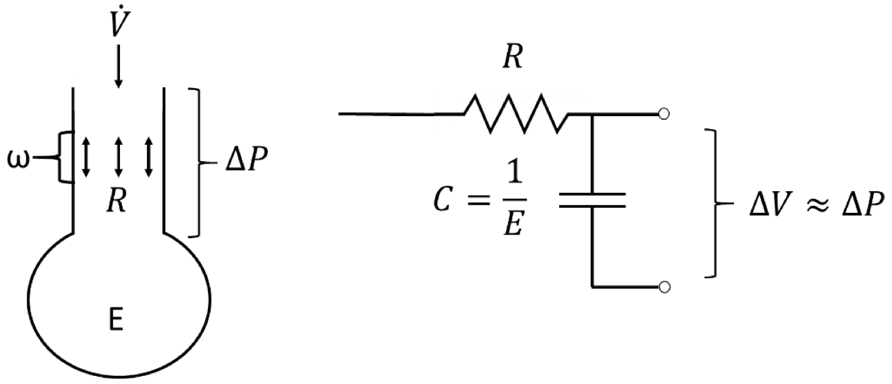

Figure 1.4 Modelling the respiratory system as a single compartment shown in tube and bag mechanical schematic (left) or as electrical analogue (right). The airway is divided into a tube, with a resistance which dictates airflow $\dot{V}$, across a pressure difference ΔP. At the end of the tube is an elastic balloon like structure to represent the elastic forces experienced in the lung parenchyma. This model is directly analogous to an electric RC-circuit, where the pressure drop is analogous to a potential difference.

1.7.3 Constant Phase Model

Pre-clinical studies of oscillometry with animal models revealed an inverse frequency dependence in resistance.[75] It was shown later that modelling of the tissue-compartment based upon an inverse power law had high fidelity with oscillometry measures up to 20 Hz.[76, 77] The following model was derived by modelling tension in response to a step displacement within the tissue compartment (acinus) with a power law:

$$T(t) = T_0 t^{-k} \tag{13}$$

where T_0, and k are constant. As in the previous section, the above expression can be transformed to the frequency domain, and expressed as a mechanical impedance of the tissue:

$$Z_{tis}(\omega) = F\{P * T_0 t^{-k}\} = \frac{G - iH}{\omega^{\alpha}} \tag{14}$$

where G represents tissue damping, and H represents the stiffness of the tissues, P is the pressure in the tissue compartment, and α is defined as:

$$\alpha = \frac{2}{\pi}\tan^{-1}\left(\frac{H}{G}\right) \tag{15}$$

with α typically less than unity in lung tissue.[78, 79] Adding the tissue contributions to the findings from the single compartment model, the impedance for this system would be:

$$Z(\omega) = R + i\omega I + \frac{G - iH}{\omega^{\alpha}} \tag{16}$$

grom this model, a parameter that can be defined is a term referred to as the hysteresivity (G/H), which relates how much proportion of tissue deformation goes into energy dissipation through frictional or viscous process compared to elastic energy storage. The form of the constant phase model provides a source of inverse frequency dependence in the R_{rs} spectra through $\frac{G}{\omega^{\alpha}}$. In healthy humans, the inverse frequency dependence in R_{rs} is only visible below 0.2 Hz.[80,81] Although in disease, this inverse frequency dependence is also seen in the typical FOT range (5-32 Hz). While the constant phase model can account for frequency dependence of Rrs observed in lung tissue, it does not necessarily mean that freqeuncy dependence is a tissue-based property. Frequency dependence of resistance in humans is usually attributed to heterogeneity and can be described using two or multicompartment models described in the next section.

1.7.4 Impedance Modelling and Asthma

While complex models such as the six-element model[82] or multi-branch models have been derived to simulate the mechanics of the entire respiratory system, the single compartment model or constant phase model still dominate in the literature due to their ability to be informative. For example, an early and common model for the respiratory impedance in asthma is the two-compartment model which consisted of two single compartments in parallel; the model was then compared with measured impedance in dogs after the administration of histamine in the frequency range of 8 to 2048 Hz.[83,84] In this thesis I use a multi-branch airway tree model which were introduced in section 1.7.1, which at it's terminal branches each includes a distinct single compartment.

1.7.5 Cost Function Minimization and Parameter Optimization

This thesis will require a procedure to determine the level of narrowing for a cluster of airways in a multi-branching airway tree that leads to the closest match to the measured ventilation pattern. In addition, we will be seeking solutions that best predict measured impedance as well. This is an optimization problem in a multi-parameter space since the many interconnected airways can have many different configurations of airway narrowing. In this section we introduce optimization in multivariate problems, and then describe simulated annealing which is the approach adopted in this thesis. The mathematical premise of any optimization procedure is that there is a functional form, f, that describes the cost of a system, A; and we seek a parameter set, β_0, such that:

$$f(\beta_0) \leq f(\beta), \;\; \beta_0 \epsilon A, \;\; \beta \epsilon A \tag{4}$$

In complex systems, like mechanical models of respiratory system, parameters are intrinsically linked with multiple similar configurations, which means that descent-optimization techniques like the Gauss-Newton algorithm can get trapped in local minima of the objective function and fail to find the global minima.

1.7.6 Simulated Annealing

While iterative techniques have the potential to get trapped in local minima of large sized solution spaces, heuristic methods can explore the interdependence of variables on global optimization. One such technique is simulated annealing which started with the concept of the travelling salesman problem, where the cost of a salesman travelling between N cities is minimized via combinatorial optimization.[85-87] The formalism for applying simulated annealing was initially introduced by Kirkpatrick et al.,[88] which is rooted in statistical mechanics, and states that the probability of a system being in a state with energy E with temperature T, would satisfy the Boltzmann distribution:

$$P(E,T) = \frac{1}{\sum_i e^{-\frac{E_i}{k_B}T}} e^{-\frac{E}{k_B}T} \tag{21}$$

where k_B is the Boltzmann constant: 1.38 x 10^{-23} $m^2 * kg * s^{-2} * K^{-1}$ and in simulated annealing this constant is omitted, and the form of this equation is simplified:

$$P(\Delta E,T) = e^{-\frac{\Delta \mathrm{E}}{\mathrm{T}}} \tag{22}$$

This equation will go to unity at high T, meaning all states are equally likely. As T decreases, the probability of states occurring is lower; representative of a fine-detailed search of the cost-function landscape to find a global minimum. For the purposes of a cost-function minimization problem, this technique improves on other optimization frameworks by occasionally allowing for worse solutions at high T, i.e, enabling the system to jump out of local minima. Iterative cooling of the temperature is implements, which puts more stringent tolerances on accepting “worse” solutions.

In the form presented above, simulated annealing has apparent limitations: (1) the probabilistic criterion of solution acceptance leads to the potential of escaping the global minima, and not return due to cooling nature of the technique. (2) Slow cooling is the only way to overcome (1), and this becomes computationally expensive. Adaptive cooling schedules have been developed that address these limitations,[89,90] albeit these techniques were not implemented in this thesis. In Yang et al., they proposed a guided annealing schedule where the temperature, T_g, is as follows:

$$T_g = \alpha T + (1 - \alpha)d^* \tag{5}$$

where T is the current temperature of the system, and is cooled in the conventional way:

$$T = \gamma T_{prev} \tag{6}$$

where γ is the cooling rate, and T_{prev} is the temperature of the previous iteration. The term d^* is a function used to track performance of the optimization, and can be defined in various ways; for which they chose:

$$d^* = \|x_e - \hat{x}^*_{curr}\| \tag{7}$$

where x_e is current evaluation of the cost, and $\hat{x}^*_{curr}$ is the lowest evaluated cost thus far. The term α is referred to as the information-effectiveness parameter and is defined as:

$$\alpha(T) = \left[1 - \exp\left\{-c\left(\frac{T}{T_{ini}}\right)\right\}\right] \tag{8}$$

where T_{ini} is the temperature of the system at the beginning of simulated annealing, and c is an adjustable parameter used to control the effectiveness of feedback. They were able to show that information guided simulated annealing improved over conventional simulated annealing, with or without a reheating schedule, by quantifying the number of simulations that were trapped in local minima for common optimization problems (Griegwangk, Rastrigin, and Schwefel function respectively).[89]

1.8 Motivation

The motivation for this thesis is as follows. MR ventilation images of an asthmatic lung can be used to determine the percentage of the lung not participating in ventilation; which is thought to be the result of small airway narrowing. A broad review of recent literature has revealed that the average VDP for a healthy subject is ~ 4.2 ± 5.4%, and ~ 10.0 ± 6.7 % for a severe asthma.[29,39,41,91-93] The obstruction of an airway (which is thought to cause a ventilation defect), which consequently blocks access of an FOT oscillation to sense the soft elastic tissue behind the obstruction, should cause reactance/elastance to stiffen proportionately. Analyzing a simple multi-branching airway tree model with thirty-two acini as shown in Figure 1.5, the absence of an acini can be shown to affect the overall stiffness of the lung. Assuming a chest-wall elastance of 10 $cm * H_2 0 * L^{-1}$, and an equal stiffness distributed to all acini, the elastance of a healthy lung as shown in Figure 1.5.A can be calculated:

$$E_{healthy} = \left(\frac{1}{E_1} + \cdots + \frac{1}{E_{31}}\right)^{-1} + E_{cw} = 40\ cm * H_2O * L^{-1} \tag{27}$$

Using one standard deviation from the mean VDP of severe persons with asthma (~16%) as depicted in Figure 1.7.B, the elastance is calculated to be:

$$E_{healthy} = \left(\frac{1}{E_1} + \cdots + \frac{1}{E_{27}}\right)^{-1} + E_{cw} = 44.4\ cm * H_2O * L^{-1} \tag{28}$$

This is an observed 11.1% change in elastance from health to severe disease, which is significantly less than the 400% change interpreted from low frequency (4 Hz) FOT.[94] To achieve this same change in elastance with the lung model depicted in Figure 1.5, a VDP of 80% would be required. It is important to note that MRI ventilation defects are derived from imaging acquired in the supine position which causes the abdomen to shift upwards, increasing R, and decreasing E. In severed obesity, E can be increased two-fold in the supine-position compared with upright.[95] While postural positioning does account for an appreciable change in stiffness of the lung this is still insufficient to account for the disparity between predictions of lung mechanics by MRI, and measured oscillometry. In asthma, the reason for the difference in the relative decrements of lung function compared to health as measured by MRI and oscillometry is currently unknown, and I am not aware of any studies that have investigated this. Asthma includes other factors apart from airway narrowing that could contribute to higher stiffness that may not produce ventilation defects. This includes potentially increased tissue stiffness from the higher elevated smooth airway muscle tone associated with asthma,.[96] The higher baseline tone can lead to an increase in stiffness of the lung tissue highly localized to the airways within the parenchyma, a manifestation of airway tissue parenchymal interdependence.[97,98] However due to the parallel nature of the lung tissue, this effect is likely very small compared to the changes in stiffness measured by oscillometry in asthma.

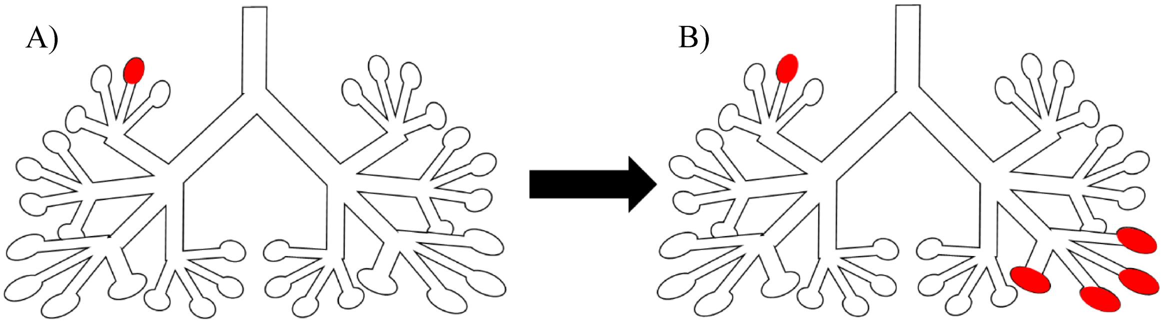

Figure 1.5 A multi-branching airway tree with a VDP of ~ 4% (A), and a VDP of ~ 16% (B).

1.10 Functional Image Modelling with Impedance Models of Asthma

Several decades of investigation with animals and computational models have indicated that heterogeneous small-airway derecruitment in asthma is a major contributor to decrements in lung function as predicted increases in R_{rs} and more negative values of X_{rs}.[78-79, 99-102] This is known to be heterogeneous from pathology, but also more recent techniques such as studies from multi-breath washout also confirm heterogeneity is strongly associated with asthma.[103-105] Connecting heterogeneous pathology and small-airway dercruitment in asthma, impedance models have been developed using functional information from inhaled gas imaging by imposing closures in multi-branching bronchial tree models. The functional participation of changes in airway diameters in asthma was also investigated by simulating ventilation and predicting impedance with a concept known as image functional modelling (IFM).[99,100] IFM is a technique that simulates the mechanics of a system, altering internal parameters such as diameters in an effort to explain function, including both impedance and ventilation distribution using imaging data. For this thesis, IFM was further developed to simulate the inhalation of gas and was compared to measured inhaled gas MR images.

The first study of IFM used inhaled gas PET to guide the location of airway closures within a multi-branching airway tree model; the simulated ventilation produced by the tree allowed them to predict the size of airways responsible for the presence of ventilation defects seen in asthma.[99] To accurately simulate observed ventilation defects, closures to airways < 2.39 mm were required; this is consistent our understanding of asthma being a small airway disease. A following investigation used inhaled-gas MRI to similarly guide the location of binary closures (i.e. dividing the lung into two regions, non-defect and defect within which airways are effectively closed) within a bronchial tree but required the addition of a normal distribution of narrowing to upper airways to account for additional impedance to matched subjects' measurements.[100] Common to both studies was the concept of a binary closure to the airway tree, where airways that fell within defects from the ventilation image were closed to 70-90% of their initial diameter. While using the additional Gaussian distributed narrowing in the ventilated regions predicted impedance that matched well with subjects' measurements, this method produced substantial and unexplained differences between the real ventilation images from MRI and the simulated ventilation images as shown in Figure 1.6. The top row of Figure 1.6 demonstrates three central slices of an inhaled gas MR image of one subject, the middle row depicts the same slices of simulated ventilation images produced from a computational airway tree model with a 70% closure to airways within defects, and the bottom for the same tree with 90% closures. The locations of defects are not correct, which could be attributed to the airway tree registration. But, more importantly, the signal intensity pattern of ventilation in ventilated regions is significantly lower than measurement.

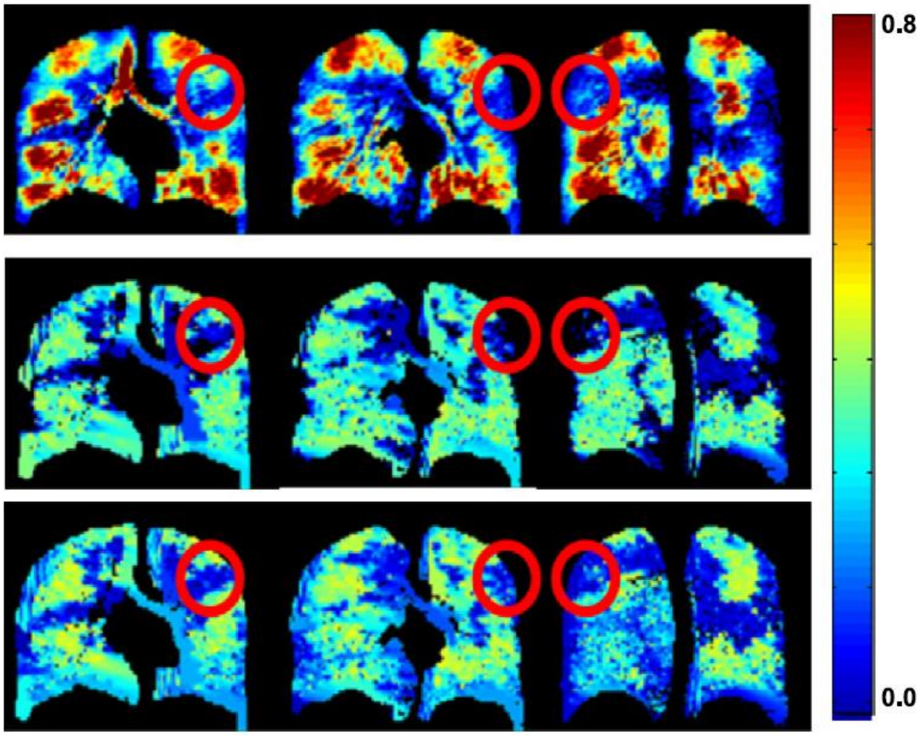

Figure 1.6 Real (top) and simulated ventilation images for three middle lung slices. The middle row represents simulated ventilation where defect airways were narrowed by 90%. The bottom row represents simulated ventilation where defect airways were narrowed by 70%. Red circles highlight differences in defect location/size.[100]

1.11 Hypothesis

The common approach for modelling mechanical impedance in asthma is to employ a binary closure of 70 to 90% airway narrowing airways that fall within the “defect” regions of inhaled gas images; a visual depiction of one such closure map is as seen in Figure 1.7. However, additional constrictions to pre-defined airways generations based upon a normal distribution have also been required to measured subjects’ impedance, sacrificing the functional participation of airways in predicting realistic ventilation. The multiple levels of ventilation within the inhaled gas images were largely discarded when converted only to binary information of regions with or without ventilation, and thus did not contribute to guiding airway narrowing. To examine how important this information might be, and to investigate the complex, and heterogeneous ventilation distribution in persons with asthma, we propose that a higher-level constriction scheme must be realized. As demonstrated by Kirby et al.,[38] k-means clustering is an approach to segment ventilation levels into clusters, which were matched with expert chest radiologists’ opinions of functionally significant differences in ventilation.

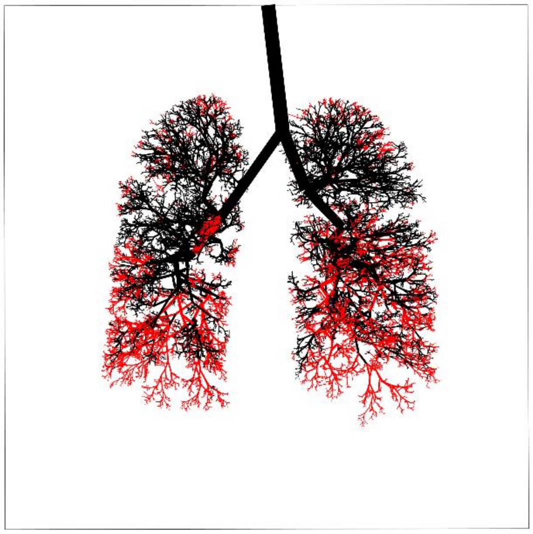

Figure 1.7 A 3D model airway tree with defect airways derived from inhaled gas MRI in red. Conventionally asthmatic modelling approaches would narrow these airways by 70-90% to respiratory mechanics.

General Hypothesis

We hypothesize that the hypointense to hyperintense signal levels in inhaled gas MR images can be used to guide a graded narrowing scheme in a multi-branching airway tree model that will improve on previous binary closure models to simulate ventilation images and impedance data in asthma

Specific Hypotheses

1) We hypothesize that simulated ventilation images predicted from a graded narrowing model will closer match measured ventilation images as assessed by reduced sum of squared differences in image intensities when compared to a binary model.

2) We also hypothesize that a graded airway narrowing model will predict a larger change from baseline R_{rs} and X_{rs} as assessed by a t-test at 5Hz. Also, we predict that the graded model will

predict impedance vs. frequency that is closer matched with measurement compared with the binary closure model; This was assessed by subjective comparison of Zrs of both graded and binary models by the increase of R_{rs} from baseline, and their statistical differences between models by t-test, as well as the subjective presence and extent of frequency dependence in R_{rs} This was also assessed by the difference between binary and graded scheme in the decrease in reactance from baseline, and subjectively by the rate of increase of X_{rs} as it more closely resembled measured $X_{rs.}$

3) We also hypothesize that the graded airway narrowing model will exhibit a larger inverse frequency dependence in the resistance spectra as quantified by the difference in resistance at 5 Hz to the resistance at 20 Hz, as assessed by a t-test when compared with predictions from the binary model.

1.12 Preliminary Development of a Time Constant Map for the Lung

A study performed by Kaminsky and colleagues (2000) found that the average peripheral airway resistance of seven persons with asthma was 11.9 +/- 2.28 cm-H_20-s-L^{-1} compared to 3.49 +/- 0.82 cm-H_20-s-L^{-1} for seven healthy participants with comparable demographics.[106] Regions fed with narrower airways (higher resistance) would take longer to fill than others, which embodies the idea that ventilation heterogeneity has an associated distribution of time constants in the lung and governs regional and heterogenous ventilation. We speculate here that the development and visualization of a time constant map over the lung derived from the ventilation data could help provide insight into scale of the heterogeneity present in the lung, presenting it in the familiar units of time rather than image intensity. Thus, new understanding of the scale and nature of the heterogeneity might be learned of the functional behaviour of the lung during inhaled gas imaging, and potentially present during breathing.

Chapter 2. Experimental Methodology

In this thesis, oscillometry and imaging data previously obtained from larger studies within the Parraga lab was used. Eight subjects (59 +/- 7 years), half male (weight = 86 +/-3 kg, height = 178 +/- 6 cm), half female (weight = 80 +/-10 kg, height = 164 +/- 3 cm), provided written informed consent to ethics board approved protocols (https://clinicaltrials.gov, NCT02351141, NCT02263794). These subjects exhibited severe clinical asthma based upon the Global Initiative for Asthma,[17] with a VDP range of 2-34 %. MR Images, and FOT were taken at baseline, and after administration of salbutamol (bronchodilator). The demographics for these subjects are as shown in Table 2.1

Table 2.1 Demographics of subjects measured with FOT, MRI, spirometry, and plethysmography.

Subject	Age	Sex	Height (cm)	Weight (kg)	BMI (kg/m^2)	FEV1 %pred	VDP (%)	Severity
S1	68	M	180	87.9	27.1	105	7.0	Severe
S2	56	M	185.5	86.7	25.2	37	31.5	Severe
S3	48	M	171.5	87.5	29.8	78	9.9	Severe
S4	66	F	161	63	24.3	54.6	16.5	Severe
S5	67	F	167	83	29.8	56	11.6	Severe
S6	60	F	163	88	33.1	37	29.2	Severe
S7	54	F	163	88.2	33.2	50	38.0	Severe
S8	53	M	173	80.5	26.9	27.9	30.7	Severe

2.1 Forced Oscillation Technique

Oscillometry was previously collected using a tremoFlo™ C-100 Airwave Oscillometry System™ as shown in Figure 1.3 by superimposing a multifrequency oscillatory pressure waveform of approximately 1-2 $cm * H_2O$ with a subject's normal breathing, over the course of 16 seconds. The waveform delivered oscillations at 5, 11, 13, 17, 19, 23, 29, 31, and 37 Hz. The impedance, Z_{rs}, was calculated by taking the fast Fourier transform of pressure and flow signals and computing the ratio of the spectra as the average of 1 second overlapping windows and for signal processing, a Hamming window with a 50% overlap was applied to the one-second windows prior to averaging from a single 16 second measurement, and 3 measurements were then averaged for the final Zrs, and accepted if the coefficient of variation for Rrs at 5 Hz was less than 15%. Any negative resistances of any window or outliers of greater than 3 standard deviations were rejected from an individual 16 seconds recording and a coherence of ≥ 0.90 was used as an acceptance criterion; where a coherence of 1.0 assumes perfect linearity between the measured pressure and flow (meaning the absence of noise). As per ATS/ERS guidelines, subjects wore a nose-clip during measurements, and supported their cheeks with their hands to minimize the upper airway shunt impedance.[64]

2.2 Hyperpolarized ^{3}He MRI

The MRI scans utilized in this study were acquired with a 3 Tesla Discovery MR750 system (General Electric Health Care; Milwaukee, WI). During the procedure, subjects inhaled a 1.0 L gas mixture of $^3He/N_2$ from functional residual capacity (FRC), and the images were taken under breath-hold conditions (total scan time: 16 s) in the supine position. A whole-body radiofrequency coil was used with a fast gradient-recalled echo method with partial echo (TR/TE/flip-angle = 3.8 msec/1.0 msec/7^0; FOV = 40x40 cm^2; matrix = 128x128, zero padded);

partial echo percent 62.5%, BW 62.5 kHz, one excitation, 14 sections (section thickness = 15 mm). Scans were performed with a rigid linear bird-cage transmit/receive chest coil (RAPID Biomedical GmbH, Wuerzburg, Germany). ^{3}He gas was polarized with a commercial exchange polarizer system (Polarean Inc, Durham, NC) to 30-40%. Images were segmented using software generated from MATLAB R2007b (The Mathworks Inc., Natick, MA). The inhaled gas ^{3}He MR images were clustered using a hierarchical k-means clustering method as described in section 1.6.2.

Chapter 3. Modelling Methodology

3.1 Airway Tree Registration

For this thesis, a 3D multi-branching airway tree with 64,895 airways, and 32,447 terminal airways was used for modelling. This model was developed from a HRCT of the lung from of a single subject, where airways diameters and junctions were derived. From the central airways, the peripheral airways were created using a fractal growing algorithm to the edges of the thoracic space, as described in section 1.7.1.[72] To model asthmatic physiology in the computational airway tree model, we used gradations in signal intensity within hyperpolarized ^{3}He MR images to apply local narrowing in the tree. To do this, we registered the 3D airway tree to a subject-specific MRI lung volume and is described fully in the following sections.

3.1.1 Point Cloud Registration

We implemented a rigid point-cloud registration using the function pcregrigid in MATLAB (MathWorks, 2017a) to move the airway tree into the MRI lung volume separately for the left and right lung. This function performs rotations and translations in 3D (x,y,z) to minimize the differences between two distributions of points. The MRI lung space (coronal slices) was defined by its boundaries, and a MR point-cloud volume was created by distributing the slices within the MR data set throughout the extent of the 3D airway tree dimensions. E.g, the positioning of the i-th slice would be:

$$P(i) = (i-1) * \frac{T}{N} + \frac{T}{2N} \tag{29}$$

where i is the slice number, T is the thickness of the lung (as determined from the coronal resolution of MRI), and N is the number of slices. As shown in Figure 3.1 below, the airway tree (black dots) was registered to MRI point cloud volume; where a separate registration was performed for the airways in the right lung of the tree with the right MR lung (red dots), and similarly for the left MR lung (blue dots).

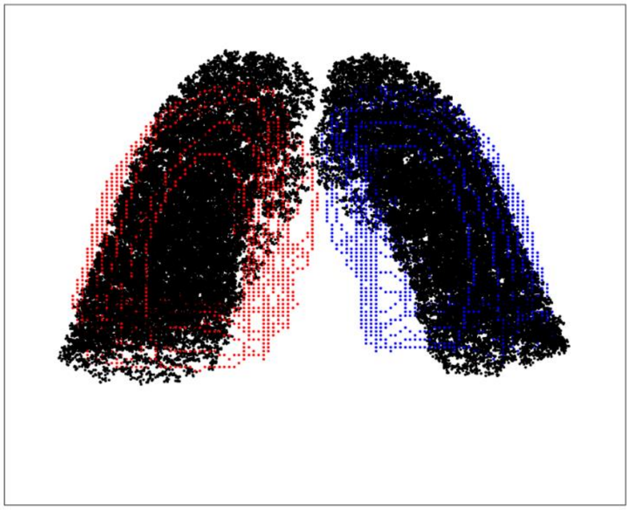

Figure 3.1 Rigid registration of the 3D airway tree model (black), to the MRI lung volume for one subject. The left lung (blue), and right lung (red) are registered separately.

3.1.2 TLC to FRC scaling

We scaled the airway tree lengths, and diameters from TLC, where the tree was derived, to FRC + 1.0 L. This was done to properly model the mechanics of the lung during the same state at which ventilation images were acquired. A scaling function that is airway-generation dependent was utilized:

$$L_{fac}(n) = \frac{\alpha}{1 + \left[\frac{d(n)}{d_p}\right]^{-\beta}} \tag{30}$$

where d is the diameter of the given airway, d_p is a threshold to differentiate small airways, and α and β are model parameters that can vary. This sigmoidal scaling function was derived to reflect the scalability of various airway generations based upon their cartilaginous structure and has a graphical form as shown below in Figure 3.2. In this figure, the scaling function for the airways lengths are shown where longer/larger airways are scaled less than smaller airway [84,107]

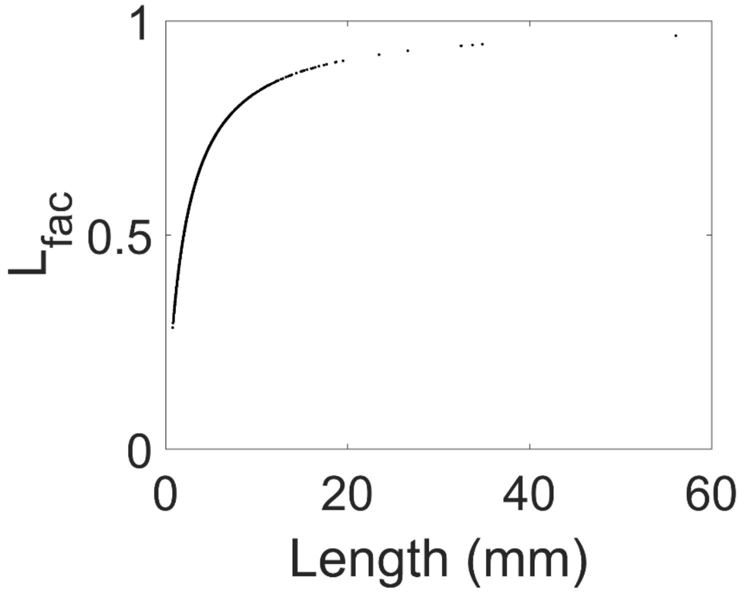

Figure 3.2 Scaling function for airway lengths to scale lung from TLC (large length) to FRC.

The scaling parameters $\alpha = 1$, $\beta = 1$, and $d_p = 2$ mm were chosen to scale airway lengths for all subjects, whereas variable α and β were chosen to scale airway diameters. The choice of α and β was made to predict a baseline (healthy) lung resistance that was 50-60% lower than the subjects' measured resistance. This threshold was chosen because it was the observed difference between healthy subjects and persons with severe asthma by Calvacanti et al.[94] Also, these parameters were chosen to synergistically match the demographic predictions of the subjects' X_{rs} at 5 Hz (further comments below).[108] The different scaling functions for airway diameters of the 8 subjects in this study are shown in Figure 3.3, where each subject required different scaling to achieve baseline conditions. This plot shows that the majority of subjects required upper airway dilation to meet baseline predictions, and likely means that the tree in this study was smaller than the trees of the actual subjects.

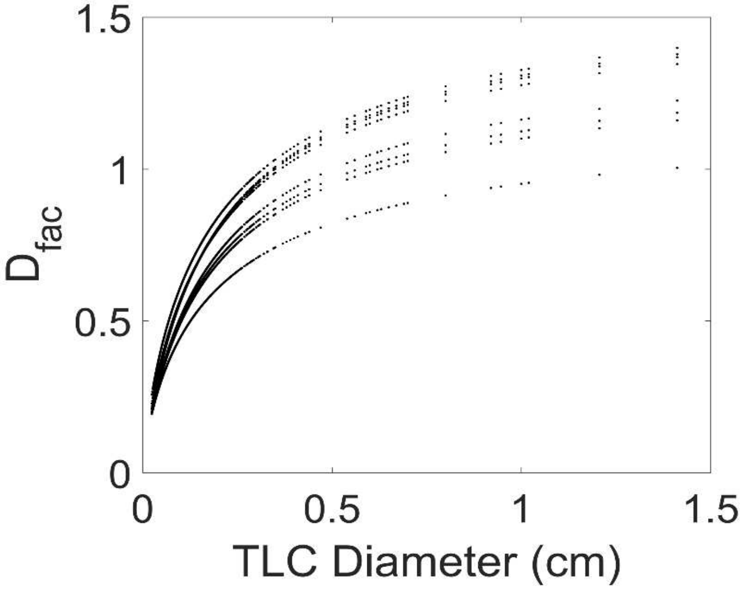

Figure. 3.3. Scaling function for airway diameters of eight different subjectss, to scale lung from TLC to FRC.

The results of the registration for one such subject is shown in Figure 3.4, with lateral and medial registration errors still evident. Given that the scaling function was applied to the entire tree, we can infer that for some subjects (mostly male), the initial airway tree morphology was incorrect, i.e, the airway tree was derived from a slim person (small chest cavity), whereas the average male has a larger chest cavity. Further deformation was needed to improve the matching of the airway into the thoracic space, and this is addressed in the following section.

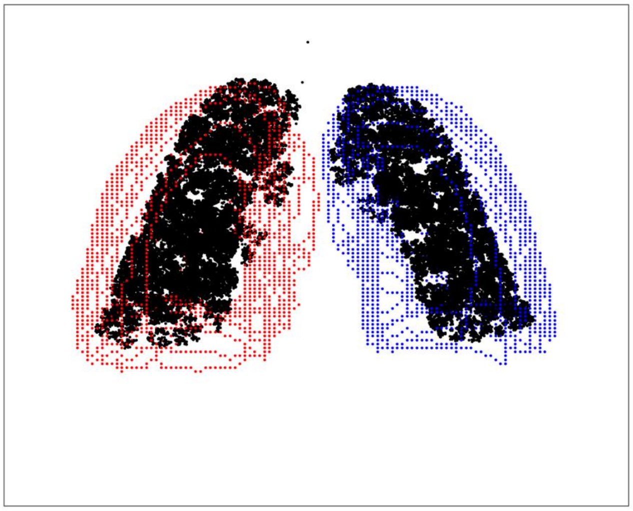

Figure 3.4. Registration of 3D model airway tree (black), to MR lung volume (red = right, blue = left) after scaling lung from TLC.

3.1.3 Deformable registration using MIND

Following scaling of the airway tree in the previous section, deformation of the tree was necessary to fill the subjects' MR lung space. This required the 3D tree to be mapped into image space (physical lengths/positions to pixel positions). Also, given the slice-format (single images) of the MR lung volume, the 3D lung-model had to be converted into a slice format as well. Using a similar logic from the previous section, airways were recruited into a given slice based upon their positioning. Exceptions were added to incorporate airways that were entering or leaving a given slice. After discerning the airways within the respective slice, the boundaries of the left and right lung space were determined separately, and a binary mask image was created for the airway space.

To deformably register the airway tree to the MRI volume, the slices of each respective volume were registered on a slice-by-slice basis, using a binary mask of the MR lung space. Also, the left and right lung were registered separately. Registration was performed using the modality independent neighbourhood descriptor (MIND) as outlined in Heinrich et al.[109] Briefly, the technique defines an image descriptor, which represents the structure of an image in a local neighbourhood. The descriptor for each voxel **x**, in image I, surrounded by a patch **r**, is defined as:

$$MIND(I,\boldsymbol{x},\boldsymbol{r}) = \frac{1}{n}\exp\left(-\frac{D_p(I,\boldsymbol{x},\boldsymbol{x}+\boldsymbol{r})}{V(I,\boldsymbol{x})}\right), \boldsymbol{r}\epsilon R \tag{31}$$

where R is the spatial search region. The patch distance, D_p(I, **x**, **x**+**r**) represents the difference between one patch around voxel **x**, and another patch at voxel **x**+**r**:

$$D_p(I,\boldsymbol{x},\boldsymbol{x}+\boldsymbol{r}) = C \star \left(I - I'(\boldsymbol{r})\right)^2 \tag{32}$$

where C is a convolution filter of size $(2p+1)^d$, d is the dimension of the image, and I' is a copy of image I translated by a distance **r**. The variance, V(I, **x**) represents the variance of the patch around the voxel of interest. After the descriptor (represented as a vector) is defined for each voxel, the similarity between the two images is defined as the sum of squared differences between corresponding descriptors:

$$S(I,J,\boldsymbol{x}) = \frac{1}{|R|}\sum_{\boldsymbol{r}\epsilon R}\left|MIND(I,\boldsymbol{x},\boldsymbol{r}) - MIND(J,\boldsymbol{x},\boldsymbol{r})\right|^2 \tag{33}$$

These values are then used to influence a deformable registration algorithm which utilizes a vector field **u** that minimizes the cost function below:

$$argmin\,(\boldsymbol{u}) = \sum_{\boldsymbol{x}} S\big(I(\boldsymbol{x}), J(\boldsymbol{x}+\boldsymbol{u})\big) + \alpha tr\big(\nabla\boldsymbol{u}(\boldsymbol{x})^T\nabla\boldsymbol{u}(\boldsymbol{x})\big)^2 \tag{34}$$

where I is the image to match, J is the image being deformed, and α is a diffusion regularization term that was chosen to be 0.05 for all subjects as it maximized registration. The cost function was solved using the Gauss-Newton optimization method, with an iterative over-relaxation technique to converge to a solution. The optimization produced a deformable vector field that deformed the airway tree to fill the MR lung-space. This deformation field translated voxels in coronal perspective of the airway tree volume. An example of one such registration is shown in Figure 3.5 below, where the right MR lung (red dots), and left MR lung (blue dots) images are represented as slices (as described above), and the black dots are the positions of airways within the tree. There were high registration statistics (> 0.85 fractional volume overlap described below) found in slices immediately prior to, and after the cardiac notch, but with deviations with lower ovelap still seen in the medial/lateral lung within the cardiac notch, as well as deviations in the far-most posterior and anterior slices. To quantify the quality of registration, a shape-matching metric, which we call the fractional volume overlap was used:

$$FVO = \frac{(A \cap B)}{B} \tag{35}$$

where A is the deformed image, and B is the image to match.

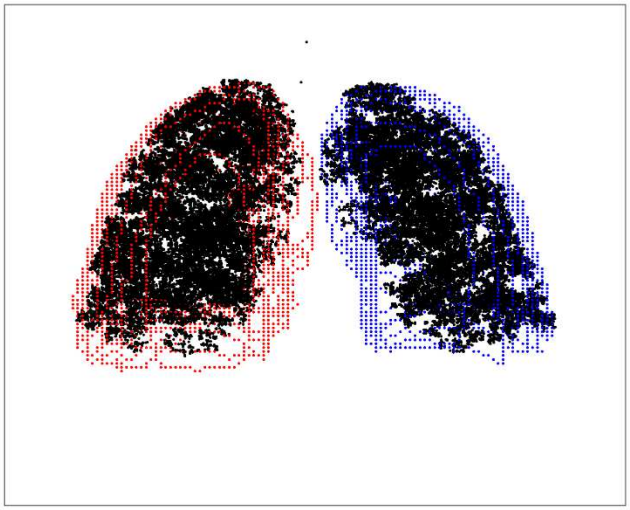

Figure 3.5. Registration of 3D model airway tree (black), to MR lung volume (red = right, blue = left) following deformable registration.

3.1.4 Registration Limitations

The final component of registration was ensuring the connectivity of the airway tree following deformation. Since the airways were segmented into individual slices, and the slices were deformed separately, connectivity of the tree from slice to slice could be lost as depicted in Figure 3.6.A, which shows airway generations 1 - 14 following deformation, where numerous subtending airway branch junctions were separated from parent branches. While the impedance of the tree could still be computed, the disconnected tree was not a realistic representation of the respiratory system. To reconnect the tree, a conditional framework for connecting the tree was implemented as follows. After registration, all airways throughout the tree were checked for connectivity of the left/right daughter branches first; if they were disconnected, they were forced to junction at the airway which falls within the lower ventilation level (to preferentially maintain location of defects during simulated ventilation). After this, the parent branches were checked for connectivity with the daughter branches and the following conditions were imposed: **if** the parent was not connected, calculate the potential length of the parent airway if connectivity was forced; **if** the length of the forced stitching does not exceed 150% of the maximum airway length within that respective airway generation: connect; **else** find all of the subtending airways from that parent, and translate them until the airways connect. As shown in Figure 3.6.B this conditional framework was able to successfully reconnect the airways of the tree and maintained a branch like appearance. But, this may have affected the location of the acini since some terminal airways were moved in this procedure. This solution could alternatively be deployed by stretching the central airways peripherally, which could have the potential of better registration statistics.

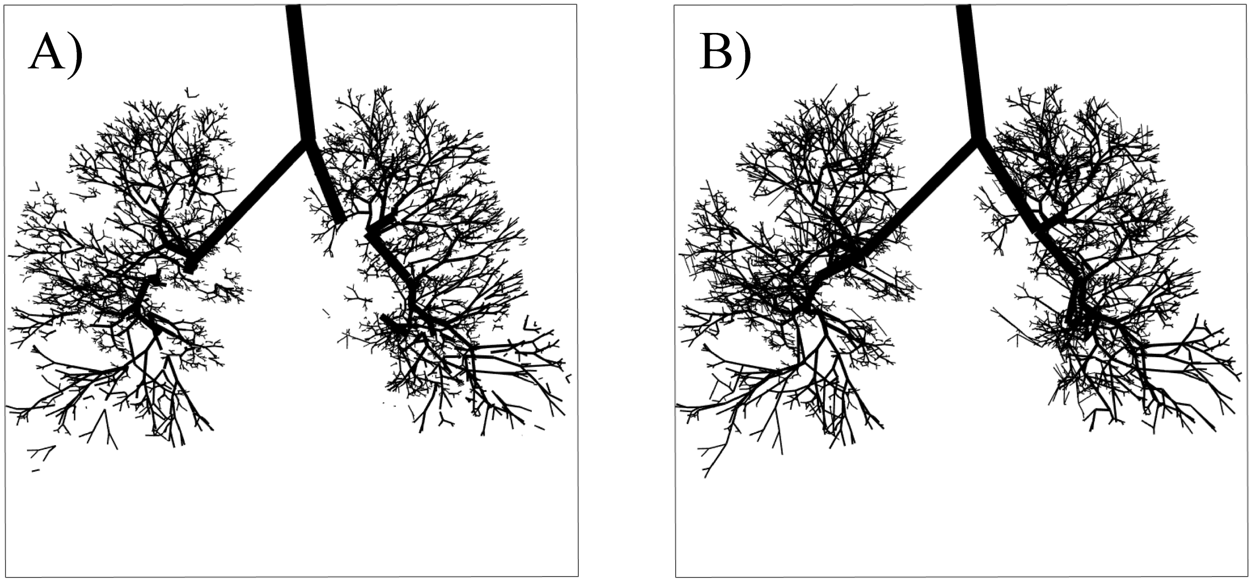

Figure 3.6. 3D Airway tree following deformation using MIND algorithm. (A) Generations 1-14 without stitching. (B) Generations 1-14 with stitching.

3.2 Impedance Calculations

To model the impedance of the airway tree, the impedance of individual airways was calculated, and then were added in parallel (at bifurcations), and in series (for each generation). The complex impedance of each airway was calculated with Womersely flow; which is derived from the Navier-Stokes equation for pulsatile fluid-flow. Womersely flow predicts both the inertive and resistive properties of any fixed tube with flow that is either laminar or approaches transitional/near Reynold's number (not fully turbulent), and thus accounts for all the expected flow regimes in the lung within the frequency region that was tested. The mathematical form is as shown below:

$$Z_a(f) = j\frac{2f\rho_{air}l_a}{r_a^2}\left[1 - \frac{2J_1\left(\alpha_a\sqrt{-j}\right)}{\alpha_a\sqrt{-j}J_0\left(\alpha_a\sqrt{-j}\right)}\right]^{-1} \tag{36}$$

where r_a is the radius, and l_a is the length of the airway, f is the frequency in Hz, ρ_{air} is the density of air (1.16 kg/m^3), J_1 and J_0 are the Bessel functions of order 0 and 1 respectively, and α_a is the Womersley number of the airway defined as:

$$\alpha_a = r_a\sqrt{\frac{2\pi\rho_{air}f}{\mu_{air}}} \tag{37}$$

where μ_{air} is the dynamic viscosity of humid air at 37°C (1.85 x 10^{-5} Pa-s). For terminal airways, a constant elasticity for the acinus added to the impedance; also, elasticity was homogeneously distributed to all acini in the tree model. While some heterogeneity in tissue properties might exist, asthma is not believed to be a tissue disease; i.e, the cause of ventilation heterogeneity is thought to be due to the heterogeneity in airway narrowing. For the terminal airways, the impedance is as defined below:

$$Z_{a,term}(f) = Z_a(f) + E_{tot} * N_{term} \tag{38}$$

where E_{tot} is the elastic contribution of all acini to the total lung elastance (stiffness), and N_{term} is the number of terminal airways (which terminate into an acinus). Given that impedance of the entire tree was determined from the parallel and series addition of impedances for individual airways, and we assume that elastance is homogeneously distributed to all acini, the elastic contribution for a single terminal airway would intuitively be the total elastance from N parallel additions of total measured elastance, E_{tot} multiplied by N_{tern}. Modelling a healthy lung with the methodology described above, we could reproduce measurements by Lui et al.,[110] as shown in Figure 3.7. In the left plot of resistance, the model (black dots), qualitatively matches well with the subject's measurements; and similar agreement is seen with elastance (right plot). E_{rs} is approximated from equation 11 by assuming I_{rs} is zero, which is not correct for high frequencies, and accounts for the descending E_{rs} after 2 Hz.

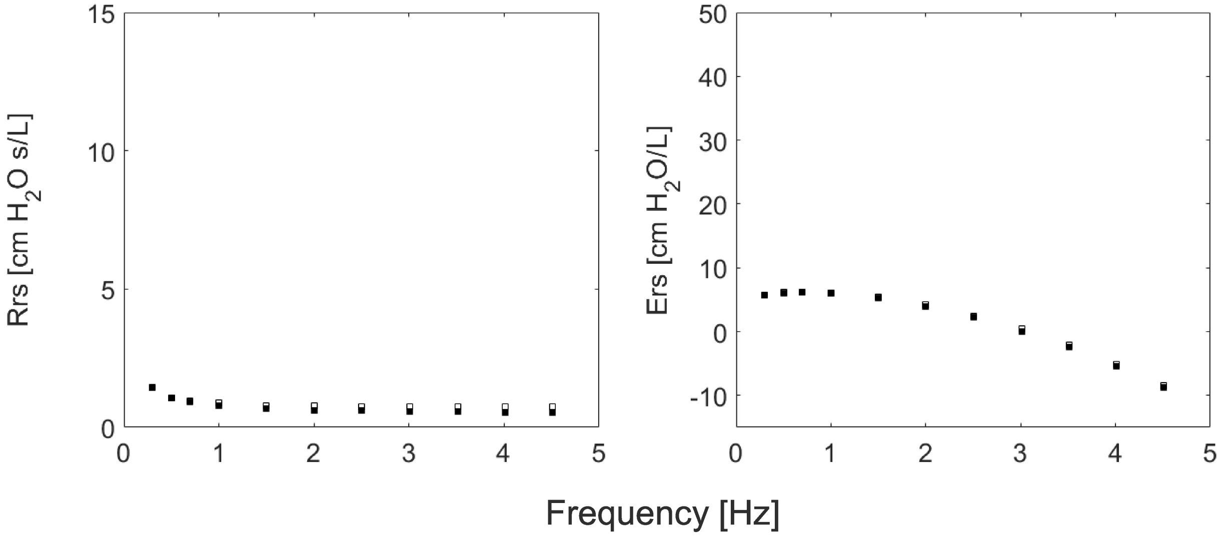

Figure 3.7. (Left) Resistance of a healthy lung, (Right) Elastance of a healthy lung using oscillometry. Model is depicted by solid squares, and measurement from Lui et al.. is depicted by open squares.[110]

3.2.1 Assumptions

After calculating the impedance of the entire airway tree, a few terms were added to realistically model the impedance of the entire respiratory system. To calculate the resistance of the lung, R_{re}, 0.5 $cm * H_2O * s * L^{-1}$ for the trachea and glottis, as well as 0.5 $cm * H_2O * s * L^{-1}$ for the chest wall was added to the airway tree resistance, R_{tree}, to reflective experimental observations:[101,102,111]

$$R_{rs}(x) = real\big(Z_{tree}(x)\big) + 1.0\ cm * H_2O * s * L^{-1}, \qquad x\epsilon f \tag{39}$$

where f is a discrete frequency measurement. Following this, a chest wall elastance of 10.6 $cm * H_2O * L^{-1}$ was added in parallel with the airway tree elastance: [112-116]

$$E_{rs}(x) = -2\pi x * imaginary\big(Z_{tree}(x)\big) + 10.6\ cm * H_2O * L^{-1}, \qquad x\epsilon f \tag{40}$$

And finally, a measured frequency dependent upper airway shunt impedance was added in parallel with the lung impedance to calculate the respiratory system impedance, Z_{rs}:

$$Z_{rs,i}(x) = R_{rs}(x) + i\left(\frac{E_{rs}}{2\pi x}\right), \qquad x\epsilon f \tag{41}$$

$$Z_{rs}(x) = \frac{Z_{rs,i}(x) * Z_{uaw}(x)}{Z_{rs,i}(x) + Z_{uaw}(x)}, \qquad x\epsilon f \tag{42}$$

where Z_{uaw} is the impedance of the upper airways as measured by Cauberghs et al.[117] The resistance of the upper-airway shunt at discrete frequencies for 16 subjects with obstructive lung disease can be seen in Figure 3.8, where shaded circles represent measurements with the cheeks supported, and open circles represent measurements with the cheeks not supported. Similar differences are seen in the reactance (X_{rs}) spectra.

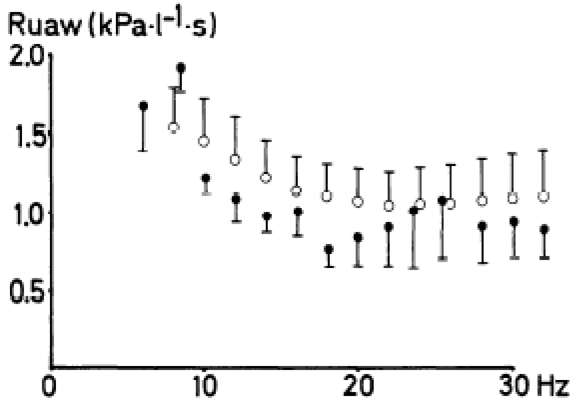

Figure 3.8. Upper airway shunt resistance (Ruaw) with cheeks supported (filled circles), and unsupported (unfilled circled) in 6 healthy subjects. Figure reproduced from Cauberghs et al.[117]

We used subject's demographics to predict baseline (healthy) X_{rs} at 5 Hz, where "baseline," reflects a healthy lung without the presence of defects, or obstruction:[108]

$$X_{rs,healthy,male} = 4 - e^{2.683-0.703*H+0.00185*W} \tag{43}$$

$$X_{rs,healthy,female} = 4 - e^{2.373-0.707*H+0.0015*A+0.00312*W}$$

where H is height in meters, A is age, and W is weight in kg. We matched these demographic predictions by choosing subject-specific variables in equation 30 and adjusting the elastance in the tree, E_{tot} in Equation 38. The values chosen for E_{tot} were within the range of observed values.[94,116,117]

3.3. Image Functional Modelling (IFM)

We aimed to deploy a graded narrowing scheme in a bronchial tree to simulate asthmatic physiology, where the degree of narrowing for individual airways was based upon local ventilation (derived from the MRI registration procedure). We implemented two techniques together to realize subject-specific narrowing schemes: IFM and simulated annealing. For simulating ventilation with IFM, we used a methodology similar Campana et al.[100] To implement IFM, we assume that gas was inhaled in one second during an inhaled gas MR acquisition and calculate the impedance of each airway at a frequency of 1 Hz. We then sum the voxel intensities for the entire inhaled gas MR image, and distribute the summed signal intensity (assumed to be the signal from 1.0 L of gas) throughout the tree, starting at the trachea, using a flow-divider relationship described by Colletti et al.,[118] where the resulting flow of gas distributed to each airway was dependent upon the resistance of the subtending branches:

$$\dot{V}_{left} = \frac{R_{right}}{R_{left} + R_{right}} * \dot{V}_{parent} \tag{44}$$

$$\dot{V}_{right} = \frac{R_{left}}{R_{left} + R_{right}} * \dot{V}_{parent}$$

This process was completed until the volume of gas in each airway was found as shown in Figure 3.9, where gas signal intensity, quantified in each airway, generally decreased with increasing airway generation since the total cross-section increased with increasing number of branches below about the 3rd generation. To produce the image, it was only important to consider the degree airflow (proportionally volume of gas) in the terminal airways, as this is the site of gas exchange, which is functionally observed with inhaled gas MRI.

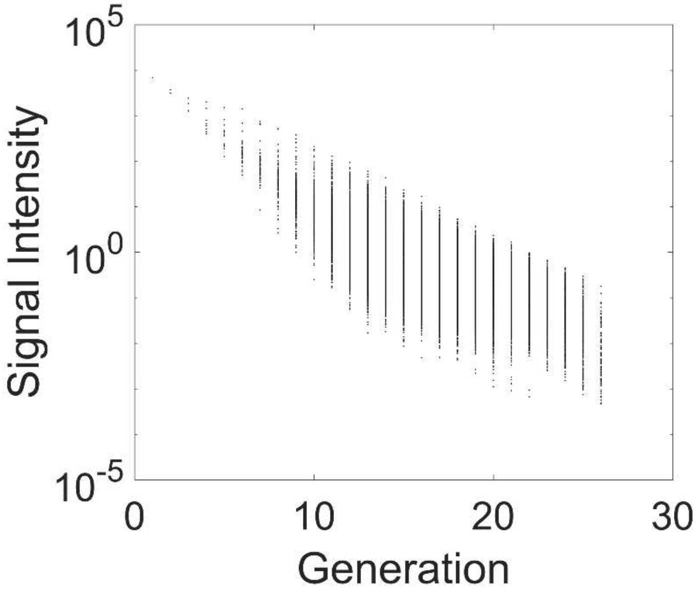

Figure 3.9. Signal intensity in each airway after implementing a flow-divider relation to distribute gas throughout an airway tree.

The methodology above assumes that the elastance at the end of all pathways were identical, thus other than the role of the pathway resistance not differentially affecting the effective time constant for filling. We then assign signal intensities derived from the flow divider relationship to a zero-filled matrix to create a ventilation image. Voxels that did not contain an acinus were assigned a signal intensity using a 3D nearest-neighbour averaging algorithm. Finally, to bring the simulated ventilation images closer in resolution to the inhaled gas MR images, a 3D median filter was applied. An example of this entire process is as depicted in Figure 3.10, where in Figure 3.10.A, voxels in a zero-filled matrix were filled with the local degree of ventilation in airways determined from the flow divider relationship; In Figure 3.10.B, the remaining zero-filled voxels were filled with a 3D-nearest-neighbour averaging algorithm and the entire image was smoothed using a median filter. Both model (Figure 3.10.B) and subject's ventilation (Figure 3.10.C) bear some similarity, but they are different. This is described later in section 5.3.

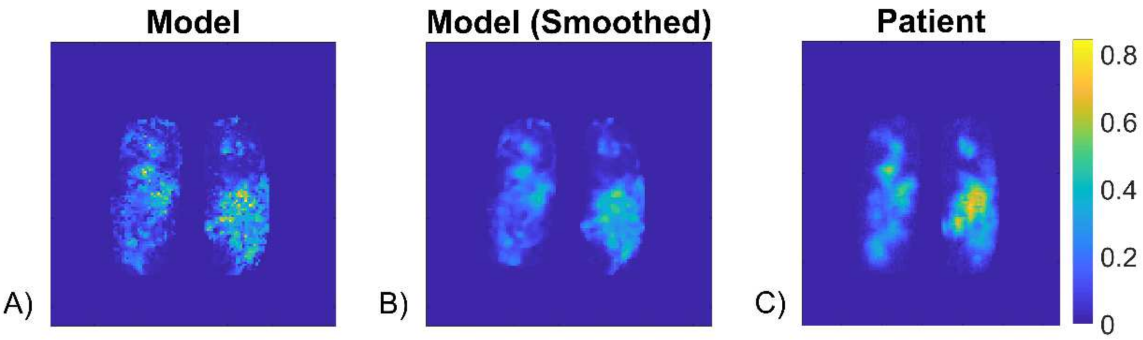

Figure 3.10. A visualization of the gas-map filling process for simulating ventilation. A) Shows the gas map filled with signal intensity values for acini that fall within voxels. B) Shows the gas map after voxels have been filled with a nearest neighbour averaging, and a median filter has been applied to the whole image. C) Subject’s ventilation image where voxel intensities have been normalized by the summed signal intensity for the entire lung.

A cumulative distribution function was then constructed from the simulated ventilation images with:

$$CDF(x) = \int_0^x f(t)dt \tag{45}$$

where x is the degree of ventilation found in a given voxel, and $f(t)$ describes the number of voxels with a given degree of ventilation.

3.4 Simulated Annealing

We used simulated annealing to realize the optimal narrowing scheme for reproducing the ventilation distribution seen with MRI. For simplicity, the sum of square differences (SSD) between each simulated ventilation image and MR image, which we refer to as the objective function (OF), was chosen to quantify the optimization of the graded narrowing scheme.

Deriving the appropriate cooling rate was accomplished by iteratively performing simulated annealing with larger cooling rates and qualitatively assessing the shape of the OF optimization. Solutions that converged too quickly, or did not converge at all, were discarded. From this assessment, the optimal cooling rate was found to be 1.5 % per iteration. For this thesis, the framework for applying simulated annealing is as shown in Figure 3.11.

Three different versions of simulated annealing were tested; in V1/V2 we only considered the optimization of a graded narrowing scheme for the terminal airways, as we believed the best possible way to match ventilation would be to apply localized narrowing to the smallest airways. This methodology limited our ability to match measured impedance, given that induced heterogeneity was restricted solely to terminal airways. In V3 two levels of simulated annealing was applied, where the first level optimized a graded narrowing scheme for the conducting airways, with the goal of improving impedance predictions by introducing structural heterogeneity throughout the upper airways; and the second level optimized a graded narrowing scheme for the terminal airways to maintain the quality of simulated ventilation. The technical difference between each version is related to equation 30, which scales the lung from TLC to FRC + 1.0L. Below is a description of the methodology for each version, and the motivation for attempting different methods. In V1 β in equation 30 was set to 1.0 while varying α and d_p, this restricted any airways from being dilated during the scaling, as one might expect when reducing lung volumes; but, since the airway tree is not that of the target subject, it is possible that some airway dilation could be needed, particularly in subjects with low impedance. This method did not provide useful baseline R_{rs}, nor did it match subjects' X_{rs} as it was less negative than the measured (obstructed X_{rs}). This motivated a new method for choosing parameters. In V2 we attempted to seek an appropriate scaling by varying all three parameters, allowing upper airways to constrict or dilate, and changing the inflection point in equation 30, which effectively defines a point where airways become more compliant and scale more easily with volume changes. This approach did not allow simulated annealing to come to solutions that had important impedance characteristics seen in persons with asthma like inversely frequency-dependent resistance. Thus, in V3 scaling was attempted by setting d_p equal to 2 mm while varying α and β which is similar to the scaling approach described by Habib et al.[84,107]. Simulated annealing was applied twice as previously described. In some subjects X_{rs} was still a too small negative curve, and thus some subjects benefitted by adjusting acinar stiffness to match X_{rs}. While this was performed on the final model tested of this thesis, from deeper analysis of the results, there were clear avenues for future implementations that are discussed on page 95. To quantity the performance of each version of simulated annealing, a metric called the performance index was borrowed:[99,100]

$$PI = \sqrt{\sum_{i}^{nf} \left(\left[R_{rs,p}(i) - R_{rs,m}(i) \right]^2 + \left[X_{rs,p}(i) - X_{rs,m}(i) \right]^2 \right)} \tag{46}$$

where $R_{rs,p}$ is the resistance of the subject, $R_{rs,m}$ is the resistance of the model, and similar subscripts are used to describe the reactance, X_{rs}; this metric is evaluated over the entire frequency range.

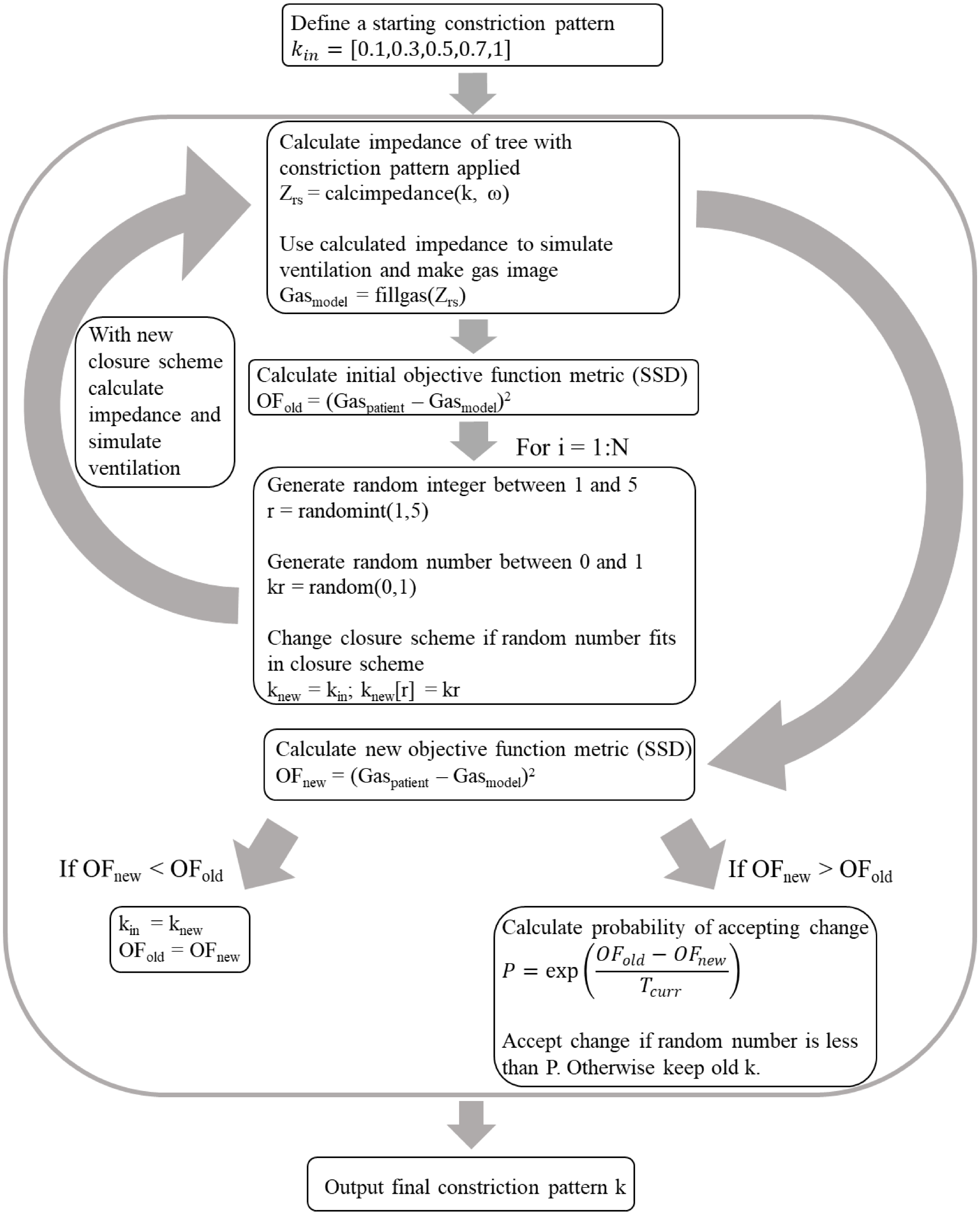

Figure 3.11. Application of simulated annealing where cost function minimization was based upon matching simulated and experimental ventilation images. The temperature was defined as the number of iterations N and is cooled every iteration by 1.5%.

3.5 Time Constant Map

The time constant of a ventilatory unit (the time it takes to be filled by 63.2 % of its' maximal volume) if filling is approximated by a single compartment and thus single exponential relationship can theoretically be calculated using the pathway resistance and tissue compliance via:

$$\tau = R * C \tag{47}$$

Given that computation of the pathway resistance may include effects of flow diversion or pendelluft to other pathways with different rates of filling, making the calculation of individual time constants from a distributed time constant map is highly complex; we will instead use the degree of ventilation within an inhaled gas MR as this is the actual filling achieved although it is the accumulated intensity and not necessarily following a single exponential behavior, thus as a model for the time for filling in a local region, assuming an exponential degree of filling via:

$$V = V_m\left(1 - e^{-\frac{t}{\tau}}\right) \tag{48}$$

where t is the time for an inhaled gas MR image acquisition (16 s), and V_m is assumed to be 63.2% of the maximum observed signal intensity.

3.6 Statistical Analysis

Following simulated annealing, we averaged the graded narrowing scheme solutions for the eight subjects in this study and performed a paired t-test between the degree of narrowing in the K(N) level to the degree of narrowing in the K(N+1) level and used a Bonferroni correction to test for a significant difference in the degree of narrowing between neighbouring K-levels. The same testing was also performed to evaluate improvements in ventilation between the binary model and the three version of simulated annealing with the graded narrowing model. Also, a paired t-test with a Bonferroni correction was used to evaluate significant improvements in the resistance at 5 Hz (R_5), the reactance at 5 Hz (X_5), and the difference between the resistance at 5Hz and the resistance at 20 Hz (R_{5-20}) for the graded narrowing model, compared with the binary closure model. A single factor ANOVA was then used to evaluate if there were significant differences in these metrics between the three versions of simulated annealing. If a significant difference was found, a Tukeys' Honest Significant Difference test was implemented to determine which differences were significant.

Chapter 4. Results

4.1 Image Registration

As described in the methodology on page 37, the registration of the airway tree to the host MR volume was quantified with the fractional volume overlap. Registration quality for the eight subjects pre- and post-salbutamol is shown in Figure 4.1, where we see that there was very little variation pre- and post-salbutamol respectively. In addition to the fractional volume overlap we calculated another common image registration metric known as the Dice similarity coefficient:

$$DSC = \frac{2|A \cap B|}{|A| + |B|} \tag{49}$$

where A is the deformed image, and B is the image to match. For the eight subjects, the DSC was calculated to be 85 ± 3 %, and there were similar differences between pre- and post-salbutamol.

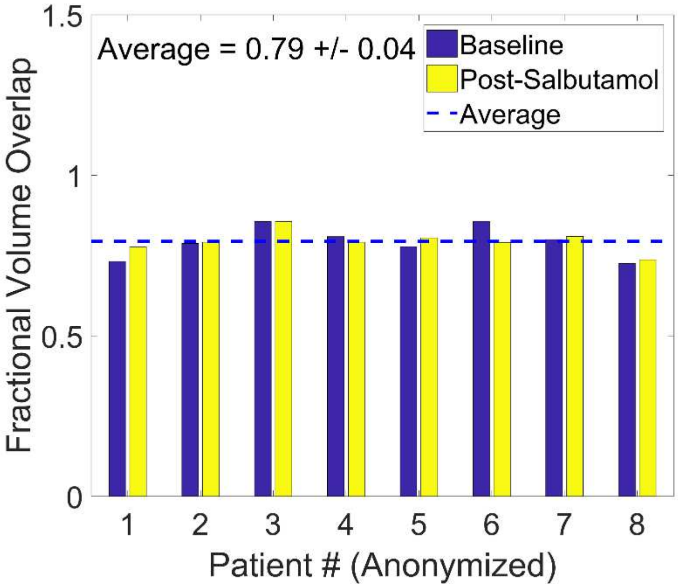

Figure 4.1 Fractional volume overlap following deformable registration framework of the same 3D airway tree.to eight different MR volumes.

By not forcing the connectivity of the airway tree, the average FVO was 0.81 ± 0.04 for the eight subjects. Using a paired t-test, the FVO was found to be significantly improved with a disconnected tree ($p < 0.005$). For the eight subjects, the largest translation of an airway to maintain connectivity of the tree was 96 mm, and the average translation within each of the eight subjects ranged from 3.4 – 14.9 mm. The airways that required the largest changes in position were typically contained within the most anterior/posterior slices following registration. For all subjectss there were clear boundaries that formed between some clusters of airways following the registration process. In Figure 4.2, there is an example of one such registration with gaps between clusters of airways. This tree appeared to exhibit physiologically reasonable separations between the apical and posterior segments of the superior lobe, however, there were some artificially large subsegmental gaps observed that formed as result of the registration process. Of course, the gaps will translate into an inability to properly quantify simulated ventilation within these regions and the impact of this is discussed in section 5.3.

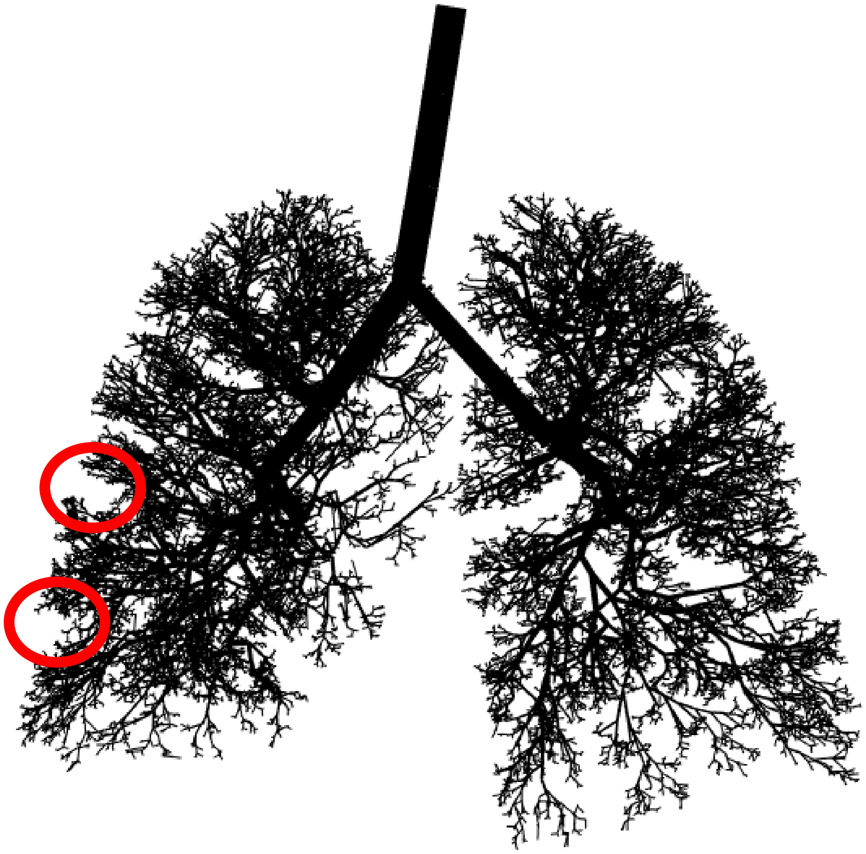

Figure 4.2 Airway tree of subject #1 following deformable registration, Red circles are representative of apparent sub-segmental boundaries post registration.

The fractional overlap evaluated on a slice-by-slice basis was typically > 0.85 in the middle of the lung and was markedly lower (< 0.60) in the most posterior and anterior slices. Although the smaller lung volumes contained within the posterior and anterior slices means that they contribute proportionally less to the overall simulated ventilation quality. Nevertheless, there are clear limitations in morphing the tree to a subject-specific volume with the proposed registration process. However, it was felt that registered the tree can still be used to make comparisons between the two models (binary vs. graded guided airway narrowing) on predicting asthmatic pathophysiology since the registration is common onto both. The impact of registration errors will be discussed on page 81-2 in the discussion.

4.2 Optimal Narrowing Scheme and Scaling Parameters

This section will describe the optimal subject-specific narrowing schemes derived with simulated annealing. Because the number of airways is large, and simulated annealing is a computationally expensive process, it was useful to develop boundary conditions that speed up the convergence with solutions that were physiologically reasonable. One boundary condition that seemed reasonable would be to enforce the degree of narrowing to be higher for lower K-levels, as it was expected that the degree of narrowing (airway obstruction) should be greater in regions of low ventilation (lower K-level). To derive these boundary conditions, simulated annealing was turned off (i.e, airway diameter closures were randomly chosen, and there was no manipulation of the variables in a pseudo-deterministic way to reduce the OF and improve the solution) and repeated for 5000 different solutions. This approach is limited to just analyzing the narrowing scheme that gave the lowest OF, rather than implementing simulated annealing to converge the system to an optimal solution. An example of the OF for successive iterations for one such subject is shown in Figure 4.3.A, and one can see that there is a wide range of values where a minimum OF level was delineated by the dashed red line. The 50 lowest OF are shown in Figure 4.3.B. The choice of 50 points was somewhat arbitrary, but the choice tended to give a consistent OF range of ~20 for all subjects; furthermore, these points were chosen to observe trends in the graded narrowing scheme for 'optimal' solutions to see if there were similarities across subjects.

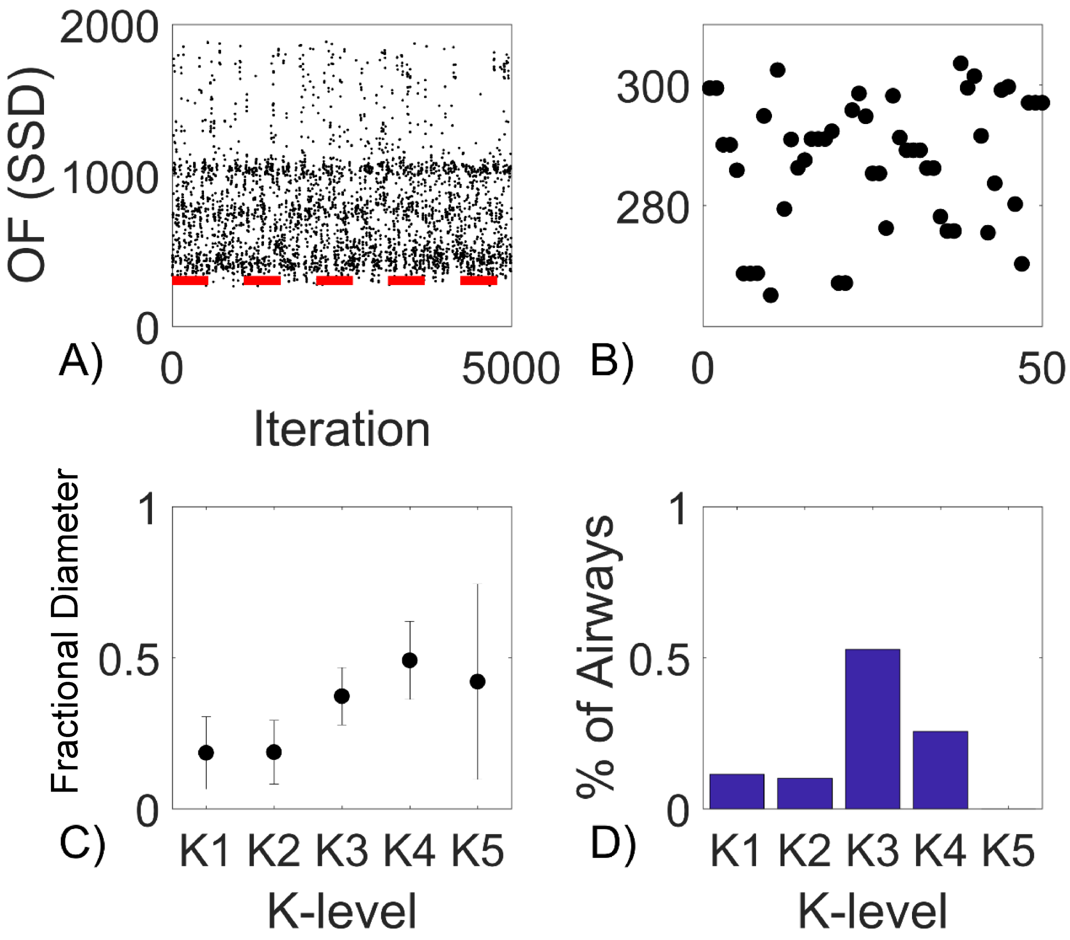

Figure 4.3. (A) The SSD between simulated and experimental ventilation for randomly generated closure scheme. (B) Taking the 50 smallest OF, illustrated by the red line in (A). (C) The mean constriction level for each K-level from the 50 points in (B). (D) The specific K-level distribution in the acini of this subject.

Taking the 50 lowest points and calculating the average graded narrowing scheme (the average ratios of each airways' final diameter to original baseline diameter within a respective K-level) for each K-level is shown in Figure 4.3.C, and the fractional diameter on average shows a decreasing trend with decreasing K-level, as was premised above. For this specific subject, the majority of terminal airways fell within the K3 level, while no terminal airways fell within the K5 ventilation level as is seen in Figure 4.3.D.

As shown in Figure 4.4, The mean fractional diameters for each K-level as described in Figure 4.3.C, was averaged across all eight subjects (black circles); Also, we calculated the same average narrowing scheme excluding three subjects who had 0% of their terminal airways in the K5 level (blue squares). Again, the trend exhibited a decreasing fractional diameter with decreasing K-level for all subjectss, where the fractional diameter in the K5 level was higher with the removal of the three subjects mentioned above. These findings were used to implement boundary conditions on potential changes to K-levels during simulated annealing, i.e, the degree of narrowing within the K(N) level must be less than the degree of narrowing in the K(N+1) level.

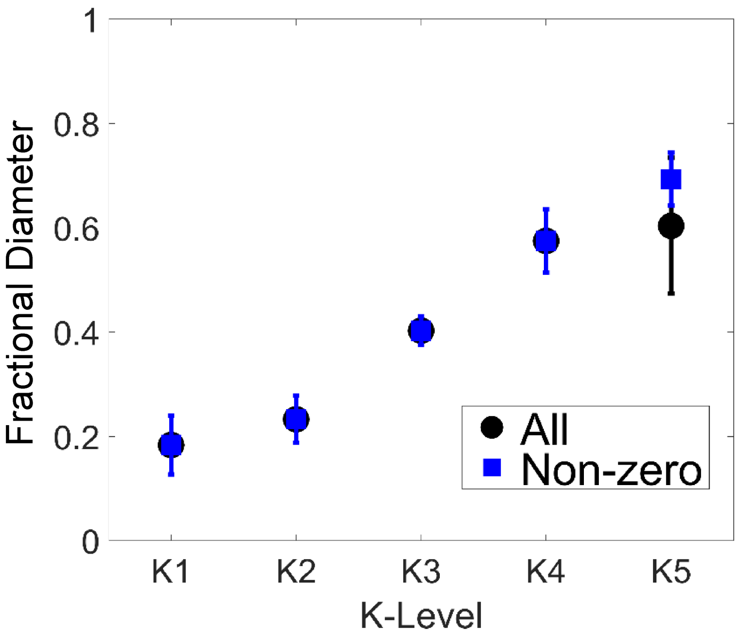

Figure 4.4. The constriction level for each K-level when averaging the findings of the 50 lowest OF points from each subject as demonstrated in Figure 4.3.C. The black dot includes all subjects, and blue squares exclude subjects whose airways did not include any acini with that respective K-level

As shown in Table 4.1, conducting a paired t-test with a Bonferroni correction revealed that the degree of narrowing between K2 and K3 was significantly different ($p = 0.0006$, $\alpha^* = 0.01$), as was K4 to K5 ($p = 0.0099$, $\alpha^* = 0.01$) using the unrestricted optimization process described above.

Table 4.1. Statistical difference between degree of narrowing in neighbouring K-levels.

Comparison	p-value ($\alpha^* = 0.01$)
K1 to K2	0.16
K2 to K3	0.0006
K3 to K4	0.013
K4 to K5	0.0099

- with removal of subjects with 0% of airways within K5 level

When simulated annealing is turned, the system converges to an optimal solution as is depicted in Figure 4.5 where (A) shows the convergence to an optimal graded narrowing scheme for simulating ventilation in a single subject with V2 of simulated annealing, and (B) shows an optimization schedule for a single (different) subject with V3 of simulated annealing, where the first phase (iterations 1-500) optimized a graded narrowing scheme for the non-terminal airways by minimizing SSD between simulated ventilation and subject ventilation, and the second phase (iterations 501-1000) optimized a graded narrowing scheme for terminal airways to achieve the same goal mentioned above. The same cooling rate, and number of iterations was used for both applications.

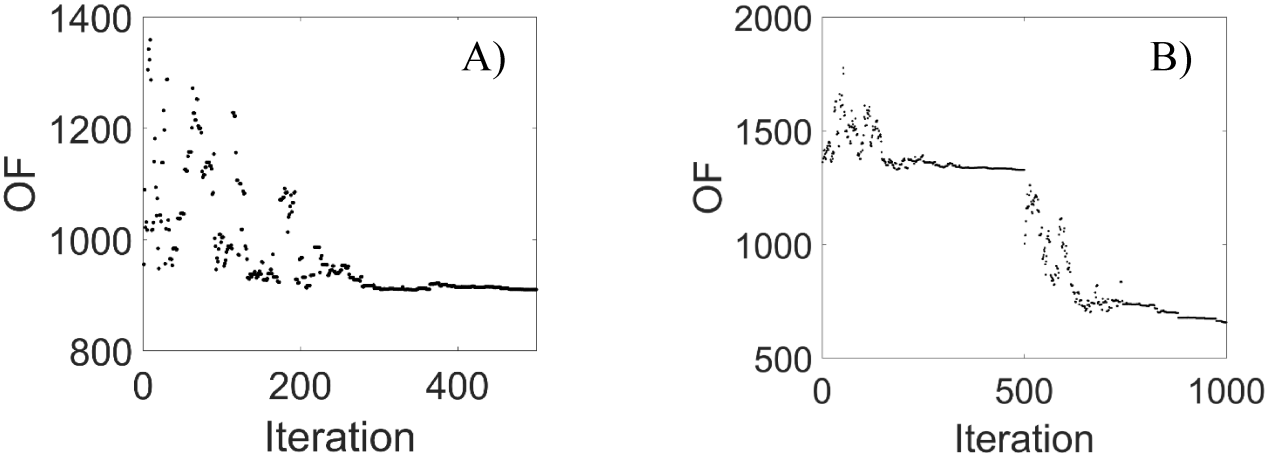

Figure 4.5 The minimization of the objective function (the sum of squared differences between simulated and real ventilation images) for a single application of simulated annealing to the terminal airways (A), and a dual application, first to the conducting airways, then the terminal airways (B).

On a subject specific basis, repeated applications of simulated annealing (V3) appeared to produce solutions (OFs') that had a ~10% variability. The OF of repeated simulations (N = 5) for the eight subjects are shown in Figure 4.6.A. Interestingly, the largest error bars (standard deviation) corresponds with subjects that had worse registration statistics (refer to Figure 4.1). Figure 4.6.B demonstrates the fractional diameter relative to initial diameter of the averaged graded narrowing scheme (height of bars) applied to conducting airways, where the error bars are representative of the standard deviations from N = 5 repeated measurements. Intra-subject variability (degree of narrowing between neighbouring K-levels) appeared to be less than what was found for the terminal airways shown in Figure 4.6.C. Intra-subject variability might suggest that the topography of the optimization landscape near the global minima is flat, meaning that there are numerous solutions that produce similar simulated ventilation. Further discussion of this can be found in section 5.2, pages 83-4.

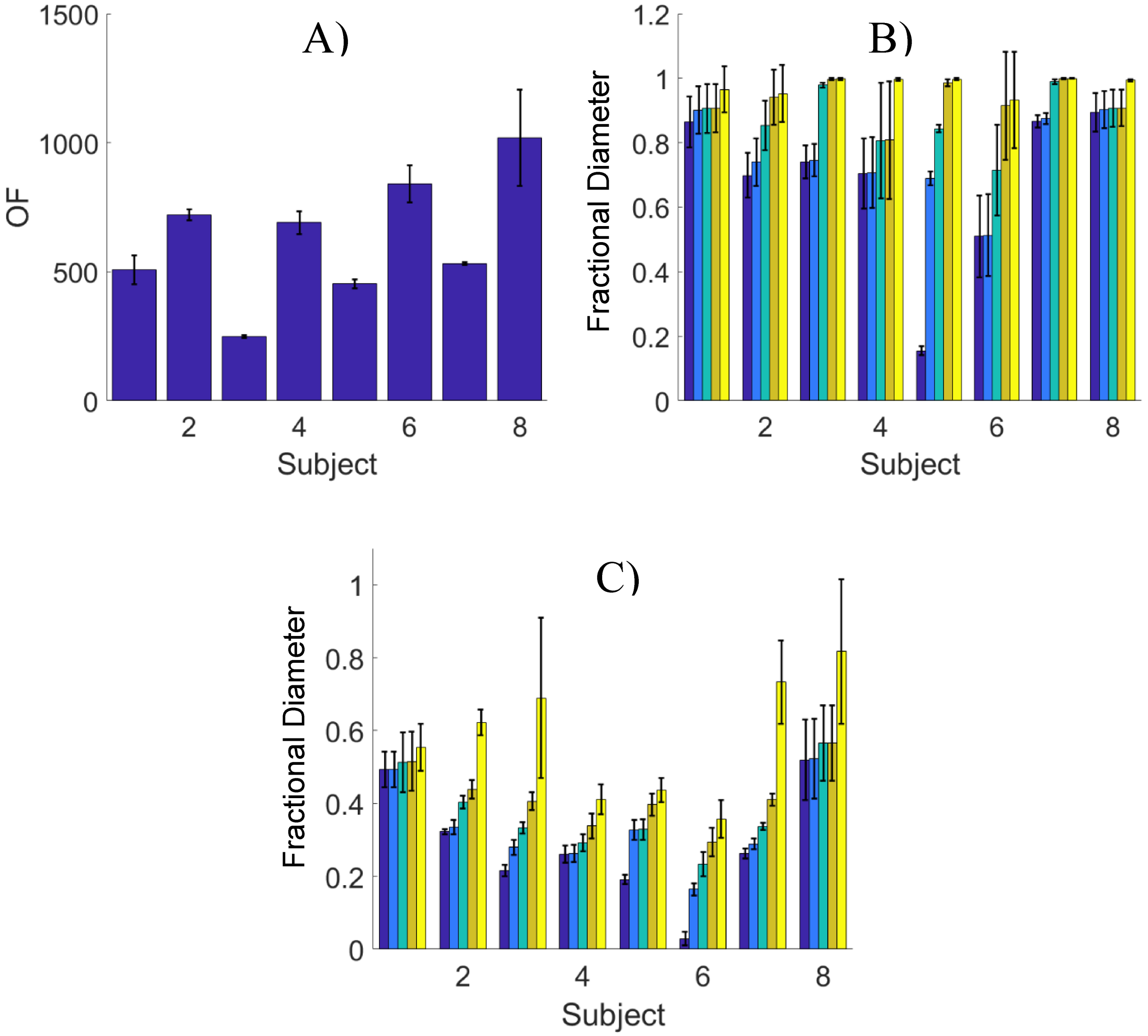

Figure 4.6. Repeated application of simulated annealing (n=5) on all subjects. Values are the means and error bars are the standard deviations. (A) A plot of the minimized OF found from simulated annealing. (B) The constriction levels of the conducting airways for each subject, where the bars are representative of K-levels 1-5 (left to right in each group). (C) Same as in B, but for constriction of the terminal airways.

The solutions found from the three different versions of simulated annealing (the average fractional diameter across all K-levels) for the terminal airways is shown in Figure 4.7. There was a decreasing fractional diameter with decreasing K-level, as was observed before with an unrestricted optimization (Figure 4.4). The variation of the fractional diameter across all subjects for a given K-level, was smallest with V1 of simulated annealing. Interestingly, the extent of narrowing required for terminal airways was largest with V3, despite additional narrowing being applied to the conducting airways as shown in Figure 4.8. Also, the degree of narrowing applied to the conducting airways (Figure 4.8) appeared to be asymptotic with K-level.

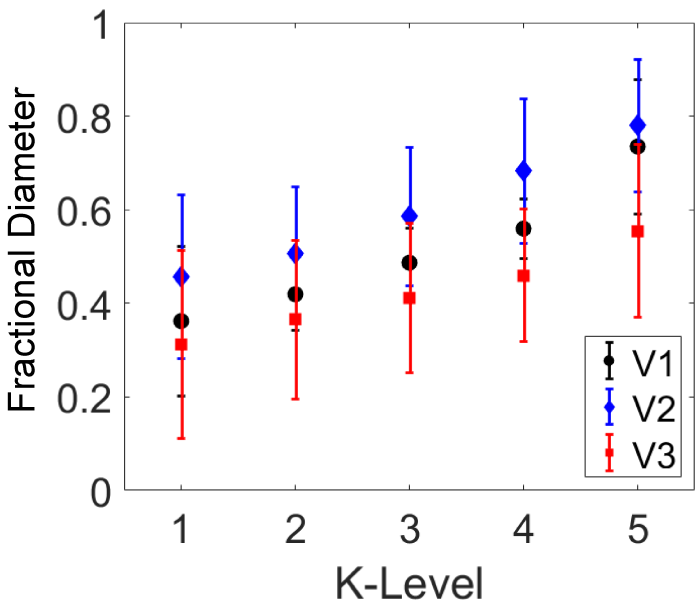

Figure 4.7. Average degree of constriction applied to the terminal airways for the eight subjects as function of K-level. Errors bars indicate the standard deviation of a given constriction level across all subjects.

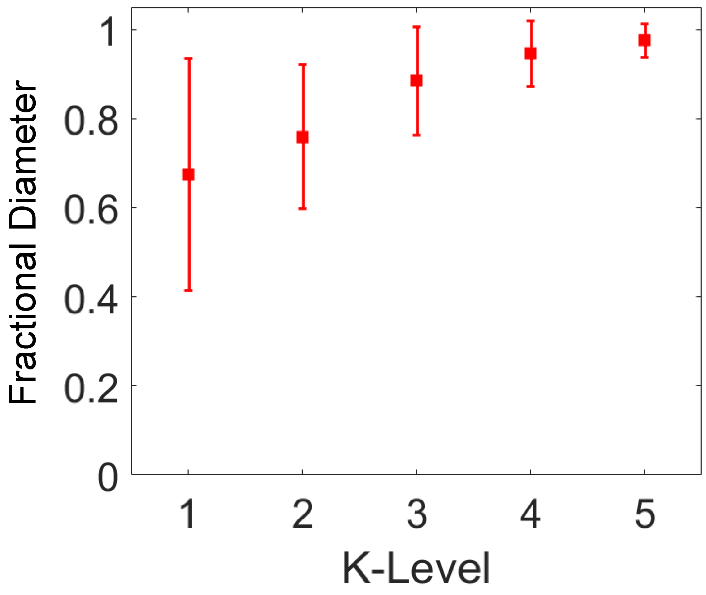

Figure 4.8. Average degree of constriction applied to the conducting airways for the eight subjects as function of K-level for version 3. Errors bars indicate the standard deviation of a given constriction level across all subjects.

For V2, the degree of narrowing and the percentage of terminal airways found within a given K-level is depicted in Figure 4.9, where the height of the bars reflects the degree of narrowing as fractional diameter, and the width of the bars reflects the percentage of terminal airways that fell within the respective K-level (normalized to 100% for each subject). We found that the degree of narrowing for a given K-level between subjects was highly variable, e.g, the height of the bars in Figure 4.9 for K1 between subject #1 and #6 was substantially different. Interestingly, the percentage of airways (width of bars in Figure 4.9) within K-levels did not seem to have an impact on the inter-subject variability of narrowing (height of the bars in Figure 4.9), as the K3 level had the widest bars on average but had similar variability to other K-levels. Excluding the K5 ventilation level (due to 3 subjects having 0% of the terminal airways within this ventilation level), the largest range of constriction was seen in the K1 (defect) level.

Additionally, across all versions of simulated annealing, the degree or narrowing in the K1 level was largest for subject #6, and lowest for subject #8.

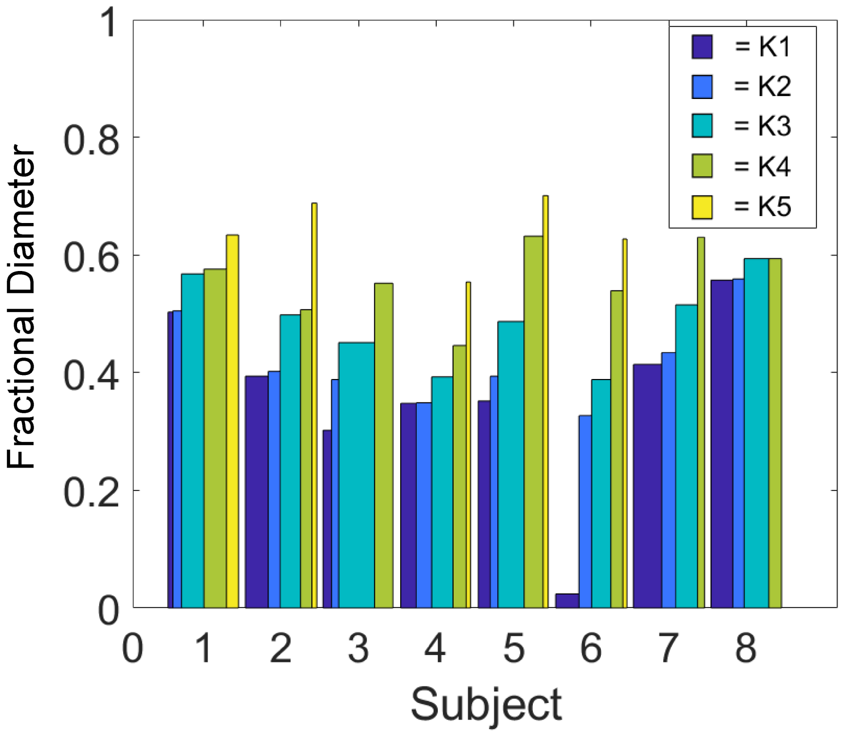

Figure 4.9. The fractional diameter of airways that fall within a given ventilation level (K-level) after simulated annealing for all eight subjects. The width of the bars represents the percentage of terminal airways that fall within a respective K-level.

4.3 Simulated Ventilation

Recall that the objective of simulated annealing was to perturb the graded-narrowing scheme on subject-specific basis to reproduce the ventilation pattern in an inhaled gas MR image. As shown in Figure 4.10, five of the eight subjects showed improved image matching (lowest OF across models) with V3 of the graded narrowing model with simulated annealing. Results from V1 and V2 were plotted as one data point as the OF only varied by 1% between each version. Simulated ventilation images with V1/V2 were significantly improved compared with binary-defect modelling as evaluated by a paired t-test with a Bonferroni correction ($p = 0.005$, $\alpha^* = 0.017$), as was V3 ($p = 0.004$, $\alpha^* = 0.017$). However, there was not a significant difference in simulated ventilation (OF) between V1/V2 and V3 ($p = 0.39$, $\alpha^* = 0.017$).

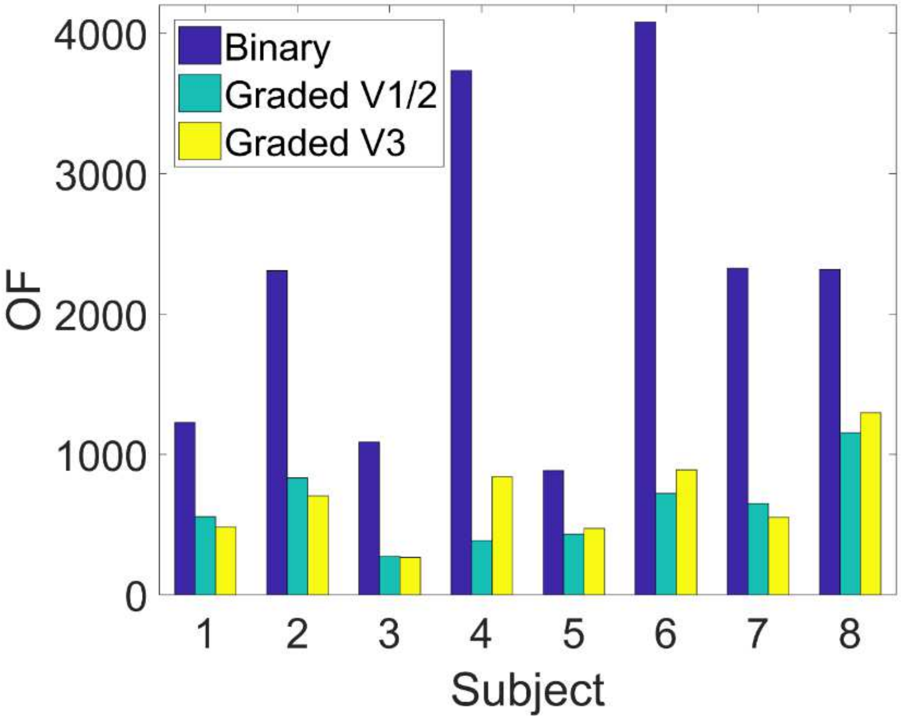

Figure 4.10 The objective function for binary modelling, and the three different versions of simulated annealing. Version 1 and 2 were represented as one bar (V1/2) as their values were within 1% of each other.

Compared with the binary closure model, the graded narrowing model was able to produce ventilation images that were visually closer to measured ventilation in terms of defect size, as well as degree of ventilation within hyperventilated regions; albeit, the binary closure model was able to produce a ventilation intensity within defect regions that more closely resembled subjects' measurements. An example of this finding is shown in Figure 4.11, where the degree of ventilation within a defect region (highlighted by a red circle) from the subject (right), bears a closer resemblance with simulated ventilation of the binary model (left), compared with the graded narrowing model (middle).

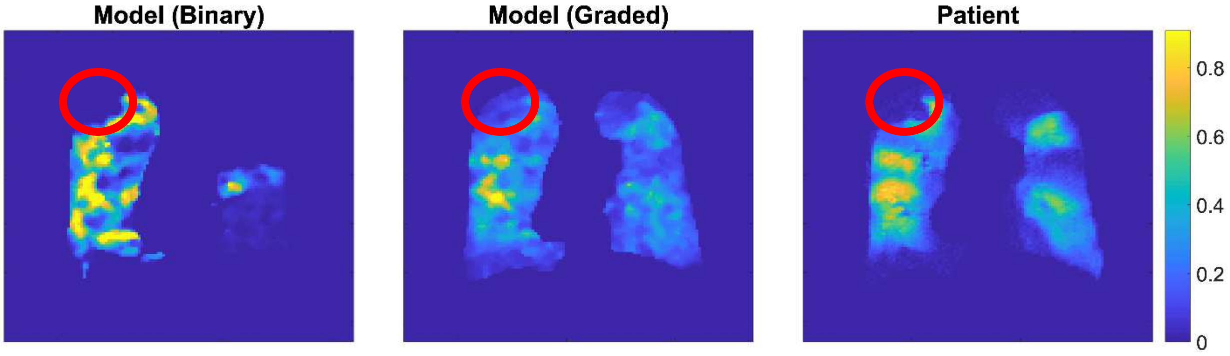

Figure 4.11 Simulated ventilation images of subject #2 for binary model (left), graded narrowing model (middle), and MR ventilation image (right). Red circles highlight the degree of ventilation with defect regions.

Additionally, we observed that a higher of heterogeneity present in the subjects' ventilation image (evaluated qualitatively) typically resulted in simulated annealing producing ventilation images that were qualitatively closer matched with the subjects' MR images. An example of one such subject with a high degree heterogeneity is shown in Figure 4.12. The graded narrowing model (middle) produced a ventilation image that was very similar to subjects' ventilation (right), whereas the binary model (left) did not.

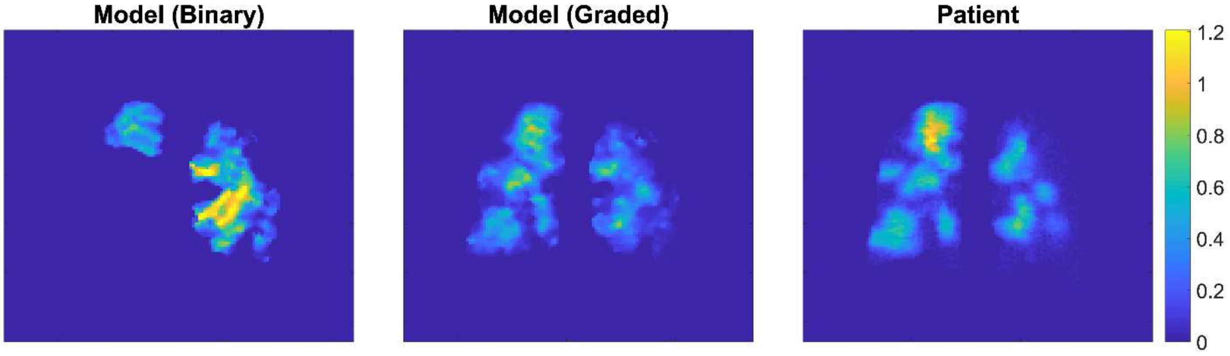

Figure 4.12. Simulated ventilation images of subject #6 for binary model (left), graded narrowing model (middle), and MR ventilation image (right).

Although the graded narrowing scheme was able to produce simulated ventilation images that were quantitatively closer to subjects' measured ventilation (compared with ventilation produced by the binary model); when ventilation was largely homogeneous, the outcomes of simulated annealing was notably limited. An example of a poor simulated ventilation image where the subject exhibited arguable ventilation homogeneity is shown in Figure 4.13; where the graded narrowing model (middle) produced patchy ventilation in regions that were homogeneous in the subjects' measured ventilation (right). But, the graded narrowing model still produced qualitative, and quantitative improvements in ventilation comparatively with the binary model.

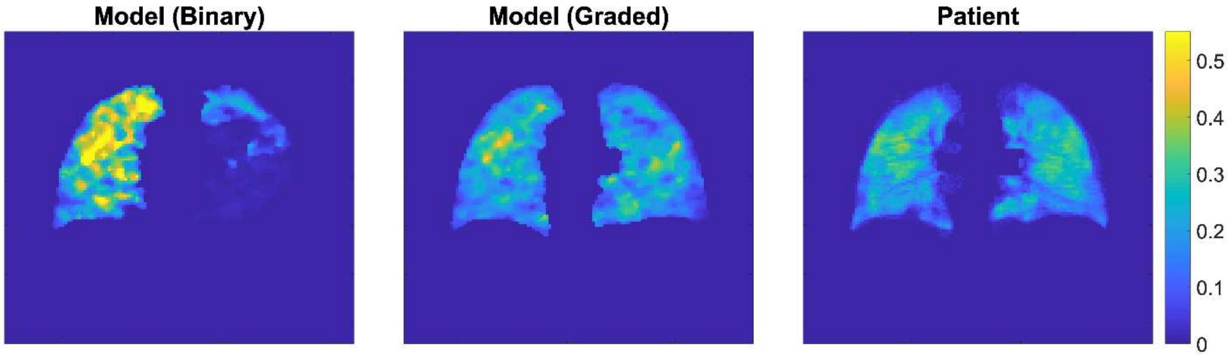

Figure 4.13. Simulated ventilation images of subject #1 for binary model (left), graded narrowing model (middle), and MR ventilation image (right).

From the simulated ventilation image, the cumulative distribution of ventilation was calculated and is shown in Figure 4.14.A, where the horizontal axis describes the fraction of voxels with a specific signal intensity, and the vertical axis describes the cumulative ventilation; e.g, 80% of voxels contained 40% of the total gas signal in the subjects' ventilation. Figure 4.14.B shows the cumulative distribution function for binary closure models (dotted and dashed lines) as done by Campana et al.[118] We found that graded narrowing model was able to produce a cumulative distribution function that more closely resembles that of the subjects' ventilation image across the entire ventilation signal intensity range. In contrast, they found that a 70% closure to defect regions more closely resembled subjects' relative ventilation distribution. But, their 70% binary closure scheme predicted a homogeneous filling of voxels within ventilated regions as was seen in Figure 1.8. This could imply that the binary closure model fails even with added Gaussian variation fails to fully model the ventilation heterogeneity, as we and others observe in asthma.[134-136]

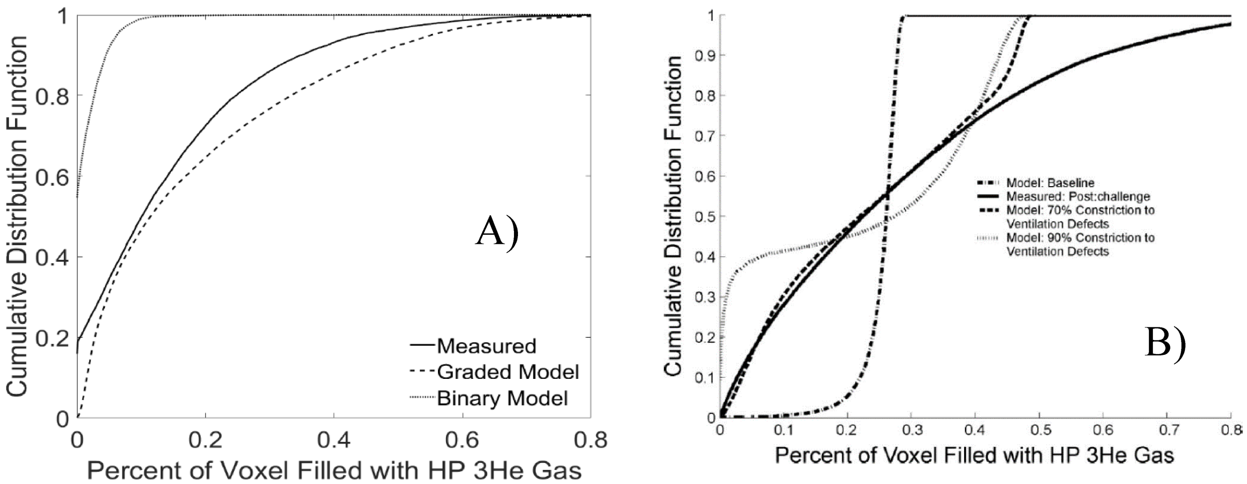

Figure 4.14 (A) Cumulative distribution of ventilation within simulated and real ventilation images. (B) Plot reproduced from Campana et al.,[118] depicting the same information with the

various models tested. As shown for the baseline model (dashed-dotted line), it predicts a homogeneous distribution of ventilation for > 25% of all voxels.

4.4 Modelled Impedance

Manual selection of the free parameters in equation 30 was performed to achieve a baseline resistance that was 50-60% lower than the subjects' measurements.This process could be automated by integrating it into the simulated annealing method, albeit at the expense of computational time. The list of these parameters for each version of simulated annealing is presented in Table 4.2, as well as scaling for the terminal airways (D_{term}), the conducting airways (D_{cond}), and additional stiffness of the lung ($E_{acini,add}$) to match subjectss' measured impedance. We also see that V3 was able to reduce the PI in 6 of 8 subjects, which is a metric used to quantify the degree of matching with subjectss' impedance measurements (lower is better). The subjects that did not show improved PI in V3, exhibited worse matching of $R_{rs,}$ but closer matched X_{rs} to subjects' measurements.

Table 4.2 Scaling parameters for equation 30, and lung elastance, E_{acini}, for baseline conditions. Scaling factor applied to conduction airways, D_{cond}, and terminal airways, D_{term}, as well as added Elastance, $E_{acini,add}$ after the application of simulated annealing.

Subject	α	β	d_p	E_{acini} (cm-H_2O-L^{-1})	D_{cond}	D_{term}	$E_{acini,add}$ (cm-H_2O-L^{-1})	PI (cm-H_2O-s-L^{-1})
1	1.3	1	2.14	11.3	-	1.066	-	2.59
	1.36[†]	1.145[†]	2.14[†]	12[†]	-	1.151[†]	-	2.63
	1.608[††]	0.89[††]	2[††]	20.6[††]	0.875[††]	1.2[††]	0[††]	2.32
2	1.3	1	1.888	8.6	-	1.063	-	6.12
	1.432[†]	1.1[†]	1.888[†]	8.9[†]	-	0.96[†]	-	6.27
	1.686[††]	0.81[††]	2[††]	15[††]	0.988[††]	0.9[††]	104[††]	3.42
3	1.3	1	2.48	14.1	-	1.43	-	0.64
	1.272[†]	1.2[†]	2.48[†]	14.6[†]	-	1.53[†]	-	0.67
	1.41[††]	0.85[††]	2[††]	30.3[††]	1.15[††]	1.12[††]	0[††]	0.63
4	1.3	1	2.28	15.9	-	1.3	-	1.32
	1.265[†]	1.1[†]	2.28[†]	16.8[†]	-	1.216[†]	-	1.23
	1.218[††]	0.79[††]	2[††]	26.8[††]	1.26[††]	1[††]	0[††]	1.64
5	1.9	1	4.16	13.1	-	1.23	-	3.77
	1.852[†]	1.7[†]	4.16[†]	8.6[†]	-	1.245[†]	-	3.52
	1.615[††]	0.9[††]	2[†]	33.8[††]	1.14[††]	0.8[††]	0[††]	3.70
6	2	1	4.72	15.3	-	1.61	-	5.77
	1.8[†]	1.722[†]	4.72[†]	10.3[†]	-	1.585[†]	-	5.47
	1.601[††]	0.85[††]	2[††]	43.1[††]	1.7[††]	1.2[††]	47[†]	3.30
7	2	1	4.705	15.6	-	1.22	-	7.46
	1.75[†]	1.689[†]	4.705[†]	10.8[†]	-	1.061[†]	-	7.03
	1.449[††]	0.87[††]	2[††]	42.2[††]	0.93[††]	1.02[††]	90[††]	5.13
8	1.3	1	2.266	14.0	-	0.917	-	7.05
	1.275[†]	1.1[†]	2.266[†]	16.0[†]	-	0.766[†]	-	7.71
	1.38[††]	0.85[††]	2[††]	25.8[††]	0.56[††]	0.7[††]	110[††]	6.11

[†] Second version of simulated annealing

[††] Third version with two levels of simulated annealing

4.4.1 Comparison of Binary Constriction to Graded Scheme

For all subjects, the graded narrowing scheme was able to produce larger changes in resistance from baseline predictions compared with binary defect modelling ($p = 0.0003$, $p = 0.0002$, $p = 0.0003$, $\alpha^* = 0.017$, for V1, V2, and V3 respectively). There was not a significant difference between each version of graded narrowing model at the confidence level, $\alpha = 0.05$, for the calculation of R_5 [$F(2,21) = 0.000341$, $p > 0.05$]. Figure 4.15.A shows the baseline R_5 prediction, the binary model R_5 prediction, the graded narrowing model R_5 prediction (all versions), and the subjects' measured R_5 for all subject; where the predicted R_5 from all versions of the graded narrowing model fell within the standard deviation of subjects' FOT measurements. Similar information is presented in Figure 4.15.B, but for X_5 predictions. The X_5 prediction from the graded narrowing model was not statistically different than binary defect modelling ($p = 0.1$, $p = 0.17$, $p = 0.028$, $\alpha^* = 0.017$, for V1, V2, and V3 respectively), but within a larger sample size, V3 shows promise of improvement. Using single factor ANOVA with a Bonferroni correction, there was a significant difference between the predictions of X_5 different versions of graded narrowing modelling [$F(2,21) = 6.3535$, $p < 0.01$]. Using a Tukeys' Honest Significant Difference test, we found a significant difference between V1 and V3 ($2.17 > 1.43$), as well as V2 and V3 ($2.09 > 1.43$). Also, V3 of the graded narrowing model was able to predict an X_5 that was within the standard deviations of subjects' measurements for 6 out of 8 subjects. Compared with binary defect modelling, all versions of the graded narrowing model were able to produce significantly larger $R_{5\text{-}20}$ ($p = 0.0012$, $p = 0.0012$, $p = 0.0017$, $\alpha^* = 0.017$, for V1, V2, and V3 respectively). There was not a significant difference in the predicted $R_{5\text{-}20}$ between the different versions of the graded narrowing model [$F(2,21) = 0.004818$, $p > 0.05$]. In Figure 4.15.C, we show the $R_{5\text{-}20}$ for the same models/measurements shown in Figure 4.15.A, and

Figure 4.15.B. In Figure 4.15.C, we can see that only subject #3 and #4 had a predicted $R_{5\text{-}20}$ with the graded narrowing model that was close to the subjects' measured $R_{5\text{-}20}$; all other subjects had predicted values that appeared lower than subjects' measurements. A single factor ANOVA test revealed that the predicted $R_{5\text{-}20}$ was not significantly different between different versions of the graded narrowing model [$F(2,21) = 0.\ 00403$, $p > 0.05$].

In Figure 4.16 we show the R_{rs} spectra (left), and the X_{rs} (right) for all versions of simulated annealing. Over the full frequency range, V3 of the graded narrowing model predicted an X_{rs} spectra that appeared more closely matched with subjects' measurements, comparatively with the other versions of the graded narrowing model, as well as the binary closure model. An apparent larger frequency dependence in R_{rs} was seen with V3, but this result was unique to subject #2, for other subjects', the improved matching of X_{rs} came at the expense of worse matching of R_{rs} at high frequencies (and similarly worse $R_{5\text{-}20}$). An example of one such subject is shown in Figure 4.17, where we show the R_{rs} and X_{rs} spectra for all three versions of simulated annealing, and worse matching of R_{rs} to subjects' measurements in V3 was evident. Regardless, V3 of the graded narrowing model was able to produce a X_{rs} spectra that apparently closely matched measured FOT in subjects 2,4,5,6,7, and 8.

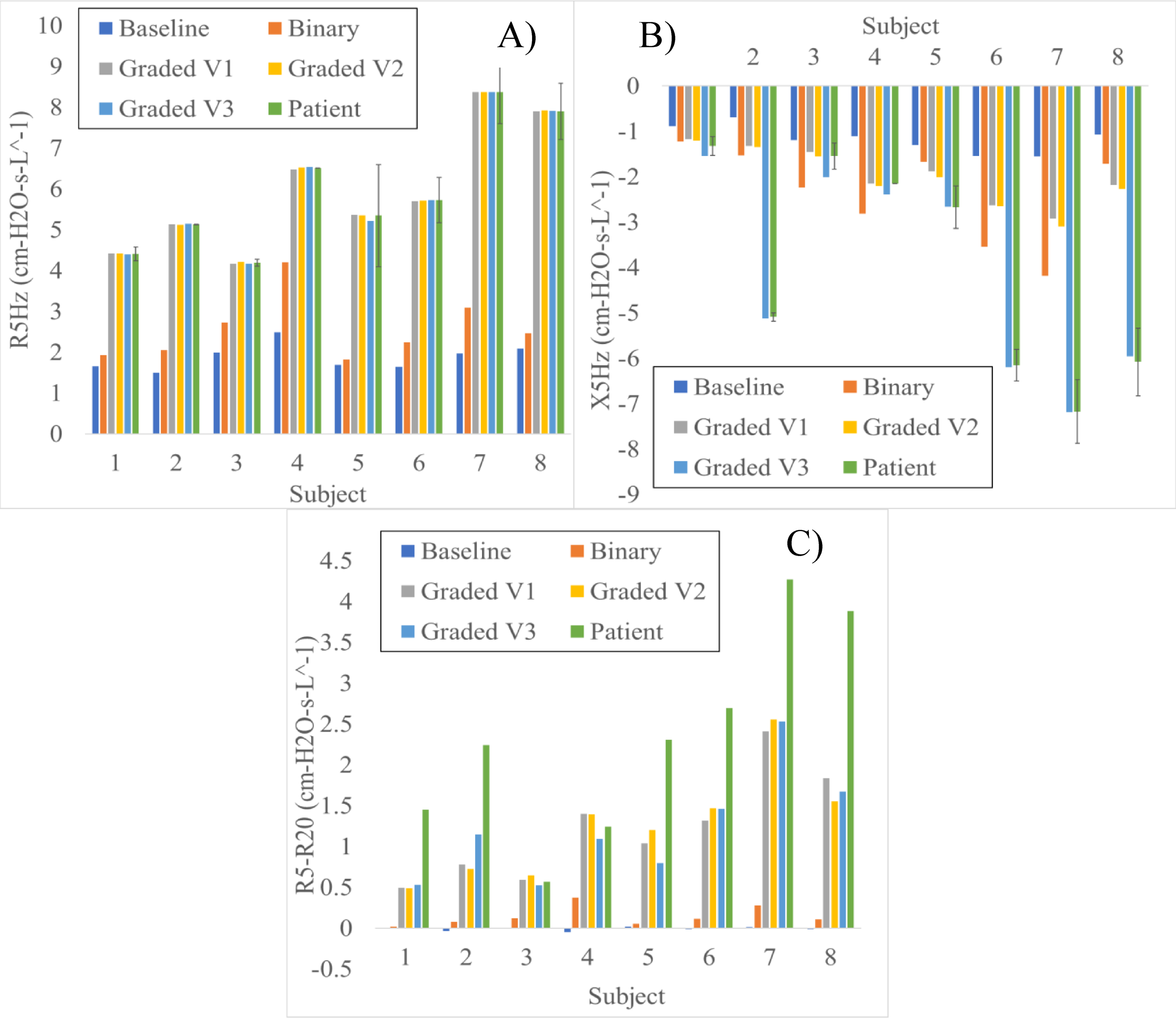

Figure 4.15. (A) Model predictions of R_{5Hz} compared with the subjects' measurements. (B) Model predictions of X_{5Hz} compared with the subjects' measurements. (C) Model predictions of $R_{5\text{-}20}$ compared with subjects' measurements. Errors bars for subject values were based upon the standard deviation from the three consecutive measurements.

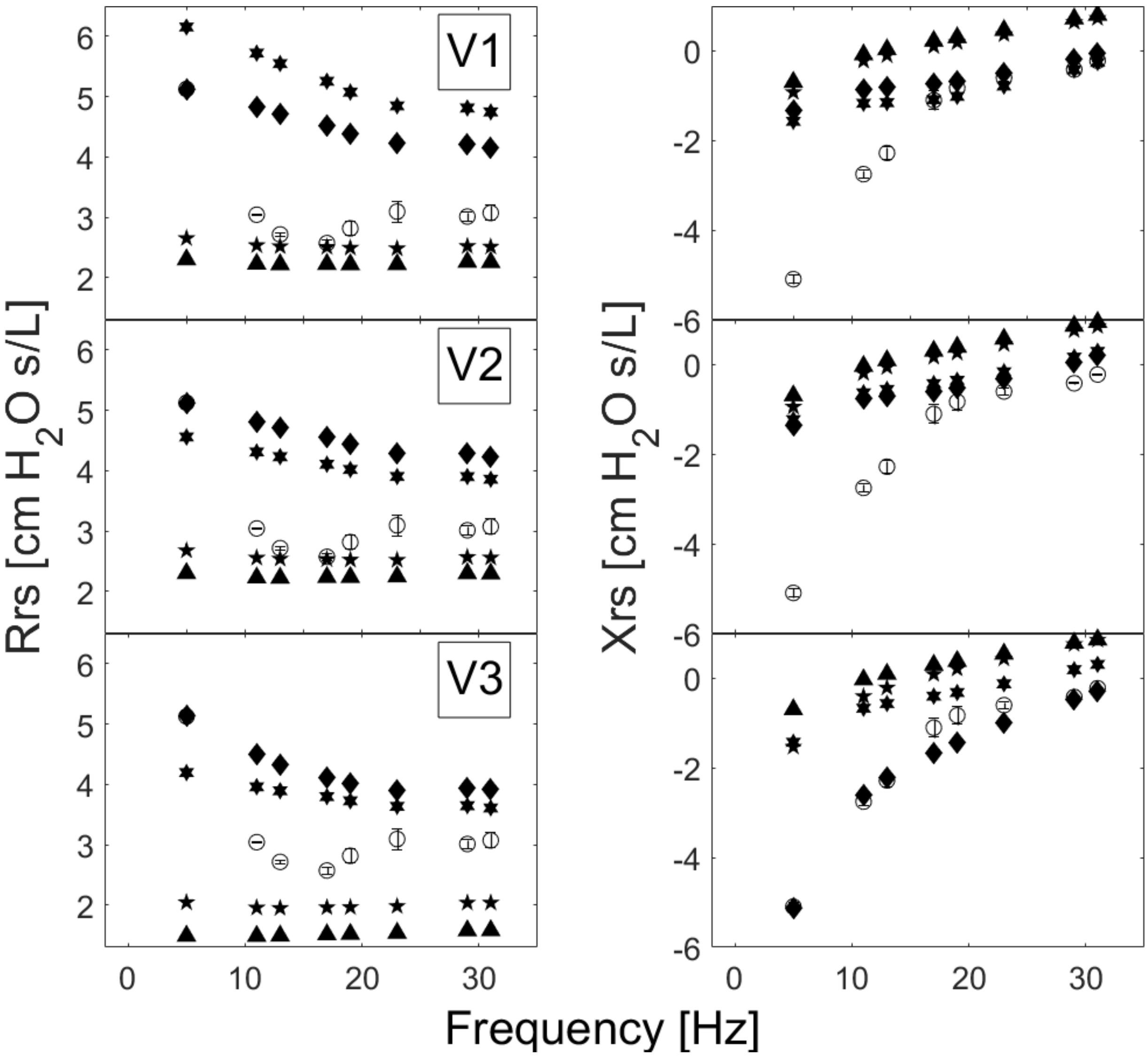

Figure 4.16 A plot of R_{rs} (left), and X_{rs} (right) for subject #2. The rows represent the different version of the graded narrowing model. Triangles represent healthy predictions, stars binary model predictions, hexagrams graded narrowing predictions, diamonds are with scaling, and circles with error bars that are standard deviations from three consecutive subject measurements.

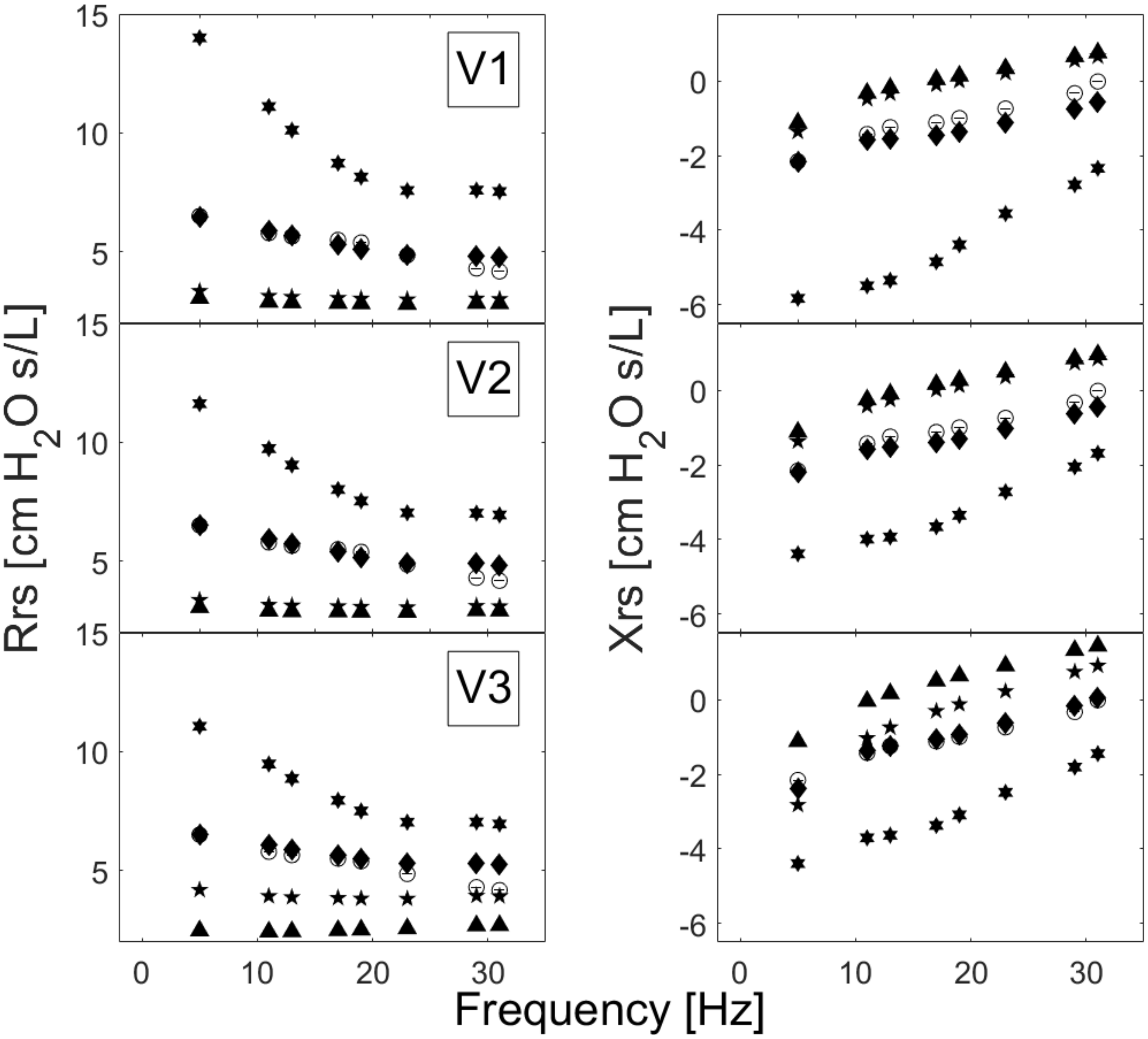

Figure 4.17 A plot of R_{rs} (left), and X_{rs} (right) for subject #4. The rows represent the different version of the graded narrowing model. Triangles represent healthy predictions, stars binary model predictions, hexagrams graded narrowing predictions, diamonds are with scaling, and circles with error bars are the standard deviations from three consecutive subject measurements.

4.5 Time Constant Map

A time constant map, which reflects the time for regions to fill to 63.2% of their maximum volume has the potential to give insight into the applicability of different PFTs or imaging techniques for assessing obstructive airway diseases like asthma. A time constant map for a single inhaled gas MRI slice is shown figure 4.18, where a large distribution of time constants is apparent.The visualization is limited to 32 seconds, which provide even range in time constants to either side of the image acquisition time of 16 seconds. When the time constant map (A) is compared with the subject's original inhaled gas image (B) we can see that an appreciable proportion of the lung is not getting a sufficient flow of air (volume of gas) during the MRI acquisition, and thus appear as ventilation defects. We can also observe that the time constants in regions of high ventilation occur over the timescale of normal breathing (~ 2s per breath).

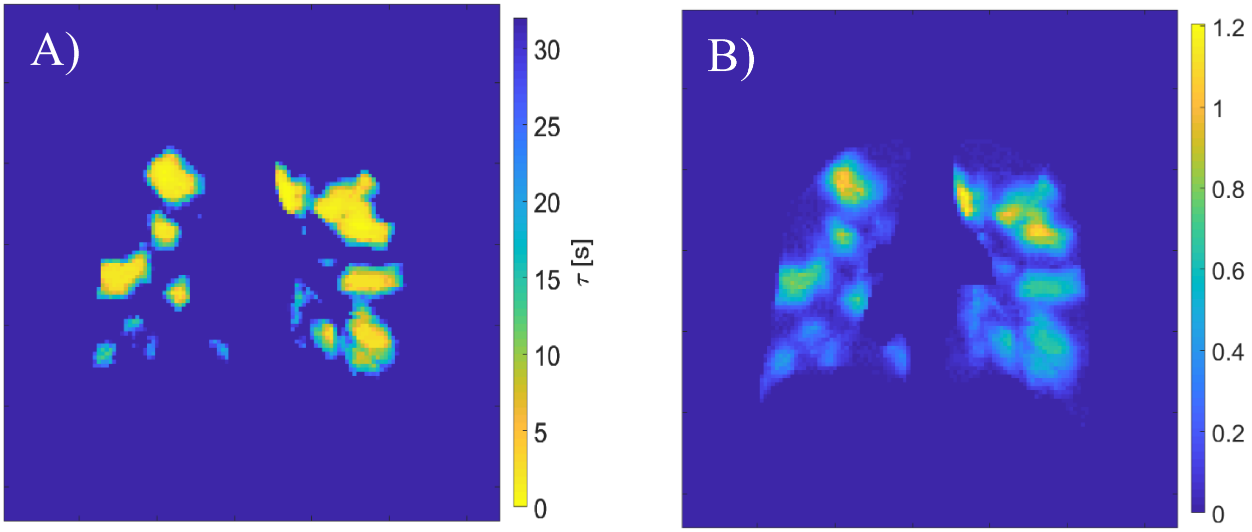

Figure 4.18 For subject #6: (A) Is time constant map to reflect it takes for a given region to be ventilated to 63.2% of its' maximal volume. (B) is the original inhaled gas image from this subject.

Chapter 5. Discussion

The intent of this work was to improve upon previous models of respiratory mechanics in asthma, which used a multi-branching airway tree model with binary closures that were derived from inhaled gas imaging. This modelling paradigm has been used in many studies to predict respiratory impedance;[99-102] but, its' ability to simulate ventilation that matches subjects' measurements is limited. This could have an impact on the interpretation of oscillometry and the nature of heterogeneous airway narrowing in disease. We hypothesized that the remaining information within the inhaled gas MRI, in the form of hypointense to hyperintense signal, could be used to guide a graded narrowing scheme within a multi-branching tree model, and would improve predictions of respiratory impedance and ventilation, when compared with the previous binary closure model.

The following discussion is separated into sections where the **principal findings** will be each discussed in turn. In the first section, the development of a registration framework that deformed the airway tree to fit within the subject-specific MRI lung space will be discussed. Following this, the appropriateness of the optimization framework, which derived an optimal subject-specific graded narrowing scheme (for the airway tree) to match simulated ventilation with subjects' measurements, will be discussed in the context of global optimization. Next, the implications of the graded narrowing scheme on ventilation, impedance predictions, and structural heterogeneity will be discussed at length. Then, a comparison of the findings from this study will be made with findings of Campana et al., who simulated ventilation with a multi-branching airway tree model that had binary closures.[100] Finally, there will be a discussion of the limitations in the modelling approach.

5.1 MIND for Morphing Airway Trees

The MIND algorithm described in section 3.1.3 was created to deformably register intensity-based images from different imaging modalities. Previous results from Heinreich et al.,[109] indicate that the MIND algorithm is superior to other common registration metrics for the same optimization framework by minimization of localization errors for 119 landmarks located in the Visible Human dataset. But, the registration proposed in this thesis did not produce impressive registration statistics (85 ± 4% DSC and 79 ± 4% FVO between tree and MRI) largely driven by poor registration in the periphery, and mis-registration in the medial/lateral long abutting the cardiac notch. There are two main reasons for mis-registration, (1) the smaller airway tree volume necessitated larger deformations which would sometimes create non-realistic airway tree volumes, (2) The algorithm relies on an automated MATLAB function, alphashape, to create an outline of the airway tree in slice-format. Alphashape creates an envelope around a set of 2D or 3D points (like a coronal slice of the MR image) with polygons. However, this function is unable to operate for < 3 points and sometimes has difficulty with a small amount of oddly oriented points. If the envelope of the tree is not indicative of the tree's actual shape, this will increase the burden on the MIND algorithm to implement large deformations. Poor registration dictates the lowest achievable OF, since airways could be missing in regions where ventilation was present, or conversely, airways could be where they should not be. When airways are improperly registered, matching ventilation in individual lobes could potentially require that airways from different lobes or segments to be narrowed, which of course is not a depiction of reality. While ventilation can be well-matched by implementing local narrowing to small airways in the overlapping regions, this likely limits the ability to match subjects' impedance.

Perhaps, extending this approach to a 3D registration has the potential to improve these statistics. The MIND algorithm requires an isotropic voxel size to perform registration, so for 3D MIND, we would require an up-scaling of the resolution in the MRI dataset along the "slice" direction because the original image resolution is ~ 3 x 3 x 14 mm^3. This creates a significant challenge for converting the airway tree into an image-volume (like the MRI dataset). To meet the requirements for isotropic voxel sizes, the 3D-MIND algorithm requires the airway-tree to be divided into 78 slices. Due to the existing algorithm for rigid registration of the tree to the MR volume (before deformation), an application of 3D MIND that was attempted was only able to work for three subjects (#1, #2, #7). For these subjects, we saw an average of a 2% increase in registration (quantified by FVO). For the remaining subjects, the implementation of alphashape on the far-most anterior and posterior slices did not work, causing the algorithm to fail. To preserve the entire tree structure and accommodate the needs of the 3D-MIND algorithm, one approach to help would be to create an in-house software that can draw intelligible polygons for any number of points.

Likely the choice of MIND, or any other intensity/information-based registration algorithm would be inappropriate for this problem type. Given that the registration problem in this thesis is simplified to shape-matching, one being an airway tree, and the other being an MR volume; a mesh-based registration algorithm is likely to be best suited.[119-121] To register the highly complex airway tree structure to the MR image set, landmarks such as branching point locations within the subject's CT-set, lobar boundaries, and parenchymal boundaries should be known to guide registration. This poses significant a challenge as our computational airway tree is only physically accurate down to 8th generation. However, a possible registration framework could look something like: (1) manual identification of large-airway landmarks within CT image set (2) deformable registration of landmarks / CT lung space to MR lung space similar to Guo et al.[122] (3) co-register available landmark fiducials within the tree to MR fiducials (4) Create a mesh out of the MR image set and stretch terminal airways to lobar boundaries.

Nevertheless, the methodology in this thesis was able to improve simulated ventilation (over the binary closure model), and improve impedance predictions in several subjects, but in some, the impedance was only well matched at low frequencies. The registrations were similar across subjects, thus issues in registration may not explain this difference, and possibly had more to do with the possibility that these subjects possessed an airway tree structure that more strongly differed from our tree. Therefore, although accuracy in registration was limited, and could be improved, since both graded and binary approaches shared the same registration, any improvements in registration are not likely to significantly impact the improved performance of graded imaging for modelling asthmatic physiology.

5.2 Simulated Annealing for Optimization

Simulated annealing was able to find an OF that was highly reproducible; but, there were still variations in the OF and thus in the fractional diameters for each K-level in the final solution, implying that the solution space near the final solution was 'bumpy,' with many equally shallow local minima. While one of these could be a global minimum, it appeared not to be too different from other local minima. Also, while the variability in the final graded narrowing scheme had a minor impact on the OF, it surprisingly did have a significant impact on Z_{rs}. Potentially, this is because the ventilation distribution is more sensitive to relative differences in airway diameters, but less sensitive to the overall constriction or scaling of the airways than Z_{rs}, or because of differences in sensitivity to locations in the airway tree vs small and large airways.

A visualization of a possible objective function for our system is depicted in Figure 5.1 where the landscape of the SSD is likely flat in some region with very small dips (that are nearly equally-optimal). If we were to optimize the problem to fit to an OF that also minimized the difference between measured and modelled Z_{rs} as depicted by red line in the Figure 5.1, we might come to a different configuration of airway diameters. The impedance information on its own is is far too limited to identify model properties in any airway tree model with more than 1 or 2 single compartments (the lung modelled as one or two airways with one or two elastic airspaces). But, the predicted impedance was sensitive to the final OF, indicating that we might be able to differentiate between nearly-equal ventilation solutions by considering an optimization of the airway tree configuration to match impedance measurements. In other words, the inclusion of Z_{rs} optimization could be helpful for deriving an accurate depiction asthmatic physiology as a whole.

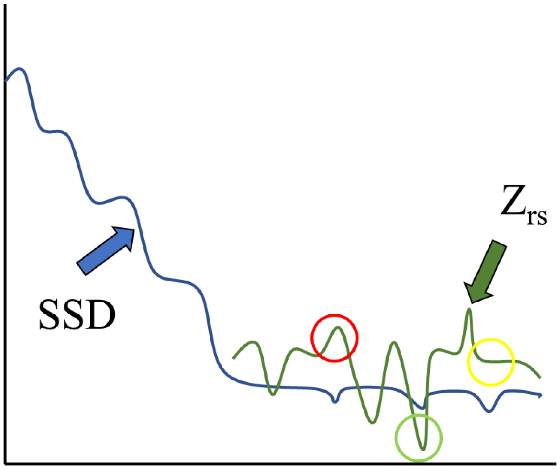

Figure 5.2 Two potential objective functions, (SSD between simulated and ventilation images in blue, and impedance in green) and the circles represent a poor overall optimization (red), a sub-optimal solution (yellow), and an optimal solution (green).

We did employ some scaling of the final fractional diameters in four subjects to predict impedance that was closer matched with subjects' measurements, but, using Z_{rs} within the OF as in Figure 5.2 may have greater flexibility, and be more equipped to find a more optimal OF. In any case while this could improve the OF in both binary and graded schemes, it's unlikely to improve the binary to the level of the graded scheme since the information in the ventilated regions is not used in the binary modelling.

5.3 Outcomes of Graded Narrowing

The graded narrowing model was able to improve over the binary closure model by producing ventilation images that were closer matched with subjects' measurements. However, the binary model predicted ventilation with defect regions that was closer matched with subjects' measurements compared to the graded narrowing model. The binary closure model significantly limits the flow of air to these regions by narrowing airways by 90% (effectively increasing the Poiseuille resistance by 10^4) while the graded scheme chose an optimal fractional narrowing for this level together with all levels. Also, beyond simulating ventilation defects, the binary closure model struggled to produce hypointense signals (equivalent to K2-K3 ventilation level); whereas the graded narrowing model did not. Only one graded narrowing scheme was derived (for subject #6) that was able to simulate well-matched ventilation in defect regions, and hypo to hyper intense signals elsewhere. This subject had a graded narrowing scheme for the terminal airways of fractional diameters of [0.04,0.16,0.23,0.29,0.34], which correspond to the K-levels in the initial graded ventilation image [K1, K2, K3, K4, K5]. The first level of airway narrowing found from optimization was 4% relative diameter (i,e 96% closure) in this subject, which is greater than the 90% that was required for the K1 level in the binary model. But, in other subjects the requirement was less than 90%. Thus, it appeared that 90% closures on their own, particularly in binary threshold-ed images was too limiting, which was observed in previous modelling literature.[99-100]

5.3.1 Optimal Graded Narrowing Schemes

V3 of the graded narrowing model demonstrated the largest improvements in impedance predictions (mainly X_{rs} predictions) compared with the binary model, therefore, this section will only focus on the optimal graded narrowing scheme found with this version. Using a paired t-test with a Bonferroni correction, only the difference in airway narrowing from K2 to K3, and K3 to K4 was found to be significant ($p = 0.0005$, $p = 0.005$, $\alpha^* = 0.01$ for K2 to K3, and K3 to K4 respectively). These findings may suggest that the delineation of five levels for describing heterogeneity might be unnecessary for describing the functional behaviour of the airway tree during ventilation, when using k-means clustered ventilation to guide the narrowing. However, in a study with more subjects, perhaps also K1 to K2 and K4 to K5 may also b significantly different. Also, in any given subject, more thresholds may be important to capture the detail in gradation of ventilation. Indeed, it is possible that an optimization of airway diameters could work without any discretization of the ventilation, using the raw images alone, but this would be computationally expensive.

5.3.2 Impedance Accuracy

In the first modelling paradigm tested, V1 and V2, subjects #5-7 when calculated from their demographic data had a predicted healthy baseline resistance at high frequencies that was larger than the subjects' measurements (in disease). To accommodate this, we imposed that the baseline healthy lung resistance should be 50-60% lower than the high frequency R_{rs} between healthy subjects and subjects with severe asthma as observed by Calvacanti et al.[94] The purpose of these changes was to give the graded narrowing model the opportunity to narrow airways while not overestimating the R_{rs} of the subject. However, predicted R_{rs} was still overshot in half of the subjects. Also, all subjects benefited from a final uniform dilation or constriction factor for the conducting airways (the airways not adjusted using simulated annealing in V1 and V2, but were adjusted in V3), and a separate uniform dilation or constriction factor for the terminal airways to best match impedance measurements through qualitative assessment. The largest reason for final scaling is likely because the starting morphology of the airway tree was not that of the individual subjects'. Additionally, airway lengths were altered during the registration, which would impact the contribution of the inertance to high frequency X_{rs},[123] perhaps explaining in part why the graded scheme high-frequency X_{rs} tended to be over-estimated. Using a subject-specific tree obtained at the same volume as MRI would eliminate the need for such large deformations, reducing the need to optimize registration in 3D, and may provide improved estimates of both ventilation and impedance. Here it was likely that matching impedance while matching ventilation could only be approached but not achieved, due to the differences in airway tree structure and additional differences caused by scaling the lungs from one shape to another.

5.4 Comparison to Campana et al[100]

Campana et al., used a binary closure scheme for defect airways, and added random closures throughout upper airways to model ventilation distribution and impedance in asthma.[100] Similar to our findings, they found that predicted ventilation was much too-low such that their images appeared dimmer than the subject's data. The deviation from the subject's data likely means that there is a scaling factor that is needed within Campana's technique to get values closer to the real ventilation image, but it may be more complex that this, since neither the binary approach or binary with added random variation have guidance to match ventilation in the non-defect regions. Also, Campana and colleagues performed a more complex treatment of closures to airways (like the binary model in this thesis) by only closing the largest airways that would decrease regional ventilation that best matched any given defect, as opposed to applying closures at the site of ventilation. This treatment could very well predict ventilation and impedance that more closely resembles subjects' measurements; however, given that simulating ventilation was our dependent variable for optimization, local closures would be more appropriate.

Like the findings of Campana and colleagues, we found it necessary to include heterogeneity in the larger airways (all airways larger than terminal airways) for proper modelling of airways mechanics. However, we used a graded narrowing scheme derived from the K-levels (ventilation levels) within our MR image to simulate upper airway heterogeneity; whereas Campana and colleagues used a Gaussian distribution of closures to a set range of airway generations with the intent of minimizing the differences with subjects' measurements (minimizing PI). While this improved their impedance estimates, it was at the expense of adding variation to the ventilated regions that did not match subject images. A difference between our model and that of Campana et al. is that they only used their model to predict Z_{rs} up to 8 Hz and without knowing the high-frequency predictions from their model, we cannot be certain if their model would predict the same higher frequency deviations in R_{rs} that we found. Given that they only model Z_{rs} at frequencies lower than what was modelled in this thesis, we can only make qualitative comparisons in which we see that their R_{rs} spectra has an inverse frequency dependence that had close resemblance with subject measurements. While this can arise form heterogeneity that was central to our, and their findings, they also employed the constant phase model for their terminal airways. The constant phase model has a built-in inverse frequency dependence, so this could have contributed to the frequency dependence they observed. As described in section 1.7.2 the healthy frequency dependence attributed to the tissue compartment of healthy humans is appropriate to describe the very low frequency range and is not usually thought to describe the frequency dependence in the FOT range > 4 Hz. However, we used a single-compartment model for the terminal airways, which, while it was able to predict some of the observed frequency dependence, it was less than observed in our subjects. Perhaps the combination of constant phase behavior and heterogeneity could improve the predicted frequency dependence. Another difference is that they modelled flow as laminar, whereas we modelled the flow with the Womersley model which is theoretically superior to model transitional (near turbulent) flow typical for the upper airway and some central airway mechanics.[78.79.101.102] This likely only affects higher frequency behavior and the reactance where inertive effects begin to become prominent, while their results were confined to 8 Hz and below, so any difference with our results is likely modest.

5.5 Model Limitations

Here the main limitations of the approach in this thesis are listed and discussed following: (1) A single tree was used for all subjects as opposed to using subject-specific trees. (2) We assumed ventilation for the acinus was entirely determined from the simple single compartment model (3) and we assumed each acinus was the same size. (4) W assumed each acinus was described by the same compliance at the end of each terminal airway, and airway compliance was negligible. (5) We used an airway tree and acquired MRI ventilation that was obtained in the supine position but measured subject impedance upright.

(1) We used a single airway tree that was registered to the ventilation images of each subject and used it to compute impedance of each subject, while the location of defects and different k-means levels of ventilation were used to guide airway narrowing were obtained from the registration of the tree to each individual subject. The poor registration likely limited the ability to match ventilation and impedance as discussed in detail in section 5.1.

(2) We prescribed the ventilation behaviour of the acinus to be entirely determined from the simple model of a terminal resistance and fixed compliance. However, the shape of the terminal airway and how it merges with the acinus can affect its ventilation. Kumer et al., has shown that the complexity of the respiratory bronchiole with variations of abutting alveoli can lead to variable degrees of entrainment (gas-trapping), that can affect the degree of recirculation and redistribution of gas which we largely ignored.[124] These effects are accounted for in our model only insofar as they can be described by changes in airway diameter coupled with the acinar compliance, However, this simplification may provide sufficient detail for the purposes of describing overall ventilation distribution at the scale of the lung.

(3) Additionally, we assumed that every acinus was the same size (one voxel, 3.125 mm). However, the size of an acinus has been reported to be 5-10 mm long,[125]which would correspond to 2-3 voxels in our simulated ventilation image. This merely means the image resolution was higher than that of the branching tree. To bridge these resolutions, we prescribed the ventilation at the end of each terminal airway from the branching tree to the nearest voxel and spatially averaged the intensity to neighbouring voxels. These gas distribution effects at the acinar levels are the limits of the scale of our imaging resolution. However, we used a flow-divider approach to determine the ventilation pattern, which assumes filling uniquely from the trachea to the acini, and we have ignored the longer range interbranch effects such as pendelluft, whereby gas can redistribute up to 13% of the input flow at bifurcations near defects.[126] This may mean that the airway diameters are predicted to be slightly larger for regions with larger time constants that received some ventilation due to pendelluft after the initial inhalation, and possibly diameters are predicted to be smaller for regions from regions with smaller time constants which donate gas after the initial inhalation during the breath-hold.

(4) We used identical elastances for all terminal acini, and rigid airways (no airway compliance), which can affect flow distribution; instead we relied on airway asymmetry (heterogeneous airway resistance) to dictate flow. This is in contrast with Alder et al., who suggested tissue stiffness is likely heterogeneous[98] and Swan et al.,[127] who found evidence to suggest that a gravitationally-dependent tissue density, and iso-gravitational heterogeneity is needed to best simulate ventilation, albeit in a healthy lung. There would likely be some variation in elastance amongst acini (independent of gravitational effects) from changes in tissue properties and differences in acinar volume; but this was largely ignored because asthma is larger thought to induce heterogeneity arising from airway diameter variation, Furthermore, implementing a compliance distribution would require a complex treatment of Z_{rs} to distribute airflow as in Coletti et al.,[118] as opposed to the straightforward used of pathway resistance that was used in this thesis. However, the differences in compliances amongst acini are likely small compared to the effects from airway narrowing, which is well established to be the source of heterogeneity in ventilation in asthma.

(5) We used an airway tree and acquired MRI ventilation that was obtained in the supine position but measured subject impedance upright. In the supine position the abdominal contents move upwards and this decreases lung volume narrowing airways, increasing $R_{rs,}$ and also can cause more negative X_{rs} if airways become sufficiently narrowed. The chest wall may also change its contribution to X_{rs} when supine particularly in obese subjects. Peters and colleagues have recently performed measurement of oscillometry in upright, and supine position for severely obese subjects before and after undergoing bariatric surgery.[95] In these subjects the supine position increased R_{rs} approximately 15 % and X_{rs} by approximately 100%. The changes due to supine position in our study should be less than this since our subjects were not severely obese. Also,

these differences would still not be sufficient to account for the disparity that was described in section 1.8 in the percent change in X_{rs} from healthy to mechanics in asthma and the percent change in ventilation defects that exists similarly comparing healthy to asthma.

Chapter 6. Conclusion and Future Work

6.1 Conclusions

The use of inhaled hyperpolarized gas MR images has been used in the past to guide airway closures within multi-branching airway tree models to model defects and its affects on respiratory mechanical impedance in health and disease. Closures were applied to airways within the defect regions of the tree, while airways outside the defects remained open with random narrowing being applied. While this binary closure paradigm can produce ventilation defects in simulated ventilation images, it is unable to properly model hyperintense ventilation, as well as respiratory mechanics without the need for additional closures throughout the tree which in previous modelling approaches were not guided from the imaging data.[100] In this thesis, a graded narrowing scheme was developed, where the ventilation information within the original inhaled gas image was used to guide the degree of narrowing within multi-branching airway tree. Ventilation images were created from a tree narrowed by a graded narrowing scheme and were shown to be closer to subjects' measurements than a binary closure model ($p < 0.005$) in an eight-subject study. However, the binary closure model did predict ventilation within defect regions that was closer to subjects' measurements (refer to section 4.3). Furthermore, while improved there remained clear discrepancies between the simulated ventilation images of the graded narrowing model and measured ventilation images as well as the size or location of regional ventilation. The differences are possibly in part due due to errors in airway tree registration with the subjects' MR lung space, as well as the fact that the tree itself was not subject specific, which contributed to limiting accuracy in registration, and which could lead to airways being in impossible locations (crossing lobar boundaries, etc.) which likely limited the achievable accuracy or the modelled ventilation.

As described previously, we did not add random, Gaussian distributed closures to the non-defect airways, which had been employed in previous studies to well match subjects' impedance.[99,100] We used a guided graded narrowing scheme that more closely matched subjects' ventilation, but this sacrificed our ability to some extent to match subjects' impedance measurements, particularly not providing sufficient frequency dependence of R_{rs}. In our study, we employed a modelling paradigm which was able to introduce airway heterogeneity but constrained by k-means clustered intensities, and simulated ventilation that very closely matched subjects' measurements (in 5 of 8 subjects). Thus, by using the ventilation data from within the inhaled gas MR image, we were able to introduce guided heterogeneity in the bronchial tree, which was used to predict respiratory impedance that for the most part matched subjects' measurements. This is important as it means that this approach may be physiologically closer to the true airway distribution that led to the measured ventilation and impedance data, leading to a more accurate interpretation of heterogeneity amongst the airways in asthma.

The graded narrowing model was able to produce larger changes to R_{rs} ($p < 0.005$) and X_{rs} ($p < 0.05$) from baseline when compared with the binary model. This affirms the initial hypothesis that the remaining information within the inhaled gas MR image beyond the defect level makes a substantial and significant contribution to the airway mechanics. This is important because it means that a large amount of disease pathology is contained within the ventilated regions, while currently ventilation data in disease is largely interpreted with quantifying the ventilation defects, while the ventilation outside of these regions is largely ignored.

While X_{rs} was quantitatively well matched with subjects' measurement using the graded narrowing model, the R_{rs} spectra was not matched for all frequencies. R_{rs} at 5 Hz was matched well for all subjects with the graded narrowing model by imposing separate closures/dilations to the conducting and terminal airways separately post – simulated annealing. But, the frequency dependence of resistance, quantified by $R_{5\text{-}20}$, was on average 40 ± 20% lower than subjects' measurements. While this was still an improvement over the binary model: 90 ± 10%, this implies that there is something missing from our model that contributes to greater frequency dependence. This could have arisen from various assumptions in our modelling such as: (1) neglecting pendelluft flow when simulating ventilation, which may have limited our predictions of airway heterogeneity, (2) using a homogeneous distribution of acinar stiffness, although adding heterogeneity in the acini might decrease heterogeneity for the airways, or (3) due to an inaccurate registration which could lead incorrect determination of the narrowing and a resulting bias to potentially lower predicted heterogeneity

6.2 Statement of Original Contributions

The following is a brief summary of my original contributions to the development of this thesis.

1. I developed a rigid-registration algorithm to translate and rotate the airway tree to align with subject-specific MRI data using a point-cloud registration that iteratively moves the entire tree, promoting maximal overlap of the tree with the MRI lung that was applied before the application of MIND.
2. I developed the code to implement a generation-dependent scaling of the airway tree when scaling from TLC to smaller lung volumes, whereas previous approaches used a homogeneous scaling of the airway tree diameters and lengths.
3. I have developed the code to segment the airway tree into a slice-format like the MR images and bound the outline of the airway tree to compare with the lung outline of the subjects' MRI.

4. I have further developed the code to deploy the 2D-MIND algorithm (developed by previous students) applied here to deform the airway tree by applying voxel-based deformations from the resultant transformation vector-field.
5. I have developed the code to translate the airway tree (in image-slice format) to a usable data structure for performing fast impedance calculation following deformation.
6. I have developed an algorithm to reconnect the airway tree following deformable registration with linear algebra.
7. I have reformatted previous iterations of code to calculate impedance throughout an airway tree, increasing efficiency (decreasing computational time), and improved modularity.
8. I developed the code to implement Simulated Annealing for optimizing appropriate closure levels for modelling ventilation and determined optimal conditions for “cooling” to achieve very good solutions as measured by the cost function.
9. I developed the code to simulate airflow throughout an airway tree with a flow divider relationship, using calculated impedances from the tree.
10. I developed the code to convert the airflow throughout the tree to an image format for comparison with inhaled gas MRI.
11. I have showed that a graded-narrowing approach for an airway tree is a better method for simulating ventilation, as well as predicting impedance compared with previous binary closure approaches.
12. I developed the code to create a time constant map from an airway tree that has been narrowed by subject-specific graded narrowing solutions.

6.3 Future Work

6.2.1 Subject Specific Tree

As mentioned previously, while we managed substantial improvements in ventilation images, there remained significant differences between the simulated ventilation images and the real ventilation images. We believe that these differences were largely due to the deformation of the generic airway tree to subject-specific MR lung spaces, both due to the fact that the tree was generic and not the subject's, and as well that considerable manipulation of the tree was required to fit within the subjects' MR lung space that was only partially successful. The best way to test both factors would be to use subject-specific grown trees. One way to test this would be to used software like VIDA (VIDA Diagnostics Inc, Coralville, IA, USA), which can be used to delineate airways from a CT data set up to a given generation. The remaining generations can be grown using a fractal-growing algorithm or something equivalent.[72,73] The CT-sets for these eight subjects have already been collected, and testing this premise only requires the generation of subject-specific trees, which I hope to be able to do in the future.

6.2.2 Modified Simulated Annealing

In the study by Campana and colleagues in 2009, they imposed significant closures derived from inhaled gas MR images, to airways with the intent to simulate ventilation images, and then imposed further closures to airways outside of defects to model airway mechanics. We imposed a graded narrowing scheme derived from inhaled gas images to a model airway tree to simulated ventilation, and to model respiratory mechanics. This paradigm improved the quality of the simulated ventilation images and accounted for more changes to Z_{rs} than the binary model. However, the respiratory mechanics were not perfectly modelled, namely the R_{rs} spectra did not exhibit as strong of a frequency dependence from 5 Hz to 20 Hz as the subjects' measurements.

One way to tackle this is to modify the objective function within the simulated annealing framework to consider the quality of the simulated ventilation imaged defined by the SSD, as well as the R_{rs} at 5 Hz and the $R_{5\text{-}20}$. The graded narrowing scheme, along with elastance of the terminal airways, E_{acini}, would be modified to minimize the OF. This novel OF that uses both sets of data would look something like:

$$OF = \sqrt{\alpha\left(\frac{|\,R_{5Hz,m} - R_{5Hz,p}|}{R_{5Hz,p}}\right)^2 + \beta\left(\frac{|\,R_{5-20,m} - R_{5-20,p}|}{R_{5-20,p}}\right)^2 + \gamma\left(Gas_p - Gas_m\right)^2} \tag{50}$$

Where α, β, γ are normalization parameters that would have to be iteratively solved to weigh the contribution of the simulated ventilation image, and respiratory mechanics to the overall fit of a given graded narrowing scheme for accurately modelling a given subjects' respiratory physiology.

Another potential approach would be to alter the flow divider approach to permit other solutions to the ventilation where pendelluft might be approximated. For example, it might be possible to add a pendelluft factor, which increases the heterogeneity predicted from the flow divider approach, exaggerating narrowing of airways as we believe greater heterogeneity is needed (from the lower frequency dependence compared with the measured data). This may be an iterative approach considering high ventilation regions as 'sources' and low ventilation areas as 'sinks' much like the trachea was a source and the entire tree was a sink using the flow divider approach performed in this work.

6.2.3 Time Constant Map

An interesting development in this thesis was the concept of a time constant map. The purpose of this map was to re-represent the degree of ventilation distribution within inhaled gas MR images as but rescaled using a timescale for filling. The regional time-scale of filling was hoped to give useful functional information of the lung using a potentially more familiar variable time instead of gas intensity. The time constant map revealed that much of the lung appeared to be filling or distributing the hyperpolarized ^{3}He within time-scales of normal breathing (1-5 s), but the filling of regional defects was much longer than the time of an MR image acquisition (> 16 s). This appears to mean that in asthma, airway obstruction is sufficient to limit the effectiveness of inhalation to provide fresh air to the gas-exchanging region of the lung. I find this particularly interesting and would like to develop a time constant map derived from the predicted impedances of an airway tree to compare to the map here which was predicted from the ventilation images directly.

.

7. References

[1] S.S. Wager, H.C. Haverkamp, J.H.T. Bates R.J. Norton et al., *Intrinsic and antigen-induced airway hyperresponsiveness are the result of diverse physiological mechanisms*, J. Appl. Physiol. 102: 221-230 (2007).

[2] L.K. Lundblad, J Thompson-Figueroa, G.B. Allen, L. Rinaldi et al., *Airway Hyperresponsiveness in Allergically Inflamed Mice*, Am. J. Respir. Crit. Care. Med. **175**: 768-774 (2007).

[3] A.V. Patterson, P.N. Yeager, *Asthma: Etiology, Pathogenesis and Treatment*, 1st Ed. (Nova Biomedical Books, 2008), pp. 1-10.

[4] B.W. Ward, T.C. Clarke, C.N. Nugent, J.S. Schiller et al., *Early Release of Selected Estimates Based on Data from the 2015 National Health Interview Survey,* National Health Interview Survey Early Release Program (Public Statistics).

[5] T. Nurmagambetov, R. Kuwahara, P. Garbe, *The Economic Burden of Asthma in the United States, 2008–2013*, Ann. Am. Thorac. Soc. **15**(3): 348 - 56 (2018).

[6] T.A. Altes, P. L. Powers, J. Knight-Scott, G. Rakes et al., *Hyperpolarized ^{3}He MR lung ventilation imaging in asthmatics: Preliminary findings*, J. Magn. Reson. Imag. **13**: 378 – 84 (2001).

[7] G. Parraga, A. Ouriadov, A. Evans, S. McKay et al., *Hyperpolarized 3He Ventilation Defects and Apparent Diffusion Coefficients in Chronic Obstructive Pulmonary Disease : Preliminary Results at 3.0 Tesla*, Invest. Radiol. **42**: 384 - 91 (2007).

[8] S. Samee, T. Altes, P. Powers E.E. de Lange et al., Imaging the lungs in asthmatic patients by using hyperpolarized helium-3 magnetic resonance: Assessment of response to methacholine and exercise challenge, J. Allergy. Clin. Immunol. **111**(6): 1205-1211 (2003).

[9] Asthma Society of Canada, *Diagnosis Asthma Basics #1*, Family Physicians Airways Group of Canada, 2017 (Unpublished).

[10] A.S. Gershon, J.C. Victor, J Guan, S.D. Aaron et al., *Pulmonary Function Testing in the Diagnosis of Asthma: A Population Study*, Chest. **141**(5): 1190-1196 (2012).

[11] J.D. Leuppi, C. M. Salome, C.R. Jenkins, H. Koskela et al., *Markers of airway inflammation and airway hyperresponsiveness in patients with well-controlled asthma*, Eur. Respir. J. **18**: 444-450 (2001).

[12] G. Ciprandi, I. Cirrilo, C. Klersy, G.L. Marseglia et al., *Role of $FEF_{25–75}$ as an Early Marker of Bronchial Impairment in Patients with Seasonal Allergic Rhinitis*, Am. J. Rhinol. **20**(6): 641-647 (2006).

[13] G.L. Marseglia, I. Cirillo, A. Vizzaccaro, C. Klersy et al., *Role of forced expiratory flow at 25-75% as an early marker of small airways impairment in subjects with allergic rhinitis*, Allergy. Asthma. Proc. **28**(1): 74-78 (2007).

[14] G. Ciprandi, M.A. Tosca, M. Capasso, *Forced expiratory flow between 25 and 75% of vital capacity might be a predictive factor for bronchial hyperreactivity in children with allergic rhinitis, asthma, or both*, Allergy. Asthma. Proc. **32**(2):4-8 (2011).

[15] M.A. Tosca, M. Silvestri, N. Solari, G.A. Rossi et al., *Inflammation Markers and* FEF_{25-75}*: A Relevant Link in Children With Asthma*, Allergy. Asthma. Immunol. Res. **8**(1): 84-84 (2016).

[16] E.R. McFadden, D.A. Linden*, A reduction in maximum mid-expiratory flow rate: A spirographic manifestation of small airway disease*, Am. J. Med. **52**: 725 - 37 (1972).

[17] A.F. Gelb, A.J. Williams, N. Zamel, *FEV, vs FEF25-75 Percent*, Chest. **84**: 473 - 4 (1983).

[18] S.D. Aaron, R.E. Dales, P. Cardinal, *How Accurate Is Spirometry at Predicting Restrictive Pulmonary Impairment?*, Chest. 115: 869 – 73 (1999).

[19] T.J. Barreiro, and I. Perrilo, *An approach to interpreting spirometry*, Am. Fam. Physician. **69**(5): 1107-1115 (2004).

[20] H.K. Reddel, D.R. Taylor, E.D. Bateman, L.P. Boulet et al., *An Official American Thoracic Society/European Respiratory Society Statement: Asthma*, Am. J. Respir. Crit. Care. Med. **180**: 59-99 (2009).

[21] P.L. Enright, *COUNTERPOINT: Should Oscillometry Be Used to Screen for Airway Disease? No*, Chest, **148**: 1135 – 7 (2015).

[22] J.R. Carroll, J.S. Magnussen, N. Berend, C.M. Salome et al., *Greater parallel heterogeneity of airway narrowing and airway closure in asthma measured by high-resolution CT*, Thorax. **70**(12): 1163 – 70 (2015).

[23] J. Conway, *Lung imaging — Two dimensional gamma scintigraphy, SPECT, CT and PET*, Adv. Drug Deliv. Rev. **64**: 357 – 68 (2012).

[24] B.A.H.A. van der Bruggen-Bogaarts, J.J. Broerse, J.W.J. Lammers, P.F.G.M. van Waes et al., *Radiation Exposure in Standard and High-Resolution Chest CT Scans**, Chest. **107**: 113-5 (1995).

[25] ICRP, *The 2007 Recommendations of the International Commission on Radiological Protection.* ICRP Publication 103. Ann. ICRP 37: 2-4 (2007).

[26] M.S. Albert, G.D. Cates, B. Driehuys, W. Happer et al., *Biological magnetic resonance imaging using laser-polarized* ^{129}Xe, Nature, **370**(6486): 299-201 (1994).

[27] H.U. Kauzor, R Surkau, T. Roberts, *MRI using hyperpolarized noble gases*, Eur. Radiol. **8**(5): 820 – 7 (1998).

[28] E.E. de Lange, T.A. Altes, J.T. Patrie et al., *Evaluation of asthma with hyperpolarized helium-3 MRI: correlation with clinical severity and spirometry*, Chest. **130**(4): 1055-1062 (2006).

[29] A.D. Hahn, R.V. Cadman, R.L. Sorkness, N.N. Jarjour et al., *Redistribution of inhaled hyperpolarized 3He gas during breath-hold differs by asthma severity*, J. Appl. Physiol. **120**: 526-536 (2016).

[30] L. Mathew, M. Kirby, R. Etemad-Rezai, A. Wheatley, *Hyperpolarized ^{3}He magnetic resonance imaging: Preliminary evaluation of phenotyping potential chronic obstructive pulmonary disease,* Eur. J. Radiol. **79**: 140 – 6 (2011).

[31] W.G. Teague, N.J. Tustison, T.A. Altes, *Ventilation heterogeneity in asthma*, J. Asthma, **51**(7): 677-684 (2014).

[32] A. Otis, C. Mckerrow, R. Bartlett, J. Mead et al., *Mechanical Factors in Distribution of Pulmonary Ventilation*, J. Appl. Physiol. **8**: 427-443 (1956).

[33] A.J. Deninger, B. Eberle, M. Ebert, T. Grobmann et al., *Quantification of Regional Intrapulmonary Oxygen Partial Pressure Evolution during Apnea by ^{3}He MRI*, J. Magn. Reson. **141**(2): 207-216 (1999).

[34] H. Marshall, M.H. Deppe, J. Parra-Robles, S. Hillis et al., *Direct visualization of collateral ventilation in COPD with hyperpolarized gas*, MRI Thorax. **67**: 613-617 (2012).

[35] L. Mathew, A. Evans, A. Ouriadov, R. Etemad-Rezai et al., *Hyperpolarized 3He magnetic resonance imaging of chronic obstructive pulmonary disease: reproducibility at 3.0 tesla*, Acad. Radiol. **15**:1298–1311 (2008).

[36] J.C Bezdek, *Pattern recognition with fuzzy objective function algorithms*, Springer Science & Business Media (2013).

[37] J. Macqueen, *Some methods for classification and analysis of multivariate observations*, Proceedings of the fifth Berkeley symposium on mathematical statistics and probability; Oakland, CA, USA, (1967).

[38] M. Kirby, M. Heydarian, S. Svenningsen, A. Wheatley et al., *Hyperpolarized ^{3}He Magnetic Resonance Functional Imaging Semiautomated Segmentation*. Acad. Radiol. **19**(2): 141-152 (2012).

[39] S.B. Fain, G. Gonzalez-Fernandez. E.T. Peterson, M.D. Evans et al., *Evaluation of Structure-Function Relationships in Asthma using Multidetector CT and Hyperpolarized He-3 MRI* Acad. Radiol. **15**(6): 753-762 (2008).

[40] N. Woodhouse, J.M. Wild, M.N. Paley, S. Fichele et al., *Combined helium-3/proton magnetic resonance imaging measurements of ventilated lung volumes in smokers compared to never-smokers*[*], J. Magn. Reson. Imaging. **21**(4): 365-369 (2005).

[41] S. Svenningsen, M. Kirby, D. Starr, D. Leary et al., *Hyperpolarized ^{3}He and ^{129}Xe MRI: Differences in Asthma Before Bronchodilation,* Thorax, **69**(1): 63-71 (2014).

[42] N.J. Stewart, H.F Chan, P.J.C. Hughes, F.C. Horn et al., *Comparison of ^{3}He and ^{129}Xe MRI for Evaluation of Lung Microstructure and Ventilation at 1.5T.* J. Magn. Reson. Imaging. 2018.

[43] D.P.I. Capaldi, K. Sheikh, F. Guo, S. Svenningsen et al., *Free-breathing Pulmonary ^{1}H and Hyperpolarized ^{3}He MRI: Comparison in COPD and Bronchiectasis*, Acad Radiol. **22**(3): 320-329 (2015).

[44] D.P.I. Capaldi, R.L. Eddy, S. Svenningsen, F. Guo et al., *Free-breathing Pulmonary MR Imaging to Quantify Regional Ventilation*, Radiology. **22**: 1-12 (2018).

[45] A.B. Dubois, A.W. Brody, and D.H. Lewis, B.F. Burgess Jr. et al., *Oscillation mechanics of lungs and chest in man,* J. Appl. Physiol. **8**(6): 72-105 (1956).

[46] K.N. Desagner, W. Buhr, M Willemen, H.P. van Bever et al., *Measurement of total respiratory impedance in infants by the forced oscillation technique,* J. Appl. Physiol. **71**(2): 770-776 (1991).

[47] C. Delacourt, H. Lorino, M. Herve-Guillot, P. Reinert et al., *Use of the Forced Oscillation Technique to Assess Airway Obstruction and Reversibility in Children*, Am. J. Respir. Crit. Care. Med. **161**(3): 730-736 (2000).

[48] J.P. Janssens, M.C. Nguyen, F.R. Herrmann, J.P. Michel, *Diagnostic value of respiratory impedance measurements in elderly subjects.* Respiratory. Medicine. **95**(5): 415-422 (2001).

[49] N. Carvalhaes-Neto, H. Lorino, C. Gallinari, S. Escolano et al., *Cognitive function and assessment of lung function in elderly,* Am. J. Respir. Crit. Care. Med. **152**(5): 1611-1615 (1995).

[50] R. Peslin, J. Felicio da Silva, C. Duvivier F Chabot, *Respiratory mechanics studied by forced oscillations during artificial ventilation*, Eur. Respir. J. **6**(6): 772-784 (1993).

[51] K.P. Van de Woestijne, *The forced oscillation technique in intubated, mechanically-ventilated patients,* Eur. Respir. J. **6**(6): 767-769 (1993).

[52] G. Grimby, T. Takishima, W. Graham, P. Macklem et al., *Frequency dependence of flow resistance in patients with obstructive lung disease*, J. Clin Invest. **47**(6): 1455-1465 (1968).

[53] K.R. Lutchen, H. Gillis, *Relationship between heterogeneous changes in airway morphometry and lung resistance and elastance*, J. Appl. Physiol. **83**: 1192-1201 (1997).

[54] H. Pasker, M. Peeters, P. Genet, J. Clement et al., *Short-term ventilatory effects in workers exposed to fumes containing zinc oxide: comparison of forced oscillation technique with spirometry*, Eur. Respir. J. **10**(7): 1523-1529 (1997).

[55] F.M. Ducharme, G.M. Davis, G.R. Ducharme, *Pediatric reference values for respiratory resistance measured by forced oscillation*, Chest. **113**(5): 1322-1328 (1998).

[56] M.J. Hayden, F. Petak, Z. Hantos, G. Hall et al., *Using Low-frequency Oscillation to Detect Bronchodilator Responsiveness in Infants*, Am. J. Respir. Crit. Care. Med. **157**(2): 574-579 (1998).

[57] J. Hellinckx, K. De Boeck, M. Demedts, *No paradoxical bronchodilator response with forced oscillation technique in children with cystic fibrosis*, Chest. **113**(1): 55-59 (1998).

[58] J. Clement, F.J. Landser, K.P. Van de Woestijne, *Total resistance and reactance in patients with respiratory complaints with and without airway obstruction,* Chest. **83**(2): 215-220 (1983).

[59] F. Gimeno, L.T. van der Weele, G.H. Koeter, R. van Altena, *Forced oscillation technique. Reference values for total respiratory resistance obtained with Siemens Siregnost FD5,* Ann. Allergy. **68**(2): 155-158 (1992).

[60] H.G. Pasker, I. Mertens, J. Clement, K.P. Van de Woestijne, *Normal values of total respiratory input impedance with the head generator technique, Eur.* Respir. Rev. **4**: 134-137 (1994).

[61] A. Fisher, A. Dubois, R. Hyde, *Evaluation of the forced oscillation technique for the determination of resistance to breathing,* J. Clin. Invest. **47**(9): 2045-2057 (1968).

[62] K. Jiemsripong, R. Hyatt, K. Offord, *Total respiratory resistance by forced oscillation in normal subjects,* Mayo. Clin. Proc. **51**(9): 553-556 (1976).

[63] R. Peslin, B. Hannhart, J. Pino, *Mechanical impedance of the chest in smokers and non-smokers (author's transl)*, Bull. Eur. Physiopathol. Respir. **17**(1): 93-105 (1981).

[64] E. Oostveen, D. MacLeod, and H. Lorino, R. Farre et al., *The forced oscillation technique in clinical practice: methodology, recommendations and future developments*, Eur. Respir. J. **22**: 1026-1041 (2003).

[65] M.R. Miller, R. Crapo, J. Hankinson, V. Brusasco et al., *General considerations for lung function testing,* Eur. Respir. J. **26**(1): 153-161 (2005).

[66] E.R. Weibel, *Geometric and dimensional airway models of conductive, transitory, and respiratory zones of the human lung* (Springer-Verlag KG, West Berlin, Germany, 1963).

[67] K. Horsfield, G. Cummings, *Morphology of the bronchial tree in man*, J. Appl. Physiol. **24**(3): 373 – 83 (1968).

[68] J.G. Venegas, T. Winkler, G. Musch, M.F.V. Melo et al., *Self-organized patchiness in asthma as a prelude to catastrophic shifts,* Nature. **434:** 777 – 82 (2005).

[69] T. Winkler, J.G. Venegas, *Complex airway behaviour and paradoxical responses to bronchoprovocation*, J. Appl. Physiol. **103**: 655 – 63 (2007).

[70] R.C. Anafi, T.A. Wilson, *Airway stability and heterogeneity in the constricted lung,* J. Appl. Physiol. **91:** 1185 – 92 (2001).

[71] M.H. Tawhai, P. Hunter, J. Tschirren, J. Reinhardt et al., *CT-based geometry analysis and fine element models of the human and ovine bronchial tree*, J. Appl. Physiol. **97**: 2310 – 21 (2004).

[72] M.H. Tawhai, A.J. Pullan, P.J. Hunter, *Generation of an anatomically based three-dimensional model of the conducting airways,* Ann. Biomed. Eng. **28**: 793– 802 (2000).

[73] S. Miyawaki, M.H. Tawhai, E.A. Hoffman, S.E. Wenzel et al., *Automatic construction of subject-specific human airway geometry including trifurcations based on a CT-segmented airway skeleton and surface*, Biomech. Model. Mechanobiol. 16(2): 583-96 (2017).

[74] E.D. Michaelson, E.D. Grassman, W.R. Peters, *Pulmonary mechanics by spectral analysis of forced random noise,* J. Clin. Invest. **56**: 1210-1230 (1975).

[75] Z. Hantos, B. Daroczy, T. Csendes, B. Suki et al., *Modelling of low-frequency pulmonary impedance in dogs*, J. Appl. Physiol. **68**(3): 849 – 60 (1990).

[76] Z. Hantos, B. Daroczy, B. Suki, S. Nagy et al., *Input impedance and peripheral inhomogeneity of dog lungs*, J. Appl. Physiol. **72**(1): 168 – 78 (1992).

[77] J.H.T. Bates, G.M. Maksym, D. Navajas, B. Suki, *Lung tissue rheology and 1/*f *noise*. Ann Biomed Engineer **22**: 674–681, (1994).

[78] D.W. Kaczka, E.P. Ingenito, B. Suki, K.R. Lutchen, *Partitioning airway and lung tissue resistances in humans: effects of bronchoconstriction,* J. Appl. Physiol. **82**(5): 1531 – 41 (1997).

[79] D.W. Kaczka, E.P. Ingenito, E. Israel, K.R. Lutchen, *Airway and lung tissue mechanics in asthma: effects of albuterol*, Am. J. Respir. Crit. Care. Med. **159**: 169 – 78 (1999).

[80] J.J. Fredberg, D. Stamenovic, *On the imperfect elasticity of lung tissue*. J. Appl. Physiol. **67**: 2408 – 19 (1989).

[81] D.W. Kaczka, G.M. Barnas, B. Suki, K.R. Lutchen, *Assessment of Time-Domain Analyses for Estimation of Low-Frequency Respiratory Mechanical Properties and Impedance Spectra.* Ann. Biomed. Eng. **23**: 135 – 51 (1995).

[82] J. Clement, F.J. Landser, K.P. Van de Woestijne, *Total resistance and reactance in patient with respiratory complaints with and without airways obstruction,* Chest. **83:** 215 – 20 (1983).

[83] K. Horsfield, W. Kemp, S. Phillips, *An asymmetrical model of the airway of the dog lung*. J. Appl. Physiol. **52**: 21 – 6 (1982).

[84] R.H. Habib, B. Suki, J.H.T. Bates et al., *Serial distribution of airway mechanical properties in dogs: effects of histamine*, J. Appl. Physiol. 77: 554–566 (1994).

[85] E.L. Lawlor, *Combinatorial Optimization* (Holt, Rinehart & Winston, New York, 1976).

[86] A.V. Aho, J.E. Hopcroft, J.D. Ulman, *The Design and Analysis of Computer Algorithms* (Addison-Wesley, Reading, Massachusetts, 1974).

[87] M.R. Garey, D.S. Johnson, *Computers and Intractability: A Guide to the Theory of NP-Completeness* (Freeman, San Francisco, 1979).

[88] S. Kirkpatrick, C.D. Gelatt, P. Vecchi, *Optimization by Simulated Annealing,* Science. **220**(4598): 671-680 (1983).

[89] C. Yang, M. Kumar, *An information guided framework for simulated annealing*, J. Glob. Optim. **62**: 131 – 54 (2015).

[90] J. de Vicente, J. Lanchares, R. Hermida, *Placement by thermodynamic simulated annealing*, Physics. Letters. A. **317**: 415 – 23 (2003).

[91] S. Costella, M. Kirby, G.N. Maksym, D.G. McCormack et al., *Regional pulmonary response to a methacholine challenge using hyperpolarized ^{3}He magnetic resonance imaging,* Respirology. **17**: 1237-1246 (2012).

[92] W. Zha, R.V. Cadman, D.G. Mummy, M.D. Evans et al., *Regional Heterogeneity of Lobar Ventilation in Asthma Using Hyperpolarized Helium-3 MRI*, Acad. Radiol. **25**(2): 169 – 78 (2018).

[93] D.P.I Capaldi, K. Sheikh, R.L. Eddy, F. Guo et al., *Free-breathing Functional Pulmonary MRI: Response to Bronchodilator and Bronchoprovocation in Severe Asthma*, Acad. Radiol. **24**(10): 1268 – 76 (2017).

[94] J.V. Calvacanti, A.J. Lopes, J.M. Jansen, P.L. Melo et al., *Detection of changes in respiratory mechanics due to increasing degrees of airway obstruction in asthma by the forced oscillation technique*, Respir. Med. **100**: 2207-2219 (2006).

[95] U. Peters, G. Dechman, P. Hernandez, S. Bhatawadekar et al., *Improvement in upright and supine lung mechanics with bariatic surgery affects bronchodilator responsiveness and sleep quality*, J. Appl. Physiol. [Epub ahead of print] (2018).

[96] A.M. Bramley, R.J. Thomson, C.R. Roberts, R.R. Schellenberg, *Hypothesis: excessive bronchoconstriction in asthma*, Eur. Respir. J. **7**: 337 – 41 (1994).

[97] S.J. Gunst, D.O. Warner, T.A. Wilson, R.E. Hyatt, *Parenchymal interdependence and airway response to methacholine in excised dog lobes*, J. Appl. Physiol. **65**(6): 2490 – 97 (1988).

[98] A. Adler, E.A. Cowley, J.H.T. Bates, D.H. Eidelman, *Airway parenchymal interdependence after airway contraction in rat lung explants*, J. Appl. Physiol. **85**(1): 231 – 37 (1998).

[99] N.T. Tgavalekos, M. Tawhai, R.S. Harris, G. Mush et al., *Identifying airways responsible for heterogeneous ventilation and mechanical dysfunction in asthma: an image functional modeling approach*, J. Appl. Physiol. **99**: 2388-2397 (2005).

[100] L. Campana, J. Kenyon, S. Zhaledoust-Sani, Y.S. Tzeng et al., *Probing airway conditions governing ventilation defects in asthma via hyperpolarized MRI image functional modeling,* J. Appl. Physiol. **106**: 1293-1300 (2009).

[101] D. Leary, S. Svenningsen, F. Guo, S. Bhatawadekar et al., *Hyperpolarized ^{3}He magnetic resonance imaging ventilation defects in asthma: relationship to airway mechanics,* Physiol. Rep. **4**(7): 1-14 (2016).

[102] S.A. Bhatawadekar, P. Hernandez, G.N. Maksym, *Modelling resistance and reactance with heterogeneous airway narrowing in mild to severe asthma*, Crit. Rev. Biomed. Eng. **43**(2-3): 97-130 (2015).

[103] S.R. Downie, C.M. Salome, S. Verbanck, B. Thompson et al., *Ventilation heterogeneity is a major determinant of airway hyperresponsiveness in asthma, independent of airway inflammation,* Thorax. **62**: 653-654 (2007).

[104] S. Verbanck, D. Schuermans, M. Paiva, W.Vincken, *Nonreversible conductive airway ventilation heterogeneity in mild asthma,* J. App. Physiol. **94**: 1380-1386 (2003).

[105] P.D. Robinson, P. Latzin, S. Verbanck, G.L. Hall et al., *Consensus statement for inert gas washout measurement using multiple and single breath tests,* Eur. Respir. J. **41**: 507-522 (2013).

[106] D.A. Kaminsky, J.H.T. Bates, C.G. Irvin, *Effects of Cool, Dry Air Stimulation on Peripheral Lung Mechanics in Asthma,* Am. J. Respir. Crit. Care. Med. **162**: 179-186 (2000).

[107] R.H. Habib, R.B. Chalker, B. Suki, A.C. Jackson, *Airway geometry and wall mechanical properties estimated from subglottal input impedance in humans,* J. Appl. Physiol. **77**(1): 441 – 51 (1994).

[108] E. Oostveen, K. Boda, C. P. M. van der Grinten, A. L. James et al., *Respiratory impedance in healthy subjects: baseline values and bronchodilator,* Eur. Respir. J. **42**: 1513 – 1523 (2013).

[109] M.P. Heinrich, M. Jenkinson, M. Bhushan, T. Matin et al., *MIND: Modality independent neighbourhood descriptor for multi-modal deformable registration*, Medical Image Analysis. **16**: 1423-1435 (2012).

[110] J.K. Lui, K.R. Lutchen, *The role of heterogeneity in asthma: a structure-to-function perspective*, Clin. Trans. Med. **6**: 1-11 (2017).

[111] D.W. Kaczka, C. Massa*, Reliability of Estimating Stochastic Lung Tissue Heterogeneity from Pulmonary Impedance Spectra: A Forward-Inverse Modeling Study*, Ann. Biomed. Eng. **35**(10): 1722 – 38 (2007).

[112] T. Xiang, M. Cauberghs, K.P. Van de Woestijne, *Resistance and reactance of the excised human larynx, trachea, and main bronchi,* J. Appl. Physiol. **63**(5): 1788 – 95 (1987).

[113] P. Pelosi, M. Croci, I. Ravagnan, P. Vicardi et al., *Total Respiratory System, Lung, and Chest Wall Mechanics in Sedated-Paralyzed Postoperative Morbidly Obese Patients,* Chest. **109**: 144 – 51 (1996).

[114] J. Nagels, F.J. Landser, L. van der Linden, J. Clement et al., *Mechanical properties of lungs and chest wall during spontaneous breathing,* J. Appl. Physiol. **49**(3): 408 – 16 (1980).

[115] G.M. Barnas, K. Yoshino, S.H. Loring, J. Mead, *Impedance and relative displacements of relaxed chest wall up to 4 Hz,* J. Appl. Physiol. **62**(1): 71 – 81 (1987).

[116] G.M. Barnas, K. Yoshino, D. Stamenovic, Y. Kikuchi et al., *Chest wall impedance partitioned into rib cage and diaphragm-abdominal pathways,* J. Appl. Physiol. **66**(1): 350 – 59 (1989).

[117] M. Cauberghs, K.P. Van de Woestijne, *Effect of upper airway shunt and series properties on respiratory impedance measurements.* J. Appl. Physiol. **66**(5): 2274 – 79 (1989).

[118] A.A. Colletti, R. Amini, D.W. Kaczka, *Simulating ventilation distribution in heterogeneous lung injury using binary tree data structure,* Comput. Biol. Med. **41**(10): 936-945 (2011).

[119] R. Zhao, Y. Wang, A.M. Martinez, *A Simple, Fast and Highly-Accurate Algorithm to Recover 3D Shape from 2D Landmarks on a Single Image,* IEEEtran. **14**(8): 1 – 10 (2015).

[120] H. Zhang, A. Sheffer, D. Cohen-Or, Q. Zhou et al., *Deformation-Drive Shape Correspondancem*, Eurographics Symposium on Geometry Processing, **27**(5): 1 – 9 (2008).

[121] A. de Boer, M.S. van der Schoot, H. Bijl, *Mesh deformation based on radial basis function interpolation,* Comp. Struct. **85**: 784 – 95 (2007).

[122] F. Guo, S. Svenningsen, M. Kirby, D.P.I Capaldi et al., Thoracic CT-MRI coregistration for regional pulmonary structure-function measurements of obstructive lung disease. Med. Phys. **44**(5): 1718 – 33 (2017).

[123] U. Peters, P. Hernandez, G. Dechman, G.N. Maksym, *Repeatability, Reproducibility and Reliability of Respiratory System Impedance Assessed by Oscillometry: Effect of Cheek Support and Inappropriate Positioning of Head and Neck*, American Thoracic Society Conference 2018.

[124] H. Kumar, M.H. Tawai, E.A. Hoffman, C.L. Lin, *The effects of geometry on airflow in the acinar region of the human lung,* J. Biomed. **42:** 1635 – 42 (2009).

[125] A. Hislop, L. Reid, *Development of the acinus in the human lung,* Thorax. **29**: 90 – 4 (1974).

[126] E.E. Greenblatt, J.P. Butler, J.G. Venegas, T. Winkler, *Pendelluft in the bronchial tree,* J. Appl. Physiol. **117:** 979 – 988 (2014).

[127] A.J. Swan, A.R. Clark, M.H. Tawhai, *A computational model of the topographic distribution of ventilation in healthy human lungs,* J. Theo. Biol. **300:** 222 – 31 (2012).